Mathematical Modeling of Fluid Flow and Mixing in Metallurgical Reactors with Bottom Gas Injections

by

Liping Li

B.S., Engineering Mechanics, Huazhong University of Science and Technology, China
(1985)
M.S., Engineering Mechanics, Tsinghua University, China
(1991)
M.S., Mechanical Engineering, Massachusetts Institute of Technology
(1994)

Submitted to the Department of Mechanical Engineering
in Partial Fulfillment of the Requirements for the Degree of
Doctor of Philosophy in Mechanical Engineering

at the

Massachusetts Institute of Technology

September 1996

Signature of Author . . . .
Department of Mechanical Engineering
August 9, 1996

Certified by . . . .
Robert M. Rose
Professor of Materials Science and Engineering
Thesis Supervisor

Accepted by . . . .
Ain A. Sonin
Chairman, Departmental Committee on Graduate Students

Mathematical Modeling of Fluid Flow and Mixing in Metallurgical Reactors with Bottom Gas Injections

by

Liping Li

Abstract

The counter-current flow of the molten metal and slag streams is a key feature in many of the new generation of metal refining operations in which gas injection is generally involved. In order to have a quantitative understanding of this kind of systems, a mathematical model was developed to represent fluid flow, mixing and mass transfer phenomena in a channel-type continuous reactor with bottom gas injections. The model solves for two phases (liquid and gas) in 2-D (cylindrical) and 3-D (Cartesian) coordinate systems and has the capabilities to predict the gas volume fractions, velocities for each phases. A modified version of the k-ϵ two-equation model was used to simulate the turbulence. This is considered a first attempt to model a continuous gas-stirred reactor system numerically.

Calculations on a cylindrical system with central bottom injection was used to verify the model, since experimental measurements were available in the literature for this type of system. A good agreement was obtained with two independent sets of experimental measurements. A mixing time study was carried out to understand the effect of gas flow rate and positioning of the gas injection nozzle. It was found that the reactor has a shorter mixing time with eccentric gas injection than with central injection, presumably due to the additional horizontal recirculation induced by the eccentric injection. The optimal locations for tracer additions that provide minimum mixing times were also determined from the study for systems with central gas stirring.

A channel-type continuous reactor model, which has an experimental setup counterpart at the University of Missouri-Rolla (UMR), was studied numerically. Tracer dispersion analysis was used to analyze the longitudinal mixing in the reactor. The predicted longitudinal diffusivities were compared with the experimental measurements obtained at UMR. The effects of different operating parameters, such as gas flow rate, reactor aspect ratio, bubbler separation and liquid flow rate, were investigated with the purpose of seeking ways to minimize longitudinal mixing in such system.

Based on the physical model at UMR, a liquid-liquid mass transfer analysis was conducted as a necessary component to determine the feasibility of continuous counter-current metallurgical reactors. The overall mass transfer characteristics in this kind of system were analyzed by introducing simplifying assumptions that allowed the incorporation of the effects of a third (liquid or slag) phase as part of the surface boundary condition. The effects of different process parameters on the conversion ratio were summarized in terms of two dimensionless numbers that combine the overall fluid flow and mass transfer characteristics of the reactor – the inverse Peclet number (D_e/uL) and the Damköhler number (kL/uH). Some examples of ways to increase the reactor conversion ratio include decreasing the bubbler separation, increasing the gas flow rate and optimizing reactor aspect ratio. It was concluded that the reactor length is the most critical parameter in determining the level of conversion for the range of conditions under study. It was also found that, for the same system, a length-to-height ratio of 20 is needed for a conversion ratio above 90%.

Finally, the model's capabilities and limitations are summarized and future directions are suggested.

Thesis Supervisor: Robert M. Rose
Title: Professor of Materials Science and Engineering

Thesis Supervisor: Julian Szekely
Title: Professor of Materials Science and Engineering

Acknowledgments

I would like to express my grateful appreciation to the late Professor Julian Szekely for giving me the opportunity to work on this project and for his advice during the progress of this work. His knowledge in metallurgy, materials processing and beyond helped me tremendously whenever I encountered problems during this work.

Thanks to Professor Robert M. Rose for taking the responsibility of being my thesis advisor on such short notice. His encouragement and valuable suggestions are appreciated.

Thanks to Dr. Gerardo Trapaga, my "virtual" advisor, for the advice and support from the beginning of this work. He is the source of endless suggestions and ideas.

Many thanks go to Professor Ain A. Sonin and Professor Uday B. Pal for serving on my thesis committee and their valuable suggestions in the process of this work. Special appreciation to Professor Sonin for his continuous support as the only "official" connection I had with the Department of Mechanical Engineering.

Thanks to members of the Materials Process Modeling Group of the Department of Materials Science and Engineering, both in Room 8-135 and Room 4-033, who provided their expertise and friendship. These current and former officemates are (no special order): Robert Hyers, Adam Powell, Christy Choi, Nicole Lazo, Professor Xuebin Yu, Hirokazu Shima, Naoki Ono, Masaki Nagai, G. Kris Schwenke, Scott Deering, David E. Woolley, Elliot M. Schwartz, Patricio Mendez, Martin Herrera-Trejo, Bernardo Bulnes, and Professor Andreas Alexandrou.

Thanks to Professors and former officemates of the Mechanics and Materials Group of the Department of Mechanical Engineering for their support and friendship while I was a graduate student there and thereafter. Special thanks to my former advisor Dr. Mark F. Sylvester for his guidance and support from my first visit of MIT and through the later two years that I worked with him on the plastic deformation mechanisms in crystalline polymers. He is a very special person to me.

And finally, thanks to my parents and my two younger sisters for their love and support.

Contents

List of Figures

9

10

List of Tables

Nomenclature

Roman Symbols

A area (m^2)

a surface area per unit of volume (m^{-1})

B a constant

b_u half velocity radius (m)

C normalized concentration or a constant

C_D drag coefficient or a constant

C_f inter-phase friction coefficient

C_μ, $C_{1\epsilon}$, $C_{2\epsilon}$, C_{k1}, C_{k2}, $C_{\epsilon1}$, $C_{\epsilon2}$ constants

c tracer concentration (kgm^{-3}) or a constant

c_i concentration at the reactor inlet (kgm^{-3})

c_m concentration in the lower liquid phase (kgm^{-3})

c_o concentration at the reactor outlet (kgm^{-3})

c_s concentration in the upper liquid phase (kgm^{-3})

c'_m equilibrium concentration in the lower liquid phase (kgm^{-3})

c'_s equilibrium concentration in the upper liquid phase (kgm^{-3})

D laminar diffusivity $(m^2 s^{-1})$

D_t turbulent diffusivity $(m^2 s^{-1})$

D_e longitudinal (axial) diffusivity $(m^2 s^{-1})$

d_b diameter of bubbles (m)

d_c diameter of the crucible (m)

d_p diameter of particles (m)

$\vec{F}_f$ drag force on the gas phase from the liquid phase per unit of volume (Nm^{-3})

$\vec{g}$ gravitional acceleration (ms^{-2})

H_1 height of the lower liquid level in the reactor (m)

H_2 height of the upper liquid level in the reactor (m)

H height of the liquid (same to H_1) (m)

I turbulent intensity

J flux of mass flow (kgs^{-1})

K equilibrium constant for a reaction

k turbulence kinetic energy (Jkg^{-1}) or mass transfer coefficient (ms^{-1})

k_{in} turbulence kinetic energy at the nozzle inlet (Jkg^{-1})

k_o overall mass transfer coefficient (ms^{-1})

L length of the channel-type reactor or boundary layer thickness (m)

L_s turbulence length scale (m)

l_m a length scale (m)

Pe Peclet number, also called Bodenstein number (D_e/uL)

P_k production of turbulent kinetic energy (s^{-2})

P_s equilibrium partition ratio

p pressure (Pa)

Q gas volume flow rate (Nm^3s^{-1})

Q^* a critical gas volume flow rate (Nm^3s^{-1})

Re Reynolds number (nozzle, bubble or particle)

R_g gas volume fraction

R_l liquid volume fraction

r radial coordinates

r_o radius of the nozzles (m)

Sc laminar Schmidt number (μ/D)

Sc_t turbulent Schmidt number (μ_t/D_t)

Sh Sherwood number (or mass transfer Nusselt number)

S_{k1}, S_{k2}, $S_{\epsilon1}$, $S_{\epsilon2}$ source terms in turbulence equations

t time (s)

t_R residence time (s)

t_m mixing time (s)

t_{mean} the nominal mean residence time (s)

$\bar{t}_{mean}$ the actual mean residence time (s)

ΔU slip velocity at liquid-liquid interface

U_{cl} axial velocity at the centerline of a cylindrical reactor (ms^{-1})

$U_{rms,cl}$ root-mean-square of the instantaneous components of velocity at the centerline of a cylindrical reactor (ms^{-1})

u_i', u_j' instantaneous components of velocity (ms^{-1})

u_i, u_j mean components of velocity (ms^{-1})

u horizontal liquid velocity in the channel-type reactor (ms^{-1})

V volume (m^3)

$\vec{V_g}$ velocity vector of the gas phase (ms^{-1})

V_i velocity component of the "lazy" particles (ms^{-1})

$\vec{V_l}$ velocity vector of the liquid phase (ms^{-1})

$\vec{V_r}$ relative velocity between gas and liquid phases (ms^{-1})

V_{slip} slip velocity between two phases (ms^{-1})

V_s turbulence velocity scale (ms^{-1})

W width of the channel-type reactor (m)

W_{in} gas velocity through the nozzle (ms^{-1})

X, Y, Z spatial coordinates

Greek Symbols

ρ_g density of gas phase (kgm^{-3})

ρ_l density of liquid phase (kgm^{-3})

ρ_p density of particles (kgm^{-3})

μ laminar viscosity of liquid phase $(kgm^{-1}s^{-1})$

μ_t turbulent viscosity of liquid phase $(kgm^{-1}s^{-1})$

μ_{eff} effective viscosity $(kgm^{-1}s^{-1})$

ν laminar kinematic viscosity (m^2s^{-1})

ν_t turbulent kinematic viscosity (m^2s^{-1})

Γ_{eff} effective mass diffusion coefficient (kgs^{-1})

ϵ dissipation rate of turbulence kinetic energy $(Jkg^{-1}s^{-1})$

σ statistical variance or surface tension (kgs^{-2})

σ_k, σ_ϵ constants

τ_{12} shear force at the liquid-liquid interface

Λ_f characteristic length of turbulent eddies (m)

δ_{ij} Kronecker delta

Subscribt

b bubble

eff effective

g gas

i inlet

l liquid or laminar

m melt

o outlet

p particle

s slag

t turbulent

i, j, k spatial coordinates

Chapter 1

Introduction and Background

1.1　Introduction

In steelmaking, inert and reactive gases are often supplied in the form of a single jet or multiple jets, at various stages of melt refining, to promote slag-metal reactions, eliminate thermal and/or composition gradients, help inclusion flotation, remove particulates and so on. The wide use of this method results from both practical and economical aspects. On one hand, mechanical mixing is impractical at temperatures as high as around 1600°C. On the other hand, electromagnetic mixing has the advantage of flexibility in control, but it is more expensive compared to mixing by gas injection, and it is generally believed that the electromagnetic stirring does not provide sufficient mixing power either.

Gas injection is widely used in industries other than steelmaking; for example: the Noranda process [1] for the continuous smelting and converting of copper and the QSL lead making process [2] in nonferrous industries. In addition to this, gas injection also has applications in chemical engineering (bubble column) and environmental engineering (removing temperature stratification of a lake). Several examples of industrial processes in which gas injection is applied are shown in Figure 1-1. Common to all of these processes is the gas/liquid plume produced by submerged gas injection(s) into a melt of metal and a less dense, immiscible slag or matte phase. The fluid flow in these kinds of processes is typically buoyancy driven, turbulent and

19

three-dimensional.

Under industrial conditions, only relatively low gas flow rates are applied to achieve thermal and/or chemical homogenization; somewhat more intense stirring conditions can also be practiced for accelerating slag-metal reactions. It is generally believed that the stirring results from the expansion of the gas due to the heating of the gas and the decreasing pressure (buoyancy) as the gas rises. Only a small portion is associated with the momentum of the injected gas (less than 5%).

Although gas injection has been practiced in the steelmaking industry for about 130 years, there is still not enough quantitative understanding of the fluid dynamics and mixing behavior in these systems. The main reason for this is that the fluid flow in these processes are typical of gas-melt-slag three phase flows with high turbulence intensity. The possibility of practicing continuous steelmaking makes it more attractive to have a better mathematical model to represent the fluid flow and turbulence in gas-stirred reactors. Very little work addressing the issue of gas injection in continuous channel-type reactors has been done so far.

1.2 Batch vs. Continuous Reactors

Metallurgical reactors can be classified into two broad categories: batch reactors in which materials are charged, refined over a period of time and then discharged; and continuous flow reactors, where reagents are fed continuously at one point and products are withdrawn continuously at another.

Many converting and refining processes are usually carried out in more than one batch reactor, in which the product of one reactor is transferred to the next and different reactions take place in each reactor. If this complete process is to be carried out in a long continuous channel-type reactor, these individual steps must be conducted successively as materials pass through the reactor.

Batch reactors and continuous reactors are very different conceptually. Some advantages for batch reactors include a flexible residence time, allowing very violent stirring, lower cost (especially in low-volume production) and universal applicability.

(a) An AOD Vessel

(b) HIsmelt Process

(c) Noranda Process
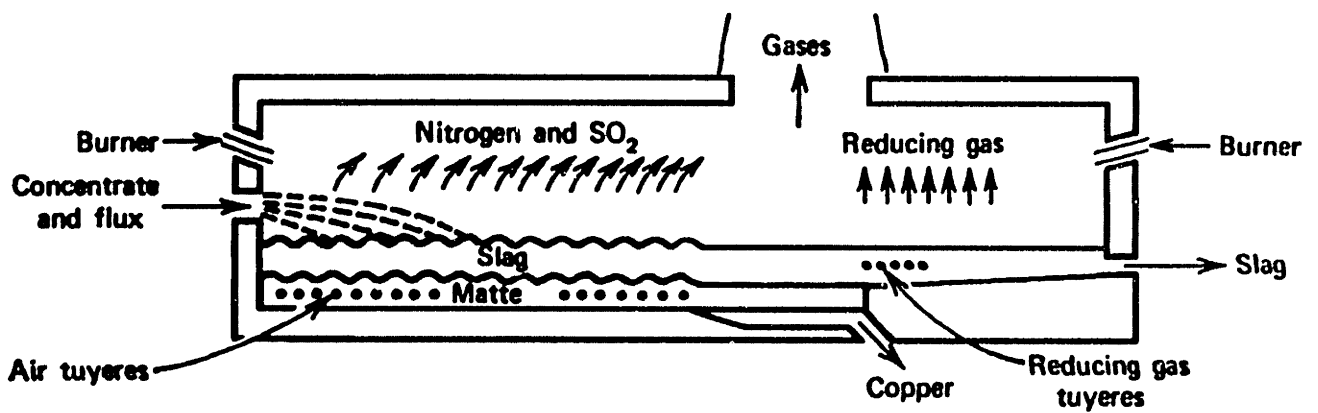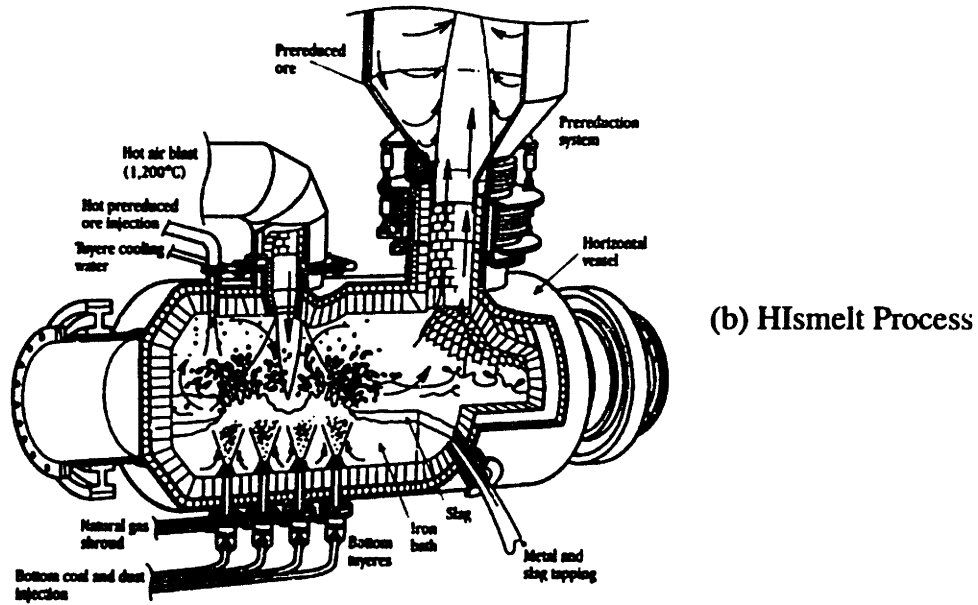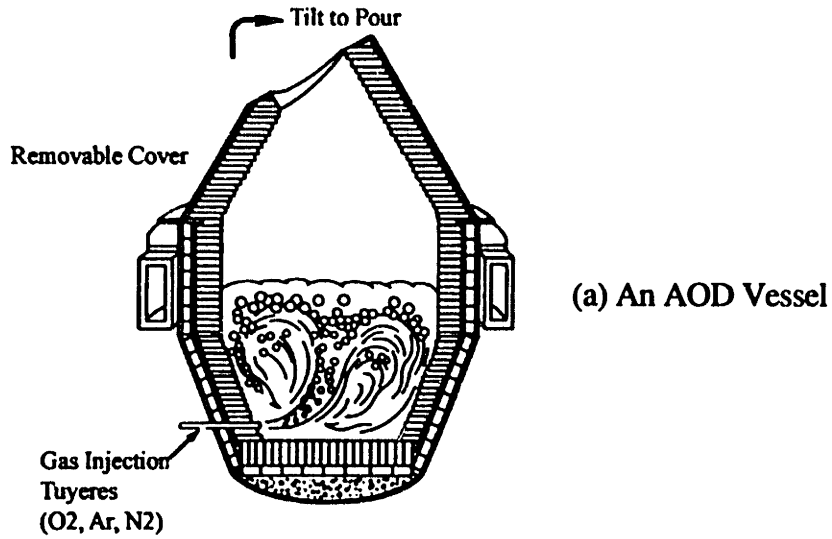
Figure 1-1: Examples of industrial processes in which gas injections are used.

Table 1.1: A comparison of basic characteristics of batch and continuous reactors.

Characteristics	Batch reactors	Continuous reactors
Operation	Easy to shutdown frequently, lose temperature from batch to batch, high capital cost, high refractory wear	Cause big waste by shutdown, but save energy because of continuous operation, low capital cost, low refractory wear
Residence time	Same for all fluid elements, long and flexible	Having a distribution, short and limited
Driving force for mass transfer	Maximum at the beginning, getting lower	Maximum all the way to the exit
Numerical simulation	Time dependent	Time independent
Issues concerned	Homogeneity	Low longitudinal mixing
Design	Known experience available	Not much previous experience available

Advantages for continuous reactors include maximum efficiency with reaction processes in counter-flow arrangements, uniformity of product quality, easy automation, and suitability for greater throughput due to compact size of plants.

Table 1.1 compares the basic features of two types of reactors. Although batch reactors are not very suitable for heterogeneous reactions, they are the type most commonly used in steelmaking because metallurgical refining processes take place in extreme conditions. There are many unsolved technical problems hindering the use of more advantageous but more complex systems such as counter-flow systems.

1.3 Objective

A key concept in many of the new generations of refining metallurgical operations for ferrous and non-ferrous metals involves the counter-current interaction between molten metal and slag streams. Since counter-current processing has been attributed with a number of benefits and is being considered as a promising alternative to general refining operations.

The research project described in this thesis is part of a collaborative effort with other institutions in a research program aimed at studying the counter-current con-

cept within an industrial reference frame. Specifically, the work carried out in this thesis is the theoretical counterpart of the experimental work carried out at UMR.

The main objective of this study at MIT is the development of a mathematical model to represent the overall fluid flow, mixing and mass transfer characteristics in a counter-current continuous channel-type reactor under various operating conditions. One goal of the research was to develop some understanding of this type of system in order to assess its feasibility. The model development covered in this thesis is based on a laboratory scale water-nitrogen physical modeling setup built at UMR; it is expected that this mathematical modeling work will be able to provide some insight into the experimental work being conducted there.

The ultimate objective of this program is to use the model to simulate the behavior of metallurgical counter-current operations, such as in steelmaking refinement, under pilot or full scale conditions.

1.4   Previous Work

In this section, the related work on the fluid flow and mixing behavior of a gas-injected reactor is reviewed, while the work on the liquid-liquid mass transfer analysis is deferred to Chapter 5 where this topic is elaborated.

An excellent review by Mazumdar and Guthrie [3] about gas stirred ladle systems has been published and its full content will not be repeated here. To provide a general picture of gas-stirred systems, a summary of the review follows.

Considerable efforts have been made during the past two decades to investigate gas injection operations in steelmaking ladles. Symmetrically and asymmetrically placed lances/tuyeres/porous plugs have been used as gas injection devices and studies have been reported on systems for wide range of vessel geometry and gas flow rates. The current knowledge in gas injection system indicates that under ladle refining conditions, apart from the vicinity of the nozzle, well dispersed spherical caps bubbles can be expected in the two phase region. Over most of the two phase zone, nozzle configurations have little influence on bubble and liquid rise velocities, gas volume

fraction distribution, etc., and are therefore not critical to the overall flow recirculation produced. The rising bubbles induce a recirculatory motion of liquid within the vessel, which typically has its "eye" located in the upper quadrant of the ladle and displaced towards the side wall. Turbulence in the plume is slightly skewed to the vertical direction. The intensity of liquid motion and mixing in the vessel is relatively sluggish in the presence of an upper slag phase in comparison to an equivalent no slag situation.

In the following, only the work that has not been considered in the review, or is directly related to the current work, will be covered which includes multiple gas injections and channel-type counter-current reactors.

1.4.1 Experimental Measurements

Water is considered to be a suitable material to physically model metallic systems for the following reasons: the kinematic viscosity of water and molten metals are in the same order of magnitude and the bubble rise velocities in water and metals are practically equal.

In a recent investigation by Iguchi et al. [4], a water-oil (silicone)-air system was used to study the effect of the top slag on the mean flow and turbulence characteristics in a steel bath agitated by bottom gas injection. The axial and radial mean velocity components, the root-mean-square (rms) values of the turbulence fluctuations, the Reynolds shear stress, and the turbulence production for two cases, with and without top slag, were measured.

In the case of channel-type reactors, several experimental investigations related to fluid flow and mixing behavior have been reported so far.

A comprehensive experimental analysis on the longitudinal mixing of a channel-type reactor was done by Sahai [5] in 1988. Dye tracer injection was used to investigate the mixing behavior and to perform flow visualization. Mean velocity fields created in water due to gas bubbling were measured by Laser Doppler Anemometry (LDA). Although the reactor used in the experiments was a "stationary system," the results obtained were very instructive.

24

By means of residence time measurements and light section analysis, a channel-type reactor model with top-blowing lances was developed by Koch et al. [6], in which both two (water-air, water-oil) and three phase (water-oil-air) conditions were tested. Caprylic acid was used to simulate the mass transfer of tramp elements from the pig iron into the slag using conductivity measurements.

Experimental work on channel-type reactors with bottom gas injections has also been reported by Iyer and Sohn [9]. A liquid bath consisting of aqueous and organic phases with a 1° slope was used to simulate the Queneau-Schuhmann (QS) reactor. The effects of liquid density, flow rate, gas injection rates, injector diameter, and injector spacing on the residence time distribution (RTD) behavior of the reactors were investigated. A mathematical model called the "ideal-reactor-network model" was also developed to describe the longitudinal mixing behavior of the system.

1.4.2   Computer Simulations

The mathematical modeling effort on the fluid flow and mixing phenomena in a gas-stirred metallurgical reactor can be divided into three categories, namely,

1. the quasi single-phase or the single phase variable density procedures [12, 14-16], in which the gas plume is considered as a homogeneous liquid of reduced density. The gas volume fraction, along with the geometry of the plume, is specified *a priori* in the numerical solution scheme through an empirically determined correlation.

2. the Lagrangian-Eulerian two phase approach [19, 21], in which a set of equations describing the liquid-phase are solved simultaneously with equations representing bubble trajectories.

3. the Eulerian-Eulerian two phase models [22, 24, 26-29], in which both liquid and gas phases are treated as a continuum and a set of continuity and momentum equations are simultaneously solved for both phases.

A detailed comparison of the three mathematical modeling procedures was provided by Mazumdar and Guthrie [30] in which they claimed that the computed axial velocity in the bulk using the different models are very similar and agree well with experimental measurements. However, in the plume region, the two sets of estimated liquid rise velocities are somewhat different. Furthermore, all modeling procedures require a number of parameters, such as bubble size, plume dimension, drag coefficient, etc., to be specified *a priori*. When considering the simplicity of implementation and computer time requirements, the quasi single-phase method is by far the best.

A mathematical modeling investigation on the gas-stirred ladle was reported recently by Jönsson and Jonsson [29] where they claim to use a more realistic treatment in the nozzle and plume region. The predicted gas fraction and velocity in a water model agreed well with experimental data, while the calculated surface velocities were only of the same order of magnitude as the experimental data.

A mathematical model which was claimed to be able to simulate two liquids and one gas phase simultaneously was reported by Richter et al. [67]. A finite volume code, K-FIX developed at Los Alamos National Laboratory, was used to carry out the implementation of the model. Void fractions in water and oil were reported and compared with measurements.

The modeling procedure that has been selected in this thesis is the Eulerian-Eulerian two phase procedure for the reasons explained in the next chapter.

It is generally believed that the fluid flow in the bulk is well understood for a ladle with one central gas stirring at the bottom. The gray areas are concentrated in the regions which are either close to the nozzle or close to the free surface of the system. There are only a few mathematical modeling investigations related to multiple gas injections that have been reported so far. To the best of the author's knowledge, there have not been any fluid flow and turbulence simulations dealing with channel-type reactors reported to date.

1.5 Modeling Approach and Arrangement of the Document

The approach involved in this thesis was to first to develop a model to represent a two-dimensional axisymmetric system. The results were compared with available experimental data and some parametric analyses were performed for a cylindrical system. Second, the model was extended to a three-dimensional and multiple nozzle system, while parametric analysis was also conducted to minimize the system's longitudinal mixing. Finally, a liquid-liquid mass transfer analysis was carried out to investigate the feasibility of continuous channel reactors.

A general fluid flow and heat transfer program PHOENICS was used to implement the model.

All the fundamental compositions, as well as some specific treatments, of the mathematical model are described in Chapter 2. Any case related to the specific implementation of the model will be described in the corresponding chapters. Chapters 3 and 4 describe the model's applications to aqueous systems under different geometric arrangements since most of the experimental work was done using water models. These involved solving two sets of conservation equations with the consideration of turbulence and mixing analysis. Mass transfer analysis was used to study the feasibility of the channel-type continuous reactor in the refining of metals and the effort is reported in Chapter 5. Chapter 6 summarizes the main implications of this work and important conclusions are drawn with supplemental discussions. Finally, Chapter 7 suggests the future directions for studies related to gas injections and metal refining.

Chapter 2

Mathematical Model

2.1 Introduction

The formulation and the approach involved in the mathematical model of the two-phase reactor systems (gas-liquid) is described in this chapter. Specifically, the fluid dynamic aspects of the model, including turbulence as well as two different techniques employed to analyze the mixing characteristics of the reactor and the mass transfer component of the model are presented, in some detail, in this chapter.

2.2 Model Description

The mathematical model developed to simulate a metallurgical reactor with bottom gas injection was based on a two-phase method called IPSA (Inter-phase Slip Algorithm) [35] which solves two sets of Navier-Stokes equations simultaneously (one for liquid phase and one for gas phase). An Eulerian-Eulerian technique is used in this method, which means both phases are treated as space-sharing interspersed continua. The contribution of each phase is measured by its volume fraction of that phase occupied.

The rationale for using the Eulerian-Eulerian technique is three fold:

1. For a channel-type reactor, there are no experimental measurements available related to the plume size, shape, the gas volume fraction distribution and the

28

interactions between plumes in the system. Therefore, a quasi-single phase method, in which a prescribed gas plume is assumed, seems impractical.

2. Since the number of bubblers for a channel-type reactor is much more than one, in a special case in this study, it is as high as 10, the number of ordinary equations to be solved in order to obtained representative bubble trajectories would be beyond the capabilities of currently available computers. Naturally a Lagrangian-Eulerian two phase model is out of the consideration. Another limitation the Lagrangian-Eulerian two phase model has is that the volume fraction of the dispersed phase has to be insignificant, because all published particle tracking methods assume negligible dispersed phase volume fraction.

3. The Eulerian-Eulerian two phase method has the capability to predict the plume size, shape and gas volume fraction distribution in the system from first principles, which is very important for a system with little existing knowledge.

2.2.1 Assumptions

A reactor with multiple bottom gas injections is a very complex system. Indeed, in order to mathematically model the fluid flow and mixing characteristics of the system, certain assumptions are needed. These assumptions are listed as follows.

1. Fluid flow is assumed steady state and considered incompressible.

2. The top free surface is flat.

3. The bubbles are spherical and rigid. This assumption holds for small bubbles and is at least a convenient approximation for large bubbles.

4. Bubble diameter is constant everywhere in the system.

5. Bubble breakup and coalescence are not taken into account.

2.2.2 Governing Equations

The model consists of a set of elliptic partial differential, source-balance equations that express the conservation of mass, momentum and other fluid variables, applied to each of the two phases. The modified Navier-Stokes equations generalized to take into account the facts that each of the phases occupies only part of the space, given by the volume fraction and the phases are exchanging mass and all other properties are as follows (for list of symbols see the Nomenclature at the beginning of this thesis):

continuity equations:

$$\nabla \cdot (R_l \rho_l \vec{V_l}) = 0 \tag{2.1}$$

$$\nabla \cdot (R_g \rho_g \vec{V_g}) = 0 \tag{2.2}$$

and momentum equations:

$$\nabla \cdot (R_l \rho_l \vec{V_l} \vec{V_l} - R_l \mu_{eff} \nabla \vec{V_l}) = -R_l \nabla p + \vec{F_f} \tag{2.3}$$

$$\nabla \cdot (R_g \rho_g \vec{V_g} \vec{V_g} - R_g \mu_{eff} \nabla \vec{V_g}) = -R_g \nabla p - \vec{F_f} + R_g \rho_l \vec{g} \tag{2.4}$$

where μ_{eff} is the effective viscosity, which is defined as:

$$\mu_{eff} = \mu + \mu_t \tag{2.5}$$

where μ and μ_t are the laminar and turbulent (eddy) viscosity, respectively.

In the above governing equations, R_g is the volume fraction of the gas phase and R_l is the volume fraction of the liquid phase; ρ_g is the density of the gas phase and ρ_l is the density of the liquid phase; $\vec{V_g}$ and $\vec{V_l}$ are the time-averaged velocity vectors for the gas phase and the liquid phase, respectively; p is the pressure shared by both phases; $\vec{F_f}$ is the drag force that the gas phase exerts on the liquid phase, and vise versa, as it will be explained in detail later in this chapter; $\vec{g}$ is the gravitational acceleration.

The physical meanings for each of the terms in the governing equations are as follows: The first term on the left hand side of the momentum equations is the

convection term and the second term is the diffusion term. On the right hand side of the momentum equations, there are source terms. The first term on the right hand side is the pressure term, the second is the drag force term and the third term in the second momentum equation is the buoyancy force on the gas phase coming from the liquid phase.

An additional equation is needed in order to close the set of conservation equations. In fact, as the phases completely fill the available space, all volume fractions must sum to unity, i.e.,

$$R_l + R_g = 1 \tag{2.6}$$

Equations (2.1) to (2.6) are the basic equations which have to be solved in order to simulate the two-phase flow systems. More detailed treatment and implementation of the model will be explained in the following subsections.

2.2.3 Turbulence Model

In general, the fluid flow in a metallurgical reactor with gas injections is highly turbulent. Special care has to be taken to realistically model the turbulence. Currently, there are two kinds of methods available to simulate turbulence: *Direct Numerical Simulation* and *Turbulence Models*.

Direct simulation of turbulence involves solving the transient Navier-Stokes equations to the finest scale of eddies. Considering the fact that the need to represent all eddies from the smallest to the largest scales, this leads to a calculation requiring $Re^{1/4}$ calculation points to represent all time and length scales, which is extremely difficult to handle for the present computers. Naturally, this method is not further considered in this study.

Turbulence model approach was chosen in our two-phase model. In using turbulence models, the instantaneous motion of the fluid is decomposed into a mean component and a fluctuation component. The so called REYNOLDS STRESSES has been introduced to represent the unknown transport of momentum due to turbulence because of the statistic-averaging process. Most of the turbulence models use the

31

eddy viscosity concept to determine the Reynolds Stresses from:

$$- \rho u_i' u_j' = \mu_t (u_{i,j} + u_{j,i}) - \rho \frac{2}{3} k \delta_{ij} \qquad (2.7)$$

where u_i' and u_j' are the instantaneous components of the velocity, and u_i and u_j are the mean components of the velocity; μ_t is the turbulent or eddy viscosity and k is the turbulence kinetic energy; ρ is the density of the fluid and δ_{ij} is the Kronecker delta. It is important to understand that μ_t is not a fluid property, but it depends on the state of turbulence in the flow system and must be determined by one of the available turbulence models.

For most of the turbulence models, μ_t is proportional to a turbulence velocity scale V_s and a turbulence length scale L_s.

$$\mu_t = C \rho V_s L_s \qquad (2.8)$$

where C is an empirical constant. It is emphasized here that the scales V_s and L_s characterize the large-scale turbulent motion. Table 2.1 gives a comprehensive comparison of some of the currently available turbulence models. Their advantages and disadvantages are discussed under specific applications.

A modified version of the two-equation $k - \epsilon$ model was used in this work. A two-equation $k - \epsilon$ model [38] was chosen because the model accounts for the transport effects of the turbulent velocity scale and length scale and there is a large body of experience where the $k - \epsilon$ model has been successfully used. This model, however, also has some disadvantages. For example, the local turbulence Reynolds number must be high which is not always the case in a metallurgical reactor. There is also evidence showing that the model is not sufficient when gravity or rotational forces are present in the flow system. It has been suggested that additional terms must be included to take into account the generation and dissipation of turbulence due to the interaction between the gas plume and the bulk liquid. Several alternatives of additional terms have been proposed to represent the generations of turbulence from buoyancy or fluid recirculation. Two additional terms proposed by Malin [39]

Category	Name of the models	Description	Advantages and disadvantages
Zero-equation	Constant viscosity Prandtl's mixing length LVEL model	V_s and L_s are directly calculated from the local mean quantities.	Suitable for simple shear-layer-dominated or pressure driven flows. Easy and computationally economical. Unsuitable for complex flows.
One-equation	Prandtl's $k - L$ model Prandtl's energy model	V_s is calculated from a suitable transport equation, e.g. k, and L_s is prescribed empirically	Accountable for the transport effects of the turbulent velocity scale. The length scale still has to be prescribed empirically.
Two-equation	$k - W$ model $k - \epsilon$ model Chen-Kim $k - \epsilon$ model RNG $k - \epsilon$ model	V_s and L_s are calculated from two transport equations	Accountable for the transport effects of the turbulent velocity scale and length scale. The local turbulent Reynolds number must be high. Limited universality due to the rather simple modeling of ϵ. Assuming isotropy.
Others	Reynolds-Stress model	Involves transport equations for all components of the Reynolds stress tensor, and in general, a transport equation for L_s.	Accountable for complex strain fields associated with curvature, rotation, swirl, buoyancy, etc. Anisotropic and computationally expensive.
	Two fluids model	Mixture of two fluids, each moving in the same space.	Free from the restriction of the turbulent viscosity concept. The number of equations are twice as large as for single-fluid model. Only handle one set of Navier-Stokes equations.
	Algebraic stress model	Intermediate to two equation eddy-viscosity models and Reynolds-Stress model.	Conveniently to account for the effect of body forces.
	2-scale $k - \epsilon$ model	Two transport equations for each k and ϵ, respectively, representing the "production" and "transfer" of turbulence.	Capability to model the cascade process of turbulence kinetic energy, and to resolve the details of complex turbulent flows (e.g. separating and reattaching).

Table 2.1: A summary of a wide spectrum of turbulence models.

and Simonin [40] were used in this work to represent the additional generation of turbulence from the rising bubbles, as discussed at the end of this subsection.

In the conventional two-equation $k - \epsilon$ model, the velocity scale V_s is calculated from solution of a transport equation for turbulence kinetic energy k. The length scale L_s is determined from a second transport equation (dissipation rate of turbulence kinetic energy ϵ). The turbulent kinematic viscosity ν_t can then be expressed as:

$$\nu_t = C_\mu C_D \frac{k^2}{\epsilon} \tag{2.9}$$

The modified version of transport or conservation equations for the turbulence kinetic energy k and its dissipation rate ϵ for the liquid phase are shown as follows, while turbulence in the gas phase was neglected.

$$\nabla \cdot (R_l \rho_l \vec{V}_l k) - \nabla \cdot (R_l \rho_l \frac{\nu_t}{\sigma_k} \nabla k) = R_l \rho_l (P_k - \epsilon) + S_{k1} + S_{k2} \tag{2.10}$$

$$\nabla \cdot (R_l \rho_l \vec{V}_l \epsilon) - \nabla \cdot (R_l \rho_l \frac{\nu_t}{\sigma_\epsilon} \nabla \epsilon) = R_l \rho_l \frac{\epsilon}{k}(C_{1\epsilon} P_k - C_{2\epsilon}\epsilon) + S_{\epsilon1} + S_{\epsilon2} \tag{2.11}$$

where C_D, C_μ, $C_{1\epsilon}$, $C_{2\epsilon}$, σ_k and σ_ϵ are empirical constants. The standard values of these empirical constants are $C_D = 1.0$, $C_\mu = 0.09$, $C_{1\epsilon} = 1.44$, $C_{2\epsilon} = 1.92$, $\sigma_k = 1.0$ and $\sigma_\epsilon = 1.3$ (these are the values used in the calculations as well). P_k is the volumetric rate of generation of turbulence kinetic energy k, which takes the following form:

$$P_k = \mu_t(u_{i,j} + u_{j,i})u_{i,j} \tag{2.12}$$

S_{k1} and $S_{\epsilon1}$ on the right hand side of the transport equations for k and ϵ are the additional source terms which were introduced by Malin and Spalding [39]:

$$S_{k1} = C_{k1} \rho_l R_g R_l P_k \tag{2.13}$$

$$S_{\epsilon1} = C_{\epsilon1} \rho_l R_g R_l P_k \epsilon / k \tag{2.14}$$

and S_{k2} and $S_{\epsilon2}$ are the additional source terms which were introduced by Simonin

and Viollet [40]:

$$S_{k2} = C_{k2} R_g \rho_l C_f k \qquad (2.15)$$

$$S_{\epsilon 2} = C_{\epsilon 2} R_g \rho_l C_f \epsilon \qquad (2.16)$$

where C_{k1}, $C_{\epsilon 1}$, C_{k2}, $C_{\epsilon 2}$ are empirical coefficients. Conventionally these constants are set at $C_{k1} = C_{\epsilon 1} = 2.5$ and $C_{k2} = C_{\epsilon 2} = 0.5$. C_f is the inter-phase friction coefficient which will be explained in the following subsection.

Like most turbulence models, the extra terms in equations 2.10 and 2.11 cannot be justified from first principles. However some rationalization for their form can be presented. The terms proposed by Malin and Spalding [39] (equations 2.13 and 2.14) represent the added contribution to the shear distribution due to the presence of a plume since there is a general believe that for a given level of production P_k, the conventional $k - \epsilon$ model did not produce enough kinetic energy and dissipation. The terms from Simonin and Viollet [40] (equations 2.15 and 2.16) represent the additional shear generated by the rise of the bubbles. At the present stage of evolution of these models, it is not our attempt to exclude either set of the suggested additional terms from consideration.

2.2.4 Inter-Phase Momentum Transfer

The momentum transfer between the two phases is represented by the friction forces. The inter-phase friction force per unit volume at the gas liquid "interface" was given by:

$$\vec{F}_f = C_f(\vec{V_g} - \vec{V_l}) \qquad (2.17)$$

where C_f is the inter-phase friction coefficient which is defined as:

$$C_f = (3/4d_b)C_D|\vec{V_r}|\rho_l R_g \qquad (2.18)$$

where d_b is the diameter of the bubbles and C_D is the drag coefficient; $\vec{V_r}$ is the relative velocity vector between the two phases. The drag coefficient C_D is calculated as follows.

In the churn-turbulent flow regime ($R_g > 0.3$), where there is a continuous break-up and coalescence of bubbles, the drag coefficient was calculated by [27]:

$$C_D = \frac{8}{3}(1 - R_g)^2 \qquad (2.19)$$

while in the bubbly and mist flow regime ($R_g < 0.3$), where the bubble plume consists of well defined individual bubbles which do not interact greatly with each other, the drag coefficient was expressed as [41]:

$$C_D = \frac{24(1 + 0.15Re^{0.687})}{Re} + \frac{0.42}{1 + (4.25 \times 10^4/Re^{1.16})} \qquad (2.20)$$

where Re is the bubble Reynolds number based on the gas bubble diameter, defined as:

$$Re = V_{slip}d_b/\nu \qquad (2.21)$$

where the bubble size d_b was assumed constant and equal to 9 mm in most of the simulations, depending on the experimental information available. The effect of the bubble size on the fluid flow behavior will be analyzed in the next chapter.

2.2.5 Boundary Conditions

Boundary conditions were set to ensure a realistic representation of a system with bottom gas injection. The major difference between the various boundary conditions suggested in the literature was the boundary condition at the top free surface. The final adopted boundary conditions were:

1. On the symmetry axis or symmetry plane, symmetry conditions were used. Derivatives of all variables were set to zero.

2. At solid walls, velocities and turbulence parameters (k and ϵ) are set to zero.

3. In the vicinity of the solid walls, the shear stress and values of turbulence parameters (k and ϵ) are calculated by the standard wall function method based on a logarithmic law [37].

4. At the inlet of gas injection, uniform gas velocity was assumed and the turbulence kinetic energy k and its dissipation rate ϵ were calculated from the following empirical formula [24]:

$$k_{in} = 0.01 W_{in}^2 \qquad (2.22)$$

$$\epsilon_{in} = 0.6 k_{in}^{\frac{3}{2}}/r_o \qquad (2.23)$$

where W_{in} is the gas velocity at the nozzle inlet and r_o is the radius of the nozzle. Simulations proved that the fluid flow of the system is not sensitive to the boundary values of turbulence kinetic energy and its dissipation rate. This is presumably due to the zero fraction of the liquid phase in the inlet stream.

5. At the top free surface, a fixed pressure cond'tion was used. The vertical velocity of the liquid phase is set to zero. Gas was allowed to leave the reactor across this surface at a rate given by the natural boundary conditions (i.e., zero derivatives for related variables). In other words, gas was to leave the reactor at the rate at which it arrived at the top slab of cells.

6. At the inlet of liquid stream (for channel-type reactor only), uniform liquid velocity was assumed. The boundary values for turbulence kinetic energy and its dissipation were set as:

$$k'_{in} = I^2 U_{in}^2 \qquad (2.24)$$

$$\epsilon'_{in} = 0.1643 k'^{1.5}_{in}/l_m \qquad (2.25)$$

where I is the turbulent intensity (in the range of $0.01 \sim 0.05$) and l_m is a length scale ($\sim 0.1H$, where H is the height of the reactor).

7. At the outlet of liquid stream (for channel-type reactor only), a fixed pressure condition was used. Liquid was allowed to leave the system at the rate it reaches the exit of the reactor.

For details of the boundary conditions at each side of the boundaries, please refer to Table 2.2. It should be noted, however, that specific boundary conditions are

Table 2.2: Boundary conditions.

	Velocities	k	ϵ	Volume fraction
Solid walls	$U_{l,\parallel} = 0$	0	0	0
Nozzles	$U_{g,\perp} = W_{in}$	k_{in}	ϵ_{in}	$R_g = 1$
Top free surface	$\frac{\partial U_{l,\parallel}}{\partial x} = 0, U_{l,\perp} = 0$ $\frac{\partial U_g}{\partial x} = 0$	$\frac{\partial k}{\partial x} = 0$	$\frac{\partial \epsilon}{\partial x} = 0$	$\frac{\partial R_g}{\partial x} = 0$
Symmetry axis or plane	$U_\perp = 0, \frac{\partial U_\parallel}{\partial x_\perp} = 0$	$\frac{\partial k}{\partial x_\perp} = 0$	$\frac{\partial \epsilon}{\partial x_\perp} = 0$	$\frac{\partial R_l}{\partial x_\perp} = 0, \frac{\partial R_g}{\partial x_\perp} = 0$
Liquid inlet	$U_l = U_{in}$	k'_{in}	ϵ'_{in}	$R_l = 1$
Liquid outlet	$\frac{\partial U_l}{\partial x} = 0$	$\frac{\partial k}{\partial x} = 0$	$\frac{\partial \epsilon}{\partial x} = 0$	$\frac{\partial R_l}{\partial x} = 0$

** $\parallel$ means a variable parallel to the boundary and $\perp$ means a variable perpendicular to the boundary

further discussed in subsequent chapters, as the different configurations are presented.

2.2.6 Solution Procedure

The resulting governing equations were solved using the general purpose fluid flow and heat transfer package PHOENICS [36]. A finite volume technique based on a staggered grid was used to integrate the differential equations. The procedure of solving the equations involves the following sequence:

1. Guess the pressure shared by the two phases.

2. Solve for the volume fractions, using in-store velocities and volume fractions.

3. Solve the momentum equations using the new volume fractions and guessed pressure.

4. Define the representative continuity errors by weighting and adding the phase continuity equations.

5. Construct and solve the pressure correction equation.

6. Apply corrections to pressure and all velocities.

7. Repeat from step 2 until convergence is reached.

The convergence of the calculation was considered to be reached when the magnitude of the velocity and momentum imbalances, normalized with respect to their reference values, reached some preset criterion (0.1 here). In the present study, the reference values were set to be 0.001 m/s for the velocity and 0.001 kgm/s for the momentum, respectively. All the simulations were done on SUN Sparc workstations. Typical CPU times for the different configurations considered in this thesis are given in subsequent chapters.

2.3   Mixing Analysis

The analysis of mixing phenomena is an indispensable component in the understanding of the fluid flow behavior in a metallurgical reactor with bottom gas injection. Mixing time, average residence time, longitudinal mixing and other important mixing characteristics can be obtained by solving the time dependent tracer dispersion equation.

Having the same thermophysical properties of the liquid, the tracer is considered as a second component in the liquid phase. Thus, the tracer dispersion equation can be written as:

$$\frac{\partial}{\partial t}(R_l \rho_l c) + \nabla \cdot (\vec{V}_l R_l \rho_l c) = \nabla \cdot (R_l \Gamma_{eff} \nabla c) \tag{2.26}$$

where c is the tracer concentration in the liquid phase and Γ_{eff} is the effective mass diffusion coefficient, which is defined as

$$\Gamma_{eff} = \frac{\mu}{Sc} + \frac{\mu_t}{Sc_t} \tag{2.27}$$

Sc and Sc_t are laminar and turbulent Schmidt numbers, respectively, being defined as:

$$Sc = \frac{\mu}{D} \tag{2.28}$$

and

$$Sc_t = \frac{\mu_t}{D_t} \tag{2.29}$$

where D and D_t are the laminar and turbulent diffusivity, respectively. The turbulent Schmidt number was taken to be unity in this study.

The boundary conditions used to solve the tracer dispersion equation is quite straight forward. Depending on the configurations of the reactor, a pulse input of tracer is injected from different locations of the reactor. Time dependence of the tracer concentration is calculated. A natural boundary condition is used at the outlet of the reactor.

The tracer dispersion equation (2.26) is solved after a steady-state flow field has been obtained, since we can readily assume that the injection of tracer does not affect the flow behavior in the bulk (i.e., uncoupled solutions).

2.3.1 Mixing Time

Mixing time is a useful concept to characterize mixing behavior for a cylindrical reactor with bottom gas injections. There are many different suggestions as to how to define the mixing time in a reactor. A general accepted definition is that mixing time is the time that is required for some small amount of tracer added into the liquid from a particular location, to reach an uniformity of 95%. We will use this definition to refer to mixing time in this document.

In a cylindrical reactor, a tracer is injected from a prescribed position and the evolution of tracer concentration is obtained by solving the tracer concentration equation (2.26) in a frozen (already converged) fluid flow field. Concentration map as a function of time was monitored until the difference between the maximum and the minimum concentrations in the whole computational domain is within 5% of the equilibrium concentration. The time at which the system reaches this point is recorded as the mixing time of the system.

2.3.2 Longitudinal Mixing

For a channel-type reactor, there is a steady stream of liquid entering and leaving the system continuously. Therefore, mixing time is more difficult to define for a

channel-type reactor using the same concepts described in the above section with respect to cylindrical (batch) reactors. Instead, a concept called dispersion number (inverse Peclet number Pe^{-1}) was used to analyze the degree of longitudinal mixing behavior in a channel-type reactor. In the rest of this document, dispersion number, Levenspiel number and inverse Peclet number will be used interchangeably. The technique adopted to study longitudinal mixing in the channel-type reactor, which is called residence time distribution (RTD) method, has been widely employed in chemical engineering for the analysis of chemical reactors. The main concepts involved are described in Appendix A.

For a continuous system, the tracer dispersion equation can be solved for steady state conditions. Therefore, the first term of the tracer dispersion equation (2.26) will be dropped when a continuous reactor is being considered.

The so-called C-curves can be obtained by injecting a pulse tracer at the reactor inlet and plotting the tracer response at the reactor outlet. The actual mean residence time of the liquid in the reactor can be obtained by integrating the C-curves [42], using the following formula:

$$\bar{t}_{mean} = \frac{\int_0^\infty ctdt}{\int_0^\infty cdt} \qquad (2.30)$$

In order to compute the inverse Peclet number D_e/uL, one has to calculate the statistical variance σ^2, or square of the standard deviation, which is defined by:

$$\sigma^2 = \frac{\int_0^\infty c(t - \bar{t}_{mean})^2 dt}{\int_0^\infty cdt} \qquad (2.31)$$

and then the inverse Peclet number can be calculated from:

$$\sigma^2 = 2D_e/uL - 2(D_e/uL)^2(1 - e^{-\frac{uL}{D_e}}) = 2Pe^{-1} - 2Pe^{-2}(1 - e^{-Pe}) \qquad (2.32)$$

The dimensionless group D_e/uL, the inverse Peclet number, is the parameter which represents the degree of longitudinal dispersion (or degree of deviation from the plug flow behavior for a channel-type reactor). For plug flow reactors, D_e/uL is

41

zero, while it is infinity for perfectly mixed tank reactors.

2.4 Mass Transfer Analysis

The differential equation used to carry out the mass transfer analysis involves the conservation of species being transferred from the main liquid phase to an upper liquid phase, by means of convective motion in the bulk liquid and chemical reactions at the interface. For the continuous channel-type reactor, there is a steady stream of lower and upper phases entering and leaving the system, thus, the equation can be solved as a steady state, i.e.,

$$\nabla \cdot (\vec{V_l} R_l \rho_l c_m) = \nabla \cdot (R_l \Gamma_{eff} \nabla c_m) \qquad (2.33)$$

where c_m is the species concentration in the lower liquid phase. The differential equation must be solved subjected to the following boundary conditions:

At the walls: $\frac{\partial c_m}{\partial z} = 0$ at $z = 0$ (bottom wall)

$\frac{\partial c_m}{\partial y} = 0$ at $y = \frac{W}{2}$ (side wall)

At the symmetry plane: symmetry boundary conditions.

At the "two-phase" interface: flux $J = k_o(c_m - \frac{c_s}{P_s})$ at $z = H$

At the reactor inlet: $c = c_i$ at $x = 0$

At the reactor outlet: $\frac{\partial c}{\partial x} = 0$ at $x = L$

where H is the height and W is the width of the reactor; k_o is an overall mass transfer coefficient; c_s is concentration in the upper liquid phase and P_s is the equilibrium partition ratio of the species between the two liquid phases.

The value of the overall mass-transfer coefficient k_o depends on the geometry of the system, stirring conditions, the viscosities and densities of the two phases, and the surface tension between the two phases. A detailed description of the use of this mass transfer analysis method is given in Chapter 5, together with the assumptions under which the mass transfer equation is established.

2.5 Particle Tracking

Particle tracking techniques are primarily used to visualize the flow pattern and to apply some statistical analysis on the residence time distribution of the fluid "particles" in the system. A technique called "GENTRA" [45] was used to carry out the particle tracking analysis from a Lagrangian point of view. The governing equation underlining the particle tracking method is the classical Newton's motion law, considering the various forces acting on the particles as they are affected by the fluid motion. The general equation for a particle moving along the liquid can be expressed as follows:

$$\frac{dV_i}{dt} = -\frac{3}{4}\frac{\mu}{\rho_p d_p^2}C_D Re(V_i - u_i) - \frac{\rho_l}{\rho_p}u_j\frac{\partial u_i}{\partial x_j} + (1 - \frac{\rho_l}{\rho_p})g_i \qquad (2.34)$$

where V_i and u_i represent the instantaneous velocity of the "particles" and the time-averaged liquid phase velocities (i=1, 2, 3), respectively; ρ_l and ρ_p are the densities of the liquid and the particle, respectively. d_p is the diameter of the particle and C_D is the drag coefficient which was described early in this chapter; Re is the particle Reynolds number and g_i is the gravitational acceleration. The terms on the right hand side of the equation represent the drag, pressure and gravitational effects, respectively.

The kind of particles used to conduct particle tracking are called "lazy" particles in this study and they have the following characteristics:

1. "Lazy" particles do not have a velocity of their own, but share, at each point, the continuous-phase velocity. They therefore behave like tracers in the fluid.

2. Lazy particles do not have a size or temperature and have no effect on the continuous-phase behavior.

3. On hitting a wall or obstacle, the lazy particle will be removed from the computational domain.

A stochastic turbulence model [46] was used when trajectories of particles were solved. The stochastic turbulence model accounts for the effects on particle dispersion of the turbulence fluctuations of the continuous-phase velocity. Trajectories of the "lazy" particles were then obtained by integrating the Newton's equations.

Chapter 3

Cylindrical Reactors

3.1 Reactors with Central Bottom Gas Injection

3.1.1 Fluid Flow and Turbulence

A cylindrical reactor (also called ladle in the steel making industry) with a central bottom injection represents a good starting point for building and testing the mathematical model described in the previous chapter since the system is axisymmetric (essentially two dimensional in cylindrical polar coordinates) and there is a large amount of experimental results available to compare the computed results with in order to validate the model. A schematic representation of the system is shown in Figure 3-1 where a stream of gas is rising from the bottom of the reactor. The gas interacts with the surrounding fluid and a recirculation pattern is then generated.

A cylindrical polar coordinate system was used in this study because the reactor is axisymmetric. The origin of the coordinates was placed at the center of the nozzle exit, and the axial and radial coordinates were denoted by z and r, respectively. Different grids were used to test the sensitivity of the number of cells used on the computed results. A nonuniform grid of 20×20 was selected for the axisymmetric system mentioned above. The grid node density was highest close to the walls, the free surface and the nozzle, as can be seen in Figure 3-2 where the computational domain is shown.
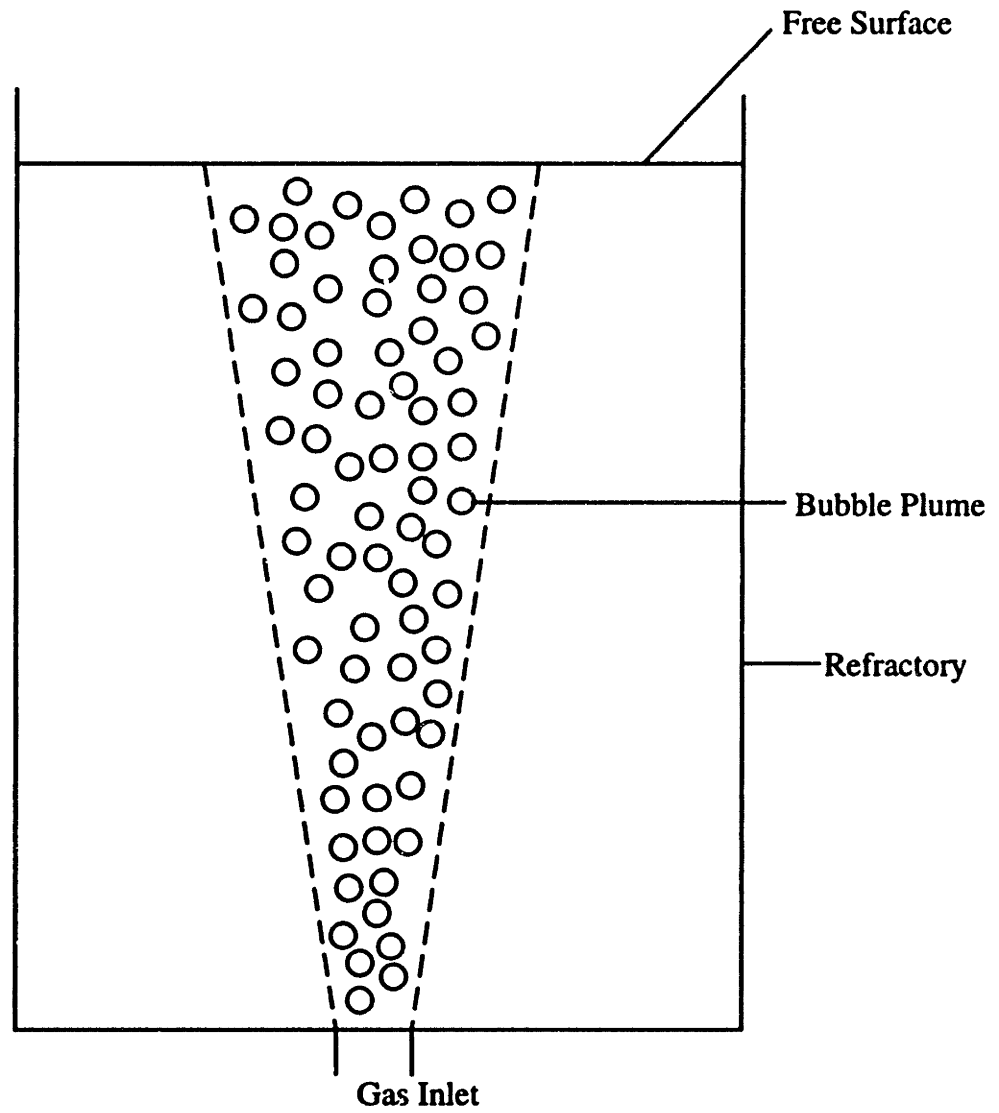
Figure 3-1: A schematic representation of a ladle with a central bottom gas injection (not in scale).

Table 3.1: Conditions of experimental measurements chosen to compare the model results with.

Conditions	Case 1	Case 2
	Iguchi et al. [52]	Sheng & Irons [16]
System	Water/Nitrogen	Water/Air
Diameter (m)	0.2	0.5
Height (m)	0.25	0.42
Gas flow rate (Nm^3/s)	41.4×10^{-6}	$50, 150\times10^{-6}$
Nozzle diameter (m)	0.002	0.004

Table 3.2: Physical properties of fluids used in the experiments.

Fluid	Density (kg/m^3)	Kinematic viscosity (m^2/s)
Water	1000.0	1.0×10^{-6}
Nitrogen	1.138	1.565×10^{-5}
Air	1.189	1.544×10^{-5}

Two independent sets of experimental measurements reported in the literature [4, 16] were used to validate the mathematical model developed. The conditions of these two experiments are shown in Table 3.1.

The nozzle Reynolds number, calculated by $4Q\rho_g/\pi\mu d_o$, is 1685 in case 1 and 1031 & 7376 in case 2 which shows fluid flows in both cases are in the turbulence regime. The physical properties of materials involved in both experiments are shown in Table 3.2. A typical calculation used 3000 sweeps for the mesh mentioned above and required about 0.5 hours CPU time on a SUN Sparc 20 workstation.

Grid Sensitivity Analysis The precision of computer simulation depends a great deal on the grid used to represent the system. Grid sensitivity analysis is important for obtaining enough precision, as well as for avoiding over-fine grid that would become computationally too expensive. Grid sensitivity tests were performed and the results are shown in Figure 3-3 where a grid of 10×10 seems too coarse while no significant difference is seen between the results from the grids of 20×20 and 25×25. A grid of 20×20 was chosen considering the much longer CPU time it would take in calculations performed with a grid of 25×25.

Surface

Wall

Nozzle
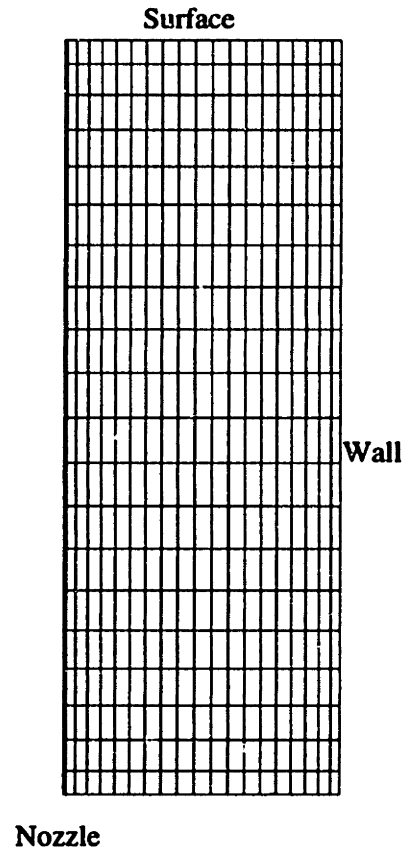
Figure 3-2: The computational domain and the grid used (only a half of the system is shown).
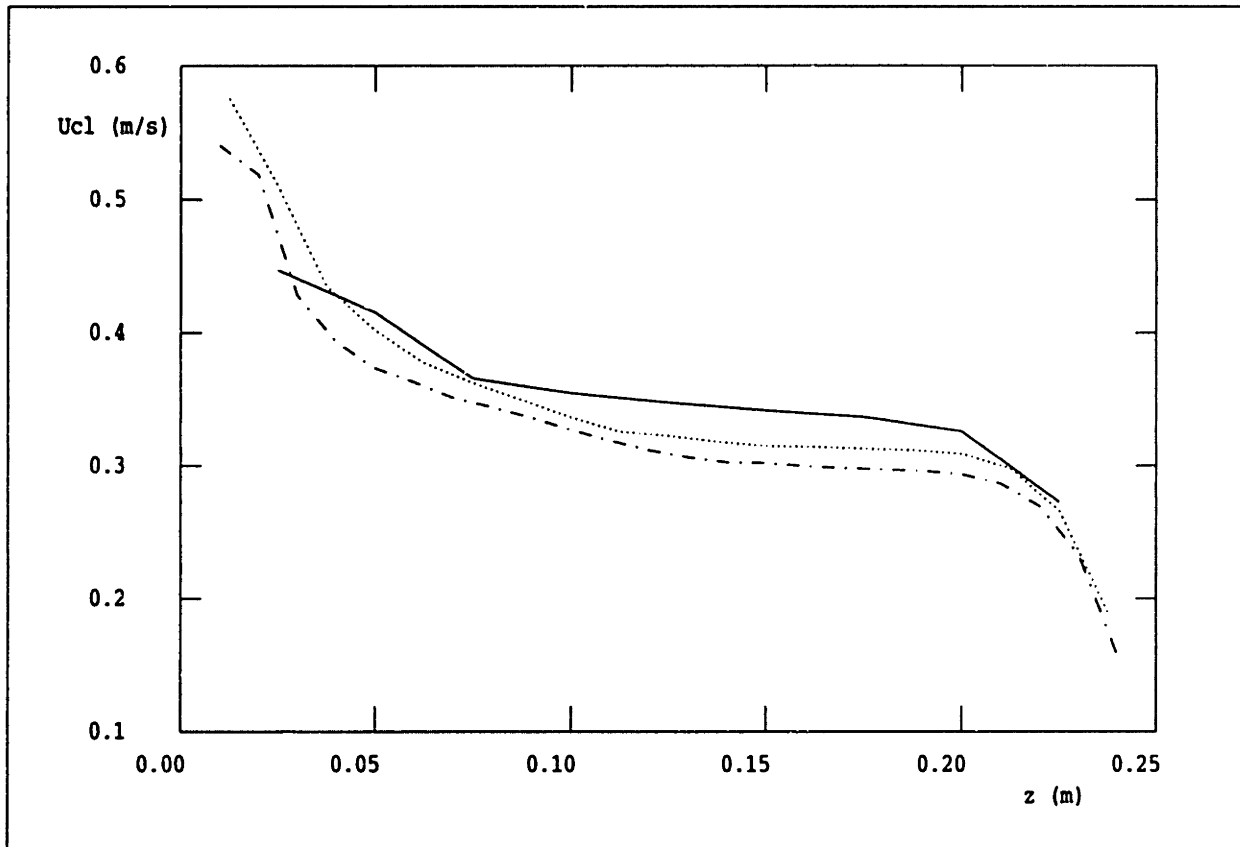
Figure 3-3: A comparison between the velocities at the centerline in Case 1 shows grid sensitivity (solid line – 10×10, short dashed line – 20×20, dash-dotted line – 25×25).

Table 3.3: Experimental correlations for calculating bubble size.

Investigators	Correlations
Mori et al. [49]	$d_b = \{(\frac{6\sigma_l d_n}{\rho_l g})^2 + 0.0242(Q^2 d_n)^{0.867}\}^{1/6}$
Davidson & Schuler	$d_b = 0.25 d_{max} = 0.25(0.35(Q^2/g)^{0.2})$
Sano et al. [48]	$d_b = 0.091(\frac{\sigma}{\rho_l})^{0.5} U_g^{0.44}$
Davidson & Amick [51]	$d_b = \{(\frac{6\sigma_l d_n}{\rho_l g})^2 + (0.54(Q d_n^{0.5})^{0.289})^6\}^{1/6}$
Anagbo et al. [50]	$V = 1.57(Q^2/g)^{0.6}$, $d_b = (\frac{6V}{\pi})^{1/3}$

Bubble Size Different empirical correlations from literature were used to calculate the bubble size and the effect of bubble size on simulation results are shown in Figure 3-4 using parameters in Case 1. The empirical correlations were chosen in this work are given in Table 3.3. It is seen that there is no obvious preferences as to which empirical correlation should be chosen to calculate the bubble size. Therefore, a constant size of 9 mm, which is obtained from experimental measurements in Case 1, was used in most of the simulations.

Simulation Results Velocity field, gas volume fraction distributions, turbulence kinetic energy and its dissipation rate were computed. The comparison between the predictions and experimental data are shown and analyzed for both cases referred earlier. Figure 3-5 to 3-10 are related to Case 1, while Figure 3-11 and 3-12 are related to Case 2.

Figure 3-5 shows the computed average velocity field of the liquid phase for Case 1 where a single recirculation "eye" at the upper half of the system can be observed which is consistent with experimental observations by numerous researchers. The fluids at the right and left bottom corners seem pretty quiescent, indicating possible "dead zones".

Figure 3-6 shows the computed average axial velocity of the liquid at the centerline of the reactor and the comparison with the experimental results obtained by Iguchi et al. [52]. It can be seen that the agreement is very good except in the regions close to the nozzle and possibly at the top free surface. The discrepancy at the free surface is believed from the artificial flat top boundary condition used in the mathematical model.
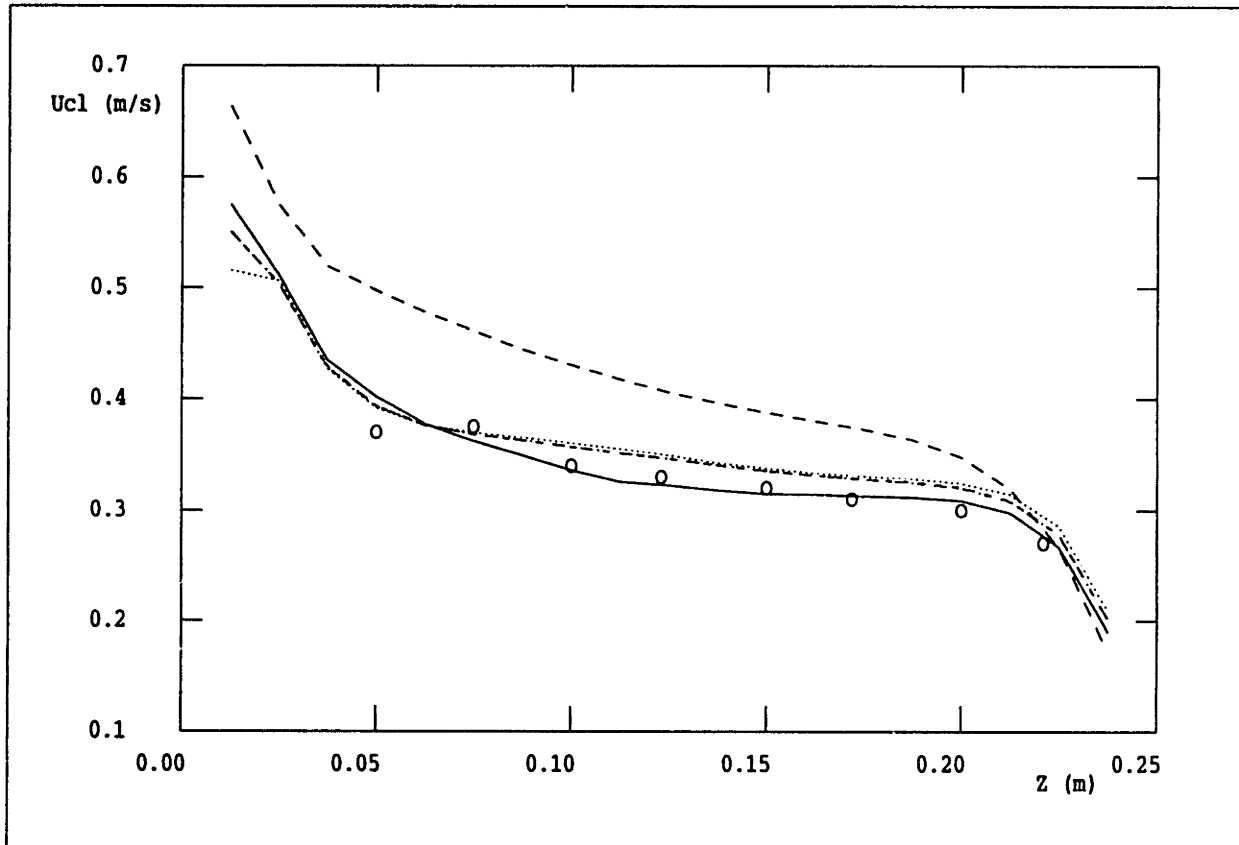
Figure 3-4: The effects of bubble size calculated from different experimental correlations (solid line - 9 mm, dotted line - Anagbo et al., short dashed line - Davidson & Amick, long dashed line - Mori et al., dash-dot line - Davidson & Schuler, circles - experimental data).

50
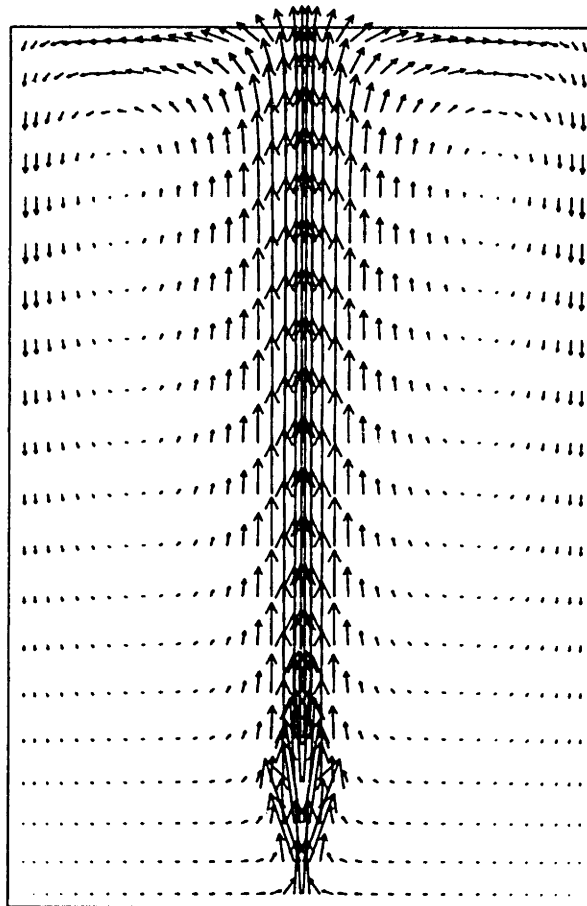
$\longrightarrow$ 0.60 m/s

Figure 3-5: The predicted average velocity field of liquid phase for Case 1.
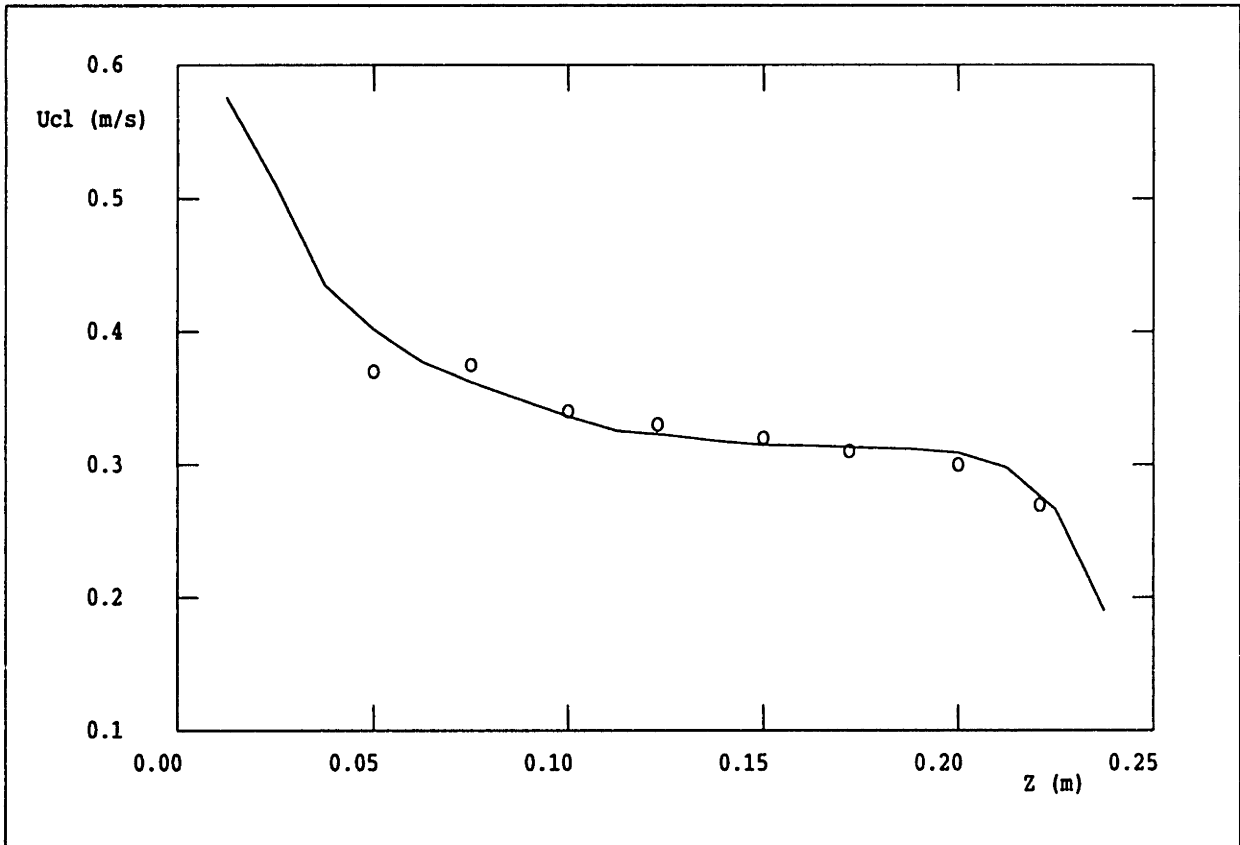
Figure 3-6: Comparison between the predicted average axial liquid velocity at the centerline of the system and the experimental results obtained by Iguchi et al. (solid line - prediction, circles - experimental data).

Figure 3-7 plots the prediction of axial velocity profile at a height of z = 20 cm and the comparison with the experimental results obtained by Iguchi et al. [52], which are also represented by a Gaussian error curve correlated from these experimental measurements. In this figure b_u represents a half-value radius of the axial mean velocity and U_{cl} is the axial velocity at the centerline at the height of z = 20 cm. Again, it is seen that the agreement shown is indeed very good except in the region close to the wall. The Gaussian error curve is represented by the following correlation:

$$\bar{U} = \bar{U}_{cl} \exp(-cr^2/b_u^2) \tag{3.1}$$

where the constant $c = \ln 2$.

Figure 3-8 is a plot showing the computed gas volume fraction (gas holdup) along the centerline of the system and the comparison with the experimental results obtained by Iguchi et al. [52]. It is seen that some discrepancy appears, especially in the region close to the nozzle.

Figure 3-9 shows the computed root-mean-square values of the turbulence components of the axial velocity along the centerline of the system and the comparison with the experimental measurements [52]. Since a two-equation turbulence model was used, the calculated root-mean-square values of turbulence components of velocity are the same in both axial and radial directions (isotropic). The comparison shows that the agreement is reasonably good considering the assumption of isotropy.

It should be noted that the sharp peak shown in the plot is believed from the high gas volume fraction close to the nozzle (as high as 1.0) since only liquid phase turbulence is considered in this study and the root-mean-square velocity components are calculated directly from the turbulence kinetic energy of the liquid phase. This is an inherited drawback from the two-phase model and it is considered no significant effect in capturing the important features of the flows in the bulk.

Figure 3-10 shows the computed turbulence kinetic energy and its dissipation rate fields. By considering the fact that mixing intensity in the system is related to the value of the turbulence kinetic energy dissipation rate ϵ, it can be suggested that

53
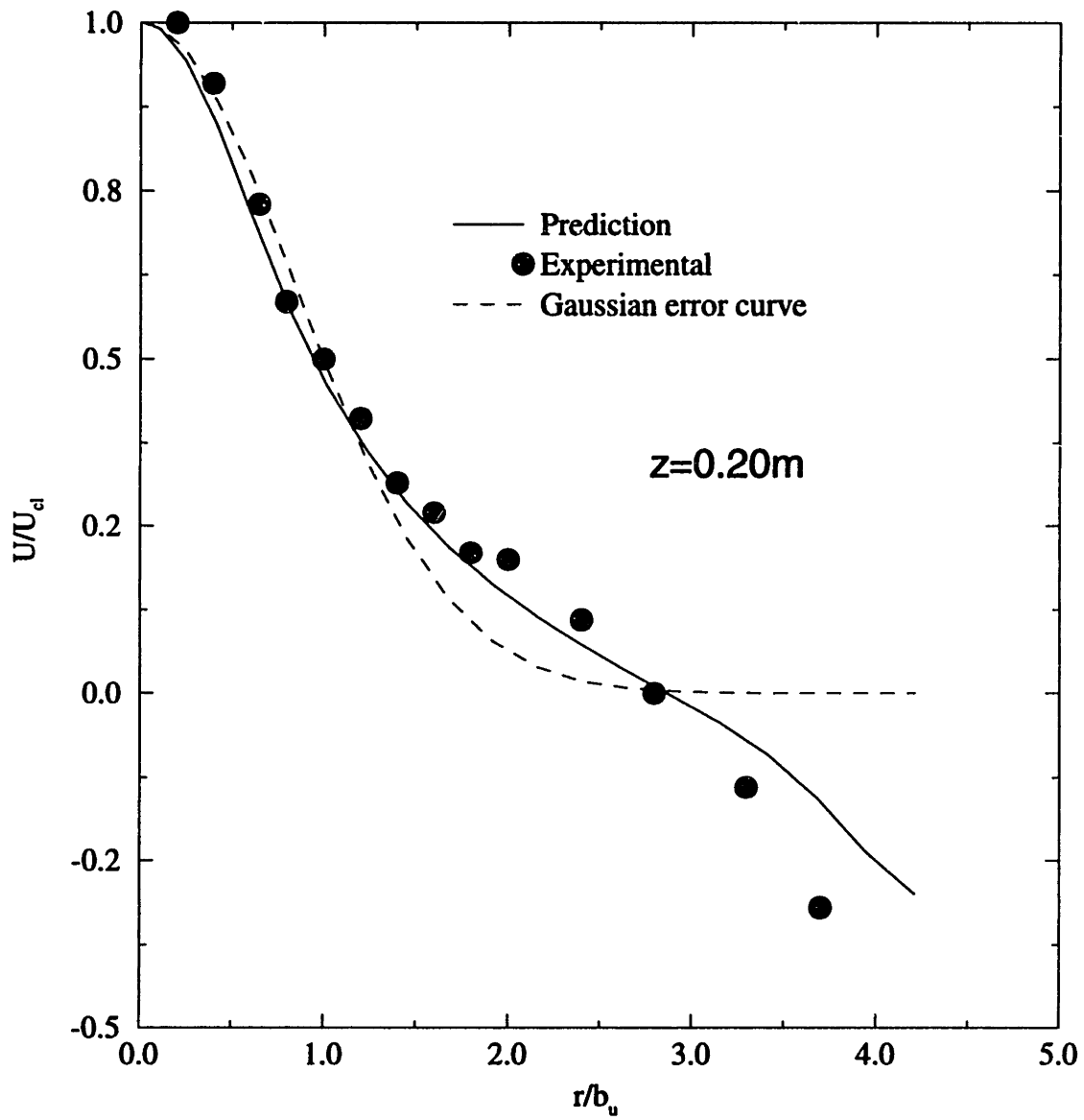
Figure 3-7: The predicted average axial liquid velocity along the radial direction at z = 20 cm and the comparison with experimental results from Iguchi et al., which are also shown as a Gaussian error curve.
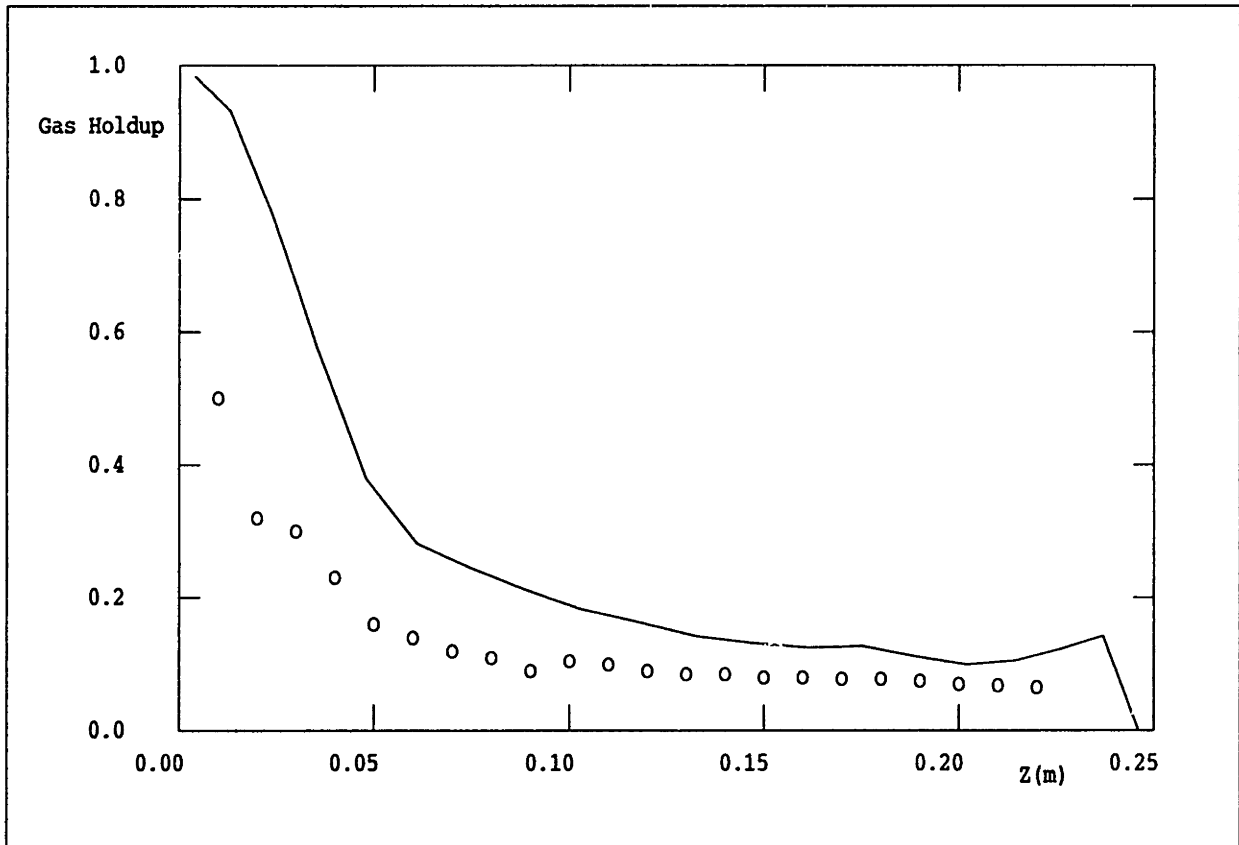
Figure 3-8: Comparison between the predicted gas volume fraction at the centerline of the system and the experimental results obtained by Iguchi et al. (solid line - prediction, circles - experimental data).
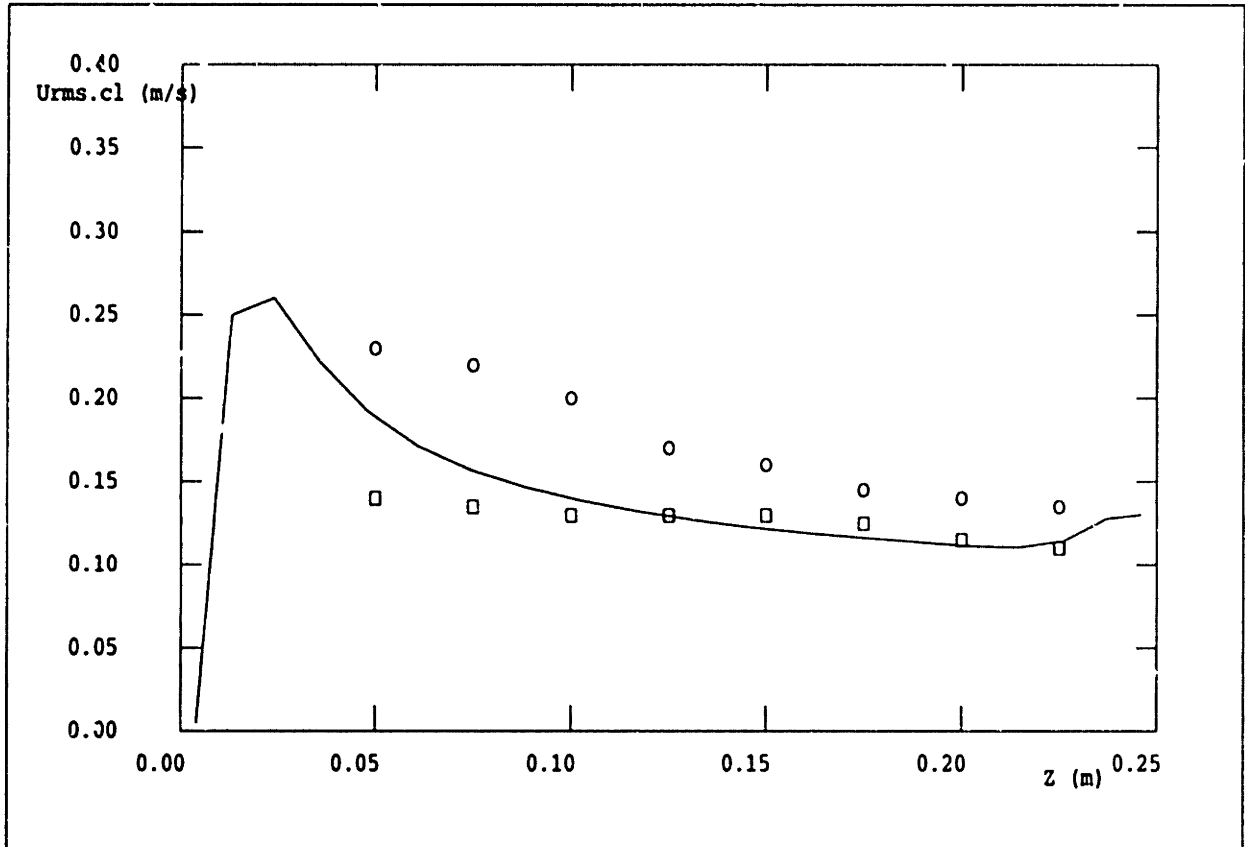
Figure 3-9: The predicted root-mean-square values of axial turbulence velocity component at the centerline of the system and the comparison with experimental results obtained by Iguchi et al. (solid line - prediction, circles - axial components, squares - radial components).

mixing is mainly promoted in the plume region. It is important to note that with the aid of mathematical modeling, the shape of the plume, turbulence kinetic energy and its dissipation rate can be predicted from first principles.

Figure 3-11 shows a comparison between some additional experimental measurements obtained by Sheng and Irons [16] and the predicted axial velocity profiles at the centerline for two different gas flow rates. It is seen that a reasonably good agreement is obtained in this comparison. It should be noted, however, that some discrepancy in the predictions is observed in the vicinity of the nozzle region.

Figure 3-12 shows a comparison between experimental measurements from Case 2 and the predicted radial profile of the axial velocity at a height of 21 cm from the bottom (experimental measurements were only available for gas flow rate of 50 mi/s). In contrast to the previous plot, it is seen that an excellent agreement is obtained in this case.

3.1.2 Mixing

Mixing helps to promote homogenization and enhance chemical reactions by bringing reactants together and removing products from reaction sites. It is therefore desirable to know the degree of mixing in order to evaluate the performance of gas-stirred reactors.

From a practical point of view when dealing with mixing, one would expect a minimum time for a reactor to reach uniformity after injecting some additives to the melt. Here, two issues need to be considered, namely the optimal location for addtions and the actual homogenization time or mixing time involved.

Among the literature related to the analysis of mixing time in gas-stirred cylindrical reactors, two different suggestions are available involving the criteria to define the degree of mixing. One group of researchers [55] suggests that mixing time is independent on the location, within the system, where the tracer is added, as well as on the location where measuring probes are placed. In contrast, another group of researchers [81, 54] suggests that mixing time does depend on where the tracer is added and where the measuring probes are placed. To further investigate this issue,
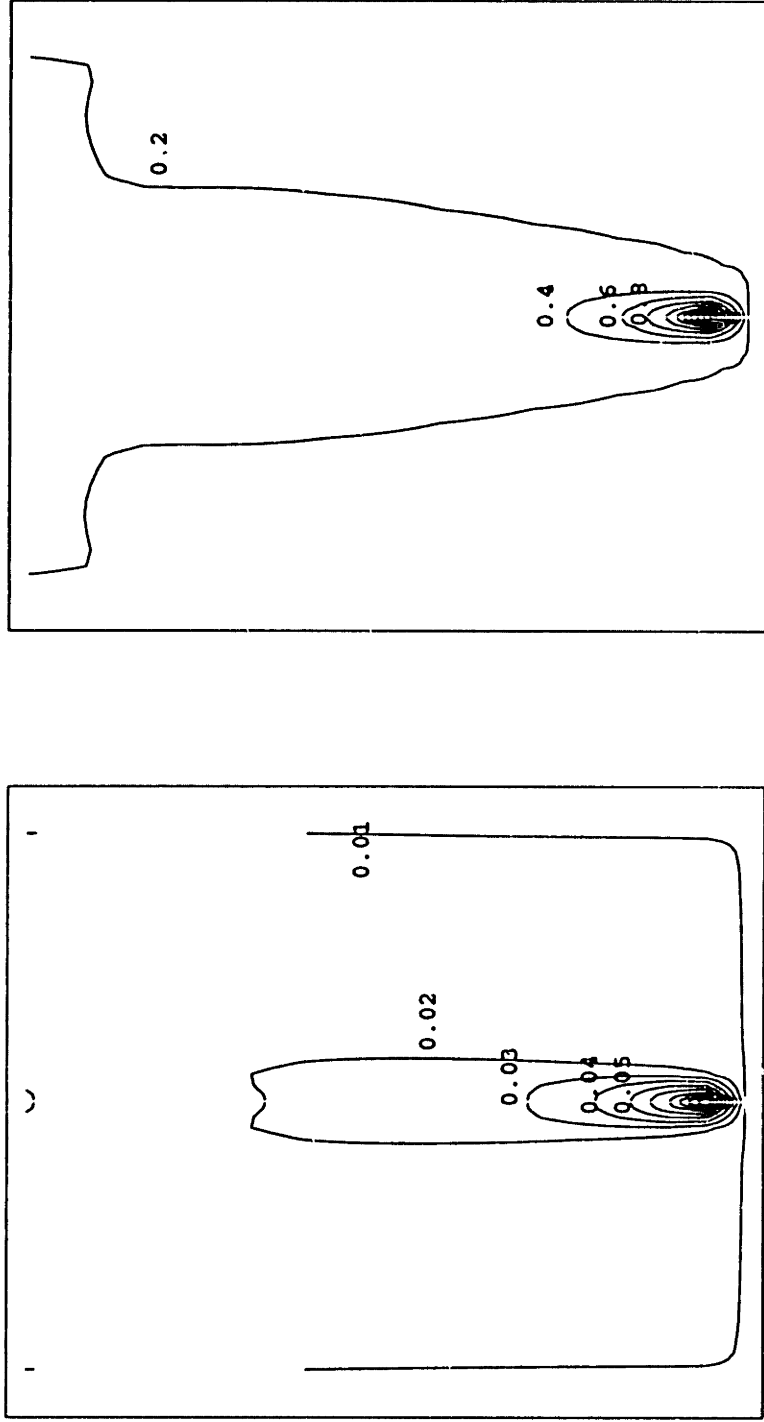
Figure 3-10: The predicted turbulence kinetic energy (J/kg) and its dissipation rate (J/kg·s) field.
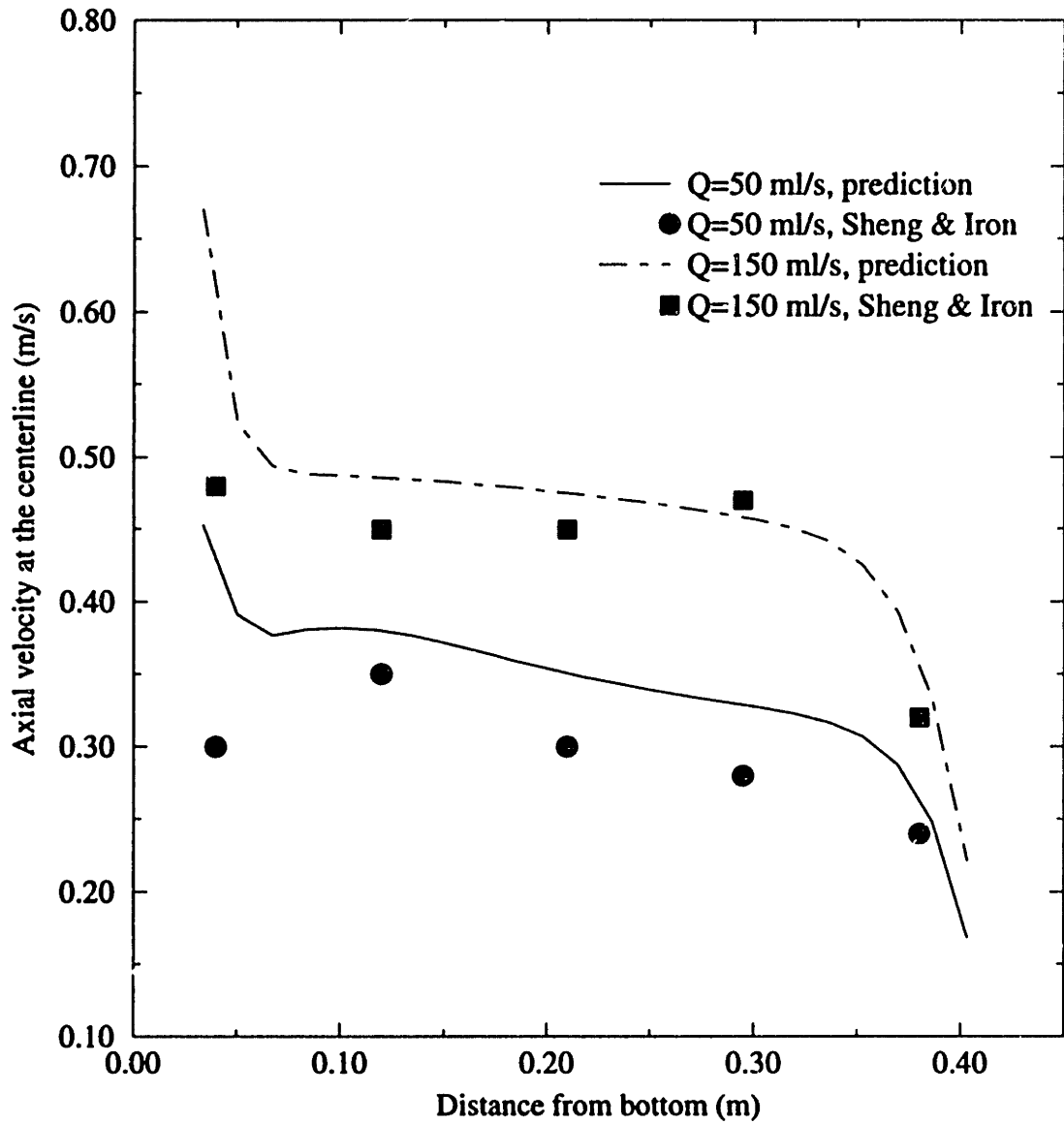
Figure 3-11: Predicted axial velocity at the centerline compared with experimental data by Sheng and Irons.
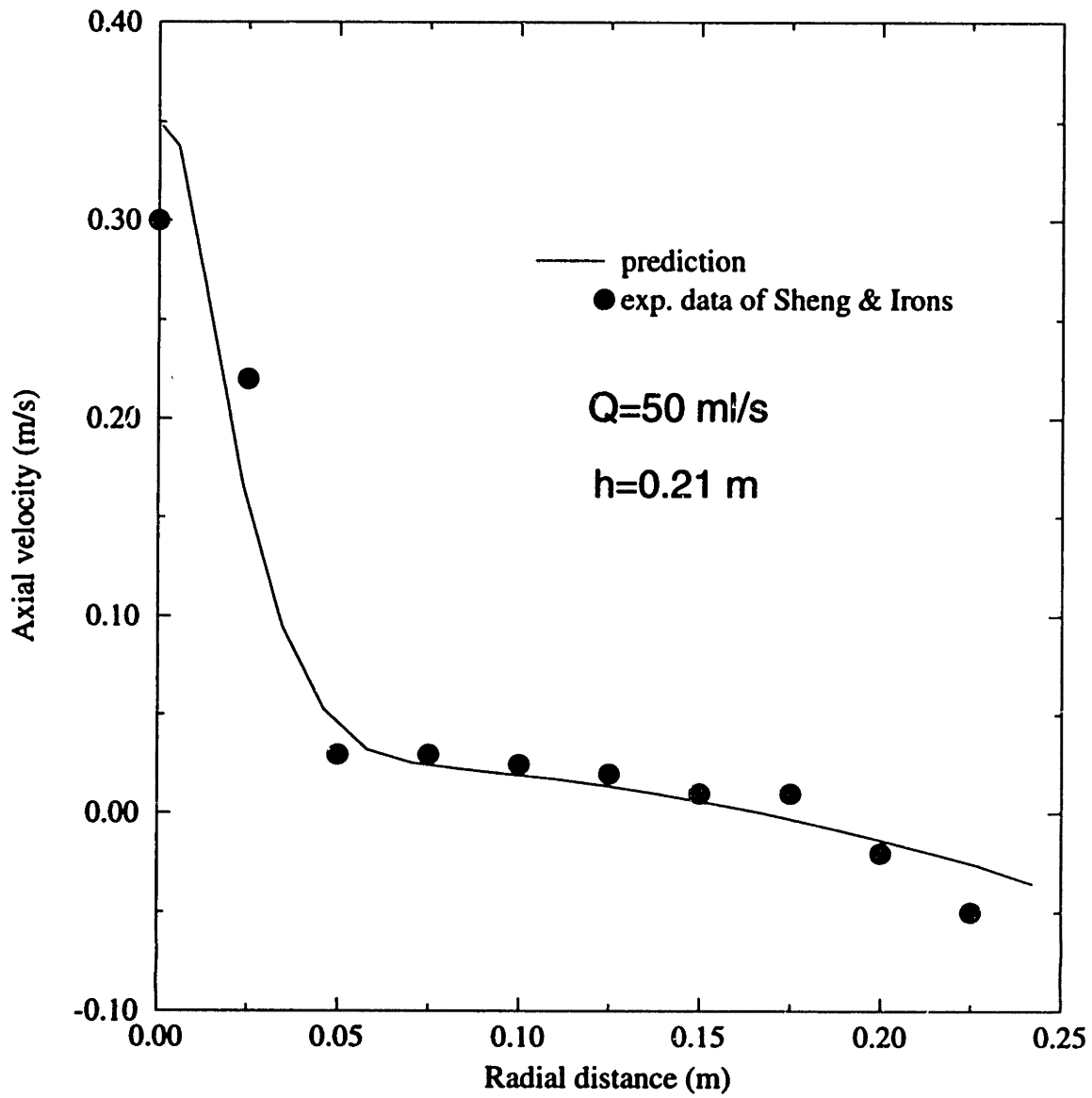
Figure 3-12: Predicted axial velocity at h = 0.21 m with experimental data by Sheng and Irons.

a thorough test was conducted in this work to analyze how mixing time is affected by tracer addition points. The effect of monitoring locations was not considered in this study.

The way to compute the mixing time in a cylindrical reactor in batch operation (i.e., there is no steady flow in and out of the system) was as follows: After obtaining the steady state velocity field of the system, a pulsed injection of concentration was introduced into the system from one of the simulation cells. A transient tracer dispersion equation was solved and the changes of concentration as a function of time was recorded for all the cells in the computational domain. When the difference between maximum and minimum concentrations, normalized by the equilibrium concentration, reached 5%, the time span was taken as the overall mixing time in the system. In this way, the effect of tracer monitoring point was isolated out from the effect of tracer addition point. The same calculation was repeated taking a different cell as the location of addition, and as a result of sweeping of every cell, the whole computational domain was visited.

Figure 3-13 shows the evolution of two typical concentration curves as a function of time. The tracer injection position was at cell (15,15) in this case, and the two measuring points were (18,18) and (10,15), respectively. It is seen that different mixing times would be obtained if measuring probes were placed at these different locations.

Figure 3-14 represents different time frames showing the evolution of the tracer concentration right after it was introduced into the system. The tracer addition point was at cell (5, 15). It can be seen that the injected tracer generally follows the overall recirculation of the liquid and diffuses in the direction perpendicular to the recirculation.

A very thorough analysis, in which every computational cell was used as a tracer injection point, was carried out to investigate the effect of tracer injection locations on the mixing time in the system. The mixing time corresponding to each simulation cell was recorded and a mixing time map was plotted. Two rather different gas volume flow rates were used to clear out the confusion, they were $41.4\,Ncm^3/s$ and

61
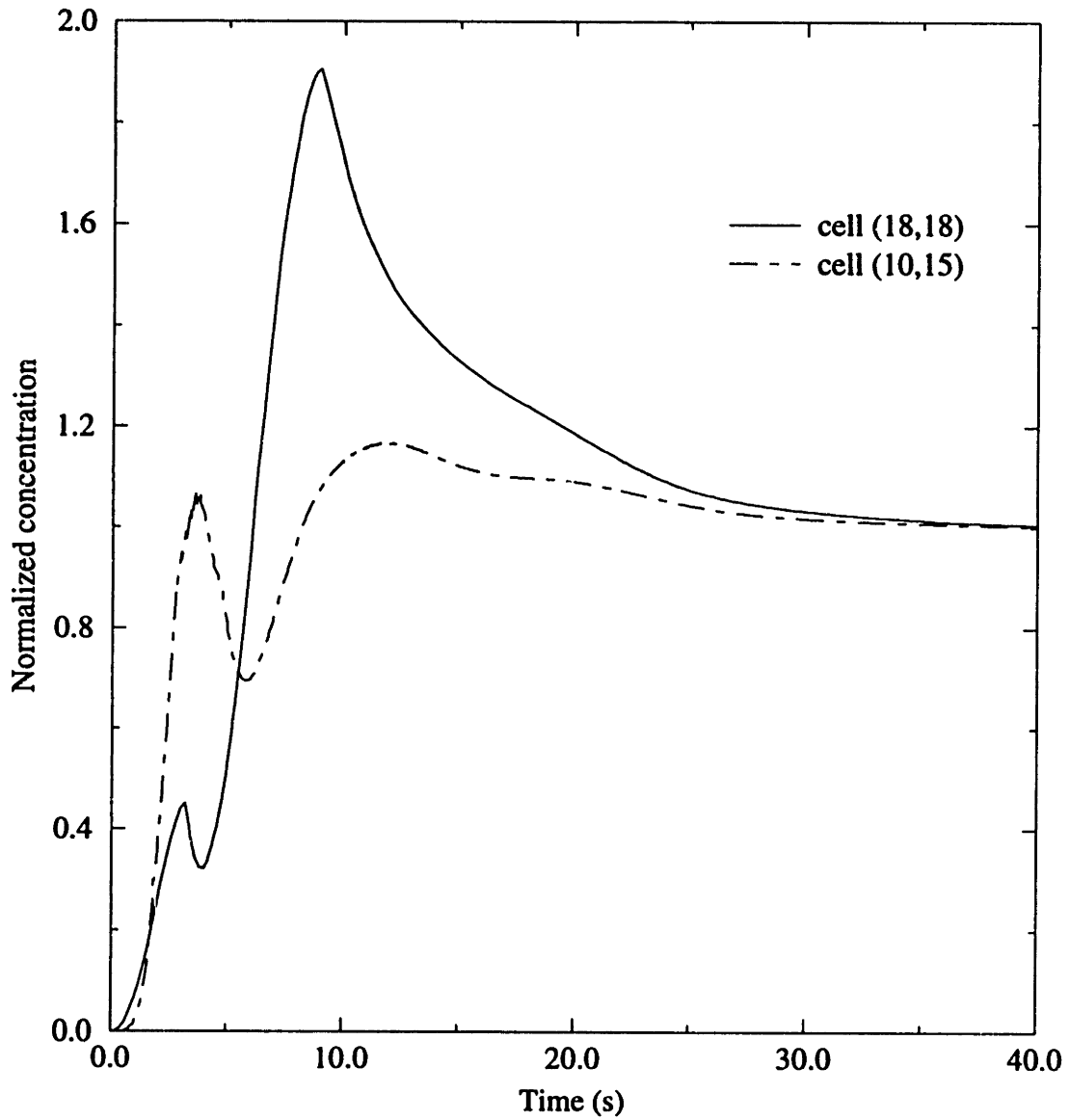
Figure 3-13: Normalized concentration as a function of time by measuring tracer concentration from two different locations.
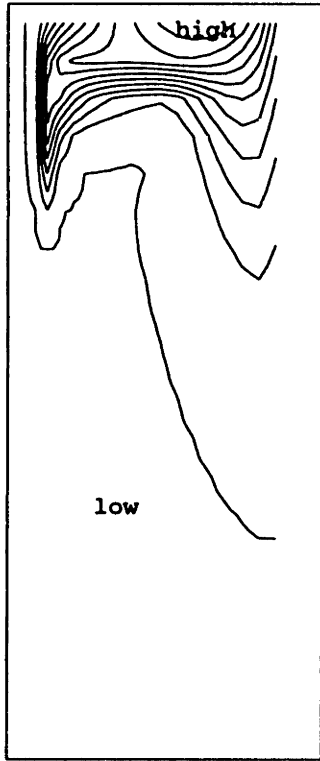
(a) t = 1 s
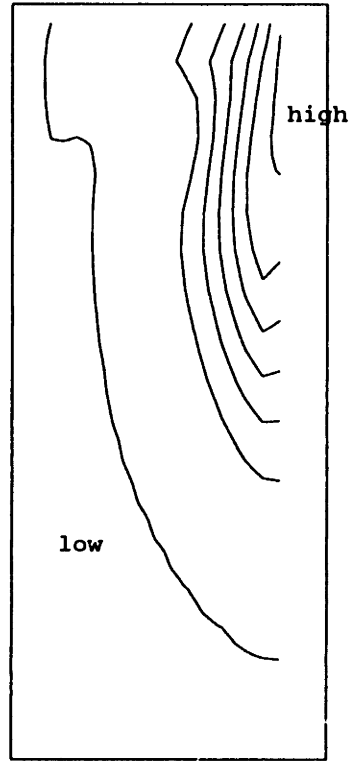
(b) t = 2 s
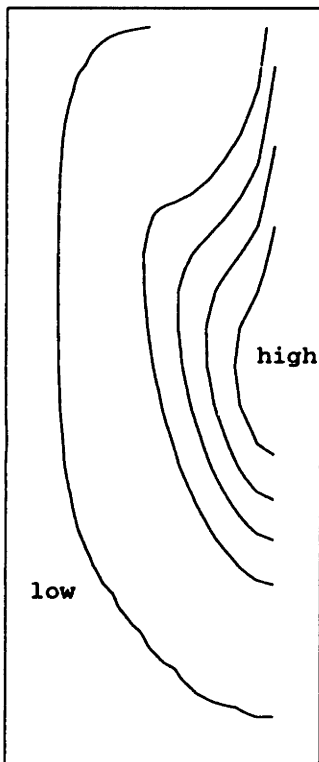
(c) t = 3 s
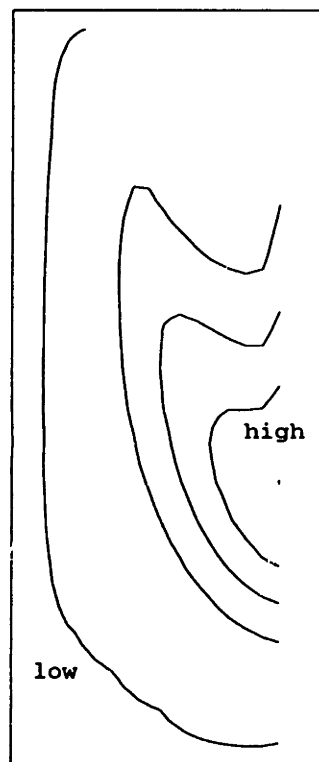
(d) t = 4 s

Figure 3-14: Time frames showing how the tracer concentration changes as a function of time in a cylindrical reactor with central bottom gas injection.

63

331.2 Ncm^3/s, respectively. The later one is eight times of the first one in magnitude. A comparison is shown in Figure 3-15 plotted as contours of mixing time.

It is shown in the figure that the effect of tracer addition locations on the mixing time follows the same pattern even though the gas volume flow rates are quite different for the two systems. These results support the suggestion that mixing time does depend on the tracer addition positions. Another point to be noted is that, contrary to intuition, the maximum time for complete mixing is when the tracer is added at the recirculation "eye" of the system. The region at the lower left corner of the plots represents another location where added tracer takes a long time to reach the whole system. The optimal tracer addition region is right outside the plume region, which consists of an area located around one third of the radius.

Further analysis of the results presented in Figure 3-15 indicates that an increase of 700% of gas volume flow rate results in an increase of mixing time of about 63%. The maximum values of local mixing times are 40 s and 16 s corresponding to the center loops, respectively.

3.1.3 Parametric Analysis of Operating Conditions

In order to investigate the mixing behavior of the system affected by several operating parameters (such as gas volume flow rate, reactor aspect ratio and nozzle size), a large number of simulations were carried out. The effect of each parameter on mixing time was studied by changing this particular parameter while others were kept constant. The results are shown and discussed in the rest of this section.

Gas Flow Rate Several gas flow rates were used to investigate their effect on the mixing time of the reactor. Three tracer injection points, which were (5,5), (10,10) and (15,15), were used here. The mixing times and their averages were calculated and the results are shown in Figure 3-16. The tendency of decreasing mixing time as gas flow rate increases is clearly shown in the figure. It should be also noted that an asymptotic behavior is shown at high gas flow rates. A correlation from the
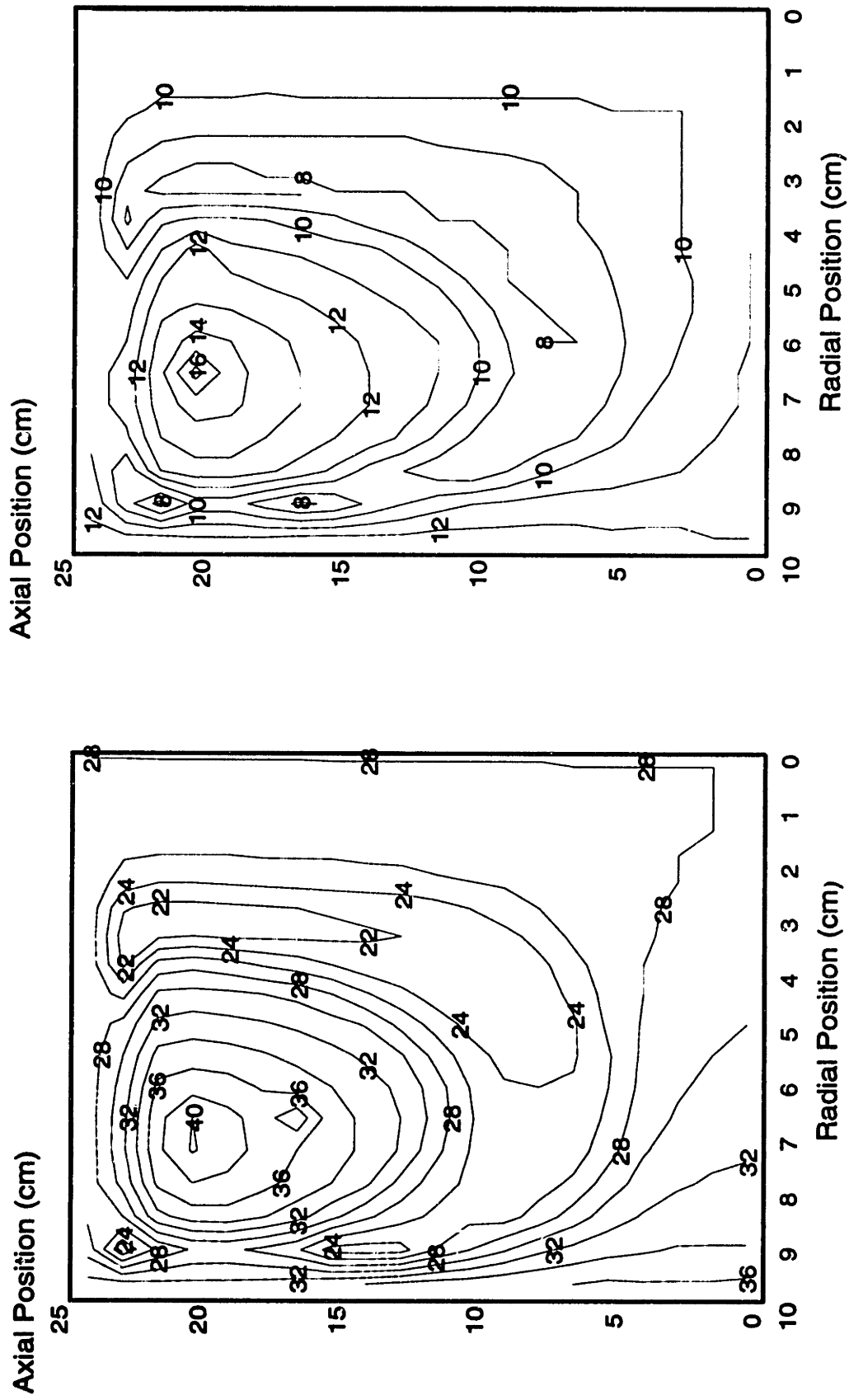
Figure 3-15: The effect of tracer addition locations on mixing time plotted as contours under two different gas volume flow rates. (a) $Q = 41.4\,Ncm^3/s$ and (b) $Q = 331.2\,Ncm^3/s$

simulation results shows that:

$$t_m \propto Q^{-0.5} \qquad (3.2)$$

Aspect Ratio   To investigate the aspect ratio effect on overall mixing time, series of tests were carried out in which the aspect ratios were chosen to be in the range of 0.5-2.0. The three injection points, identical to those used in the gas volume flow rate analysis, were selected to calculate the mixing time of the system, by averaging three mixing times obtained from three injections. Considering that the reactor volume was not kept constant for the different aspect ratios, the mixing time was normalized by the volume of the system. Figure 3-17 shows the results of these calculations. One can see from the figure that the normalized mixing time decreases as the aspect ratio increases. This is probably due to a longer residence time of the bubbles, in the range considered in this work.

Nozzle Size   Different nozzle sizes ranging from 1 mm to 6 mm were tested to investigate the possible effect of the nozzle dimensions on the overall mixing time of the system. The results are shown in Figure 3-18, from which one can see the effect of nozzle size is difficult to define. It seems that nozzle size has no effect at all on the system mixing time when it is increased from 1 mm to 4 mm, and the mixing time seems increasing when the nozzle size is increased further. It does make some sense because as the nozzle size gets bigger, the decreasing of the kinetic energy, which is only a small fraction of the total stirring energy, becomes visible only after some threshold size. Nevertheless, since the limiting value obtained in these calculations are only 3 s in difference, the effect of the nozzle size can be assumed negligible for the range of sizes explored.
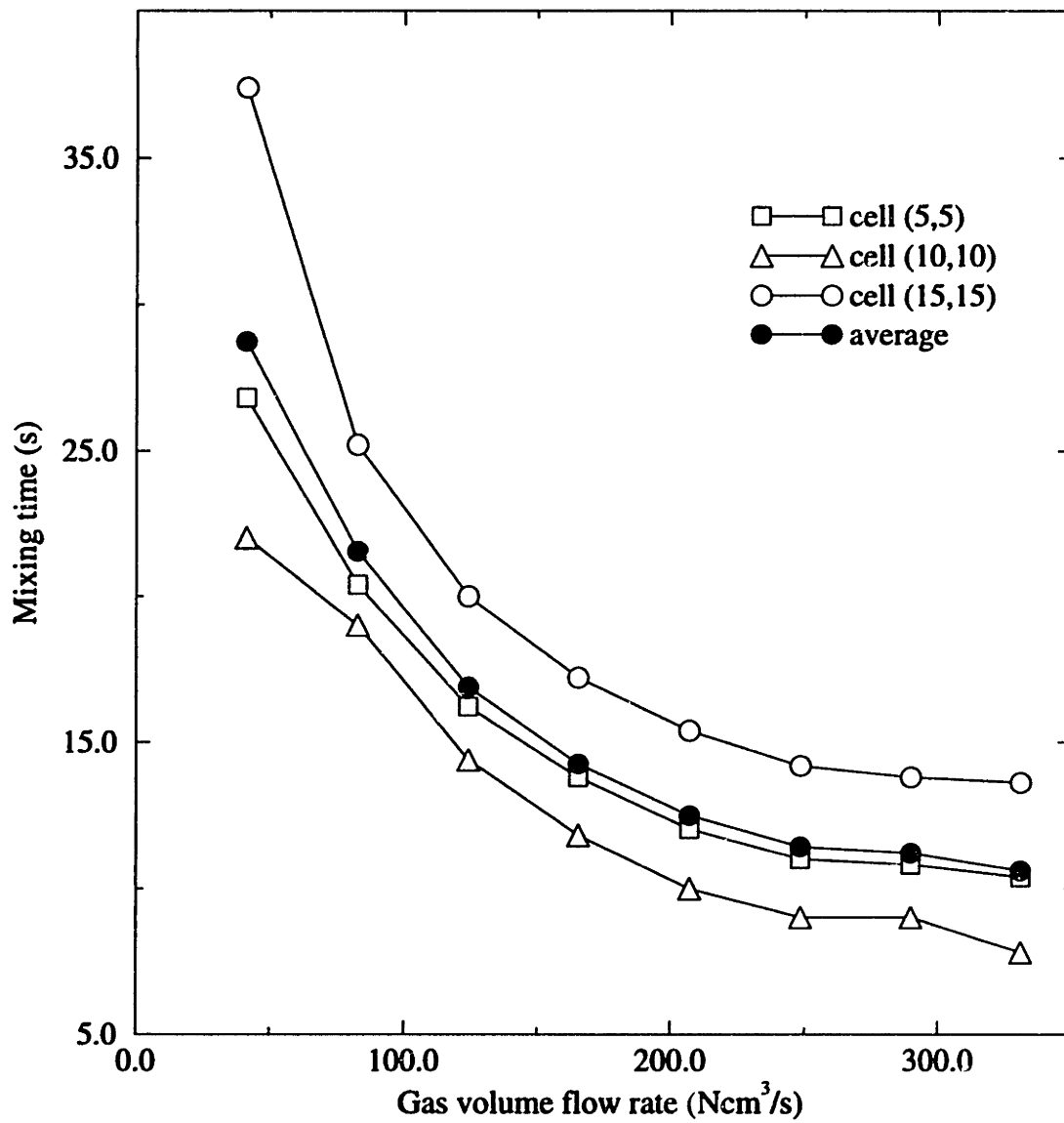
Figure 3-16: The effect of gas volume flow rate on mixing time.
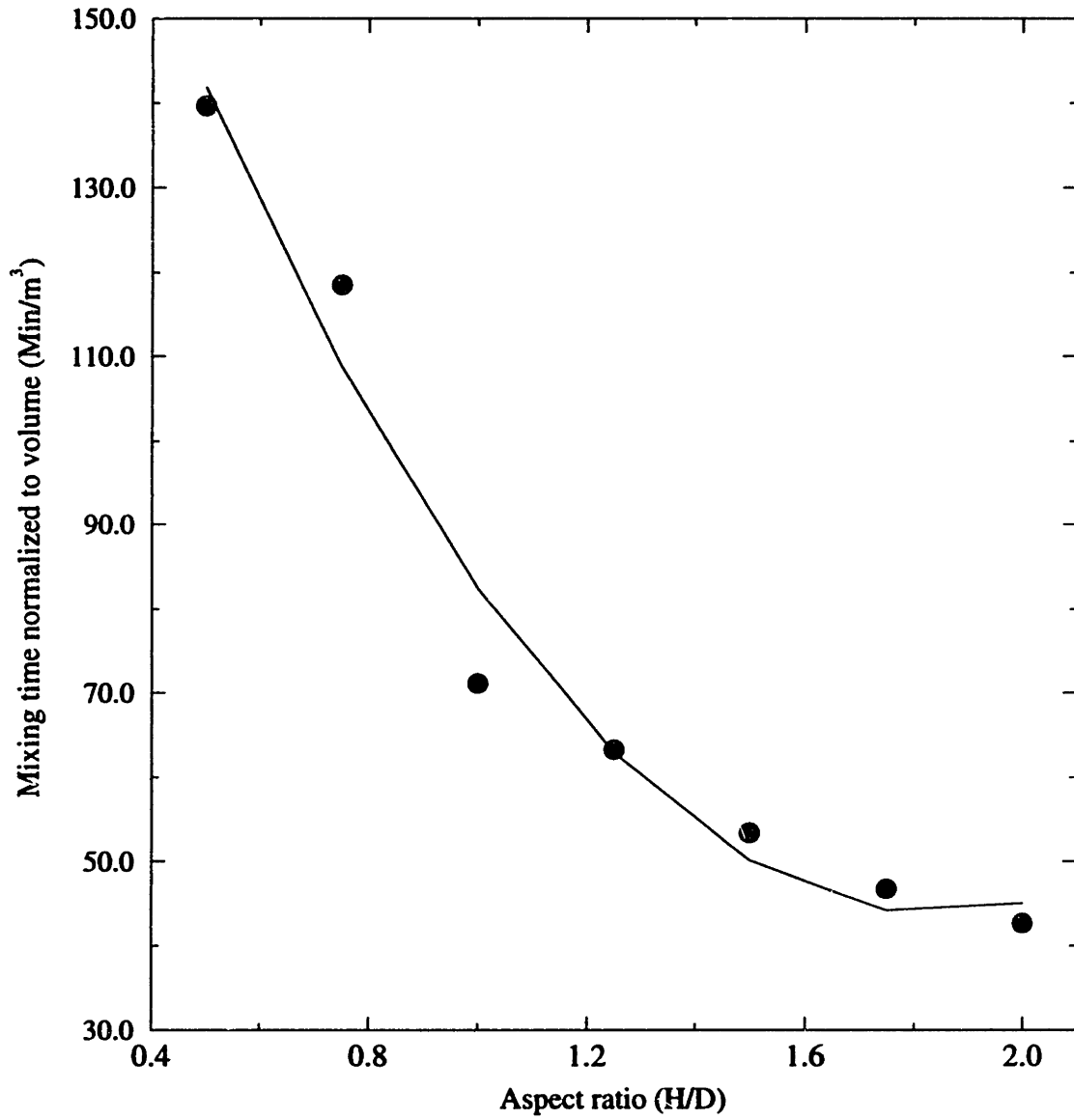
Figure 3-17: The effect of the reactor aspect ratio (H/D) on mixing time.
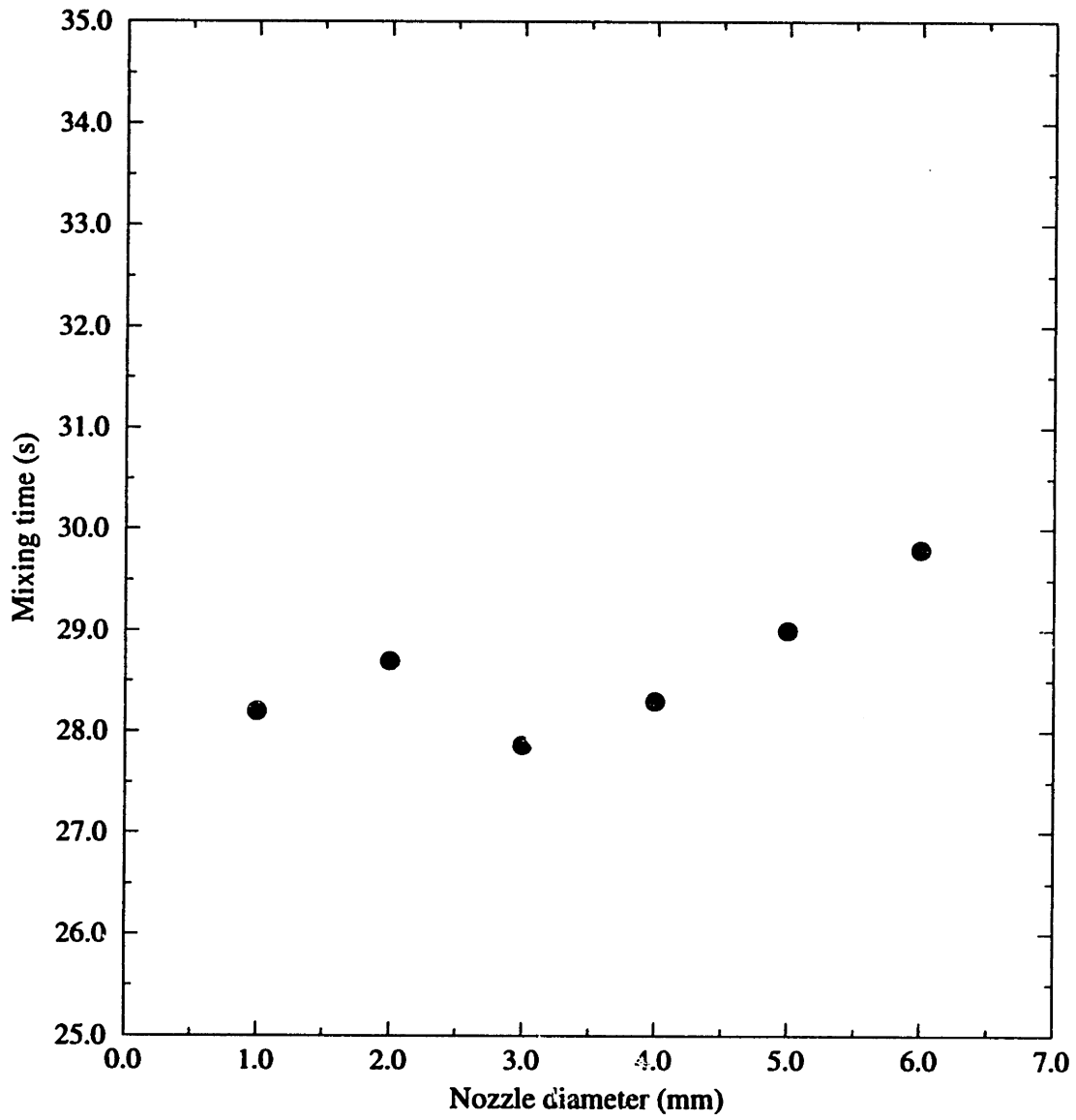
Figure 3-18: The effect of nozzle diameter on mixing time.

3.2 Single Eccentric Bottom Gas Injection

A study of a cylindrical reactor with eccentric bottom gas injection is presented in this section since this kind of design is also widely used in steel refining processes. It is desirable to compare the behavior of a system being stirred with eccentric gas injections to the behavior of a system with central stirring. It is also important to understand the advantages and disadvantages of these kind of systems. Figure 3-19 shows a schematic sketch of an eccentric bottom gas stirred cylindrical reactor.

Several investigations [56-59] have shown that eccentric bottom injection is superior than central injection in terms of improving mixing times. In contrast, mass transfer studies have shown that the mass transfer coefficient at the melt-slag interface is the highest under central injection [47]. In the rest of this chapter, the analysis will be focused on fluid flow and mixing for a system with eccentric bottom gas injection. It is noted, however, that mixing operations in ladles are more common than refining operations. Thus, it is in general that more critical to consider optimal mixing times than enhanced mass transfer coefficient in this case.

3.2.1 Fluid Flow and Mixing

The size of the system chosen to investigate the fluid flow behavior of an eccentric gas injection was the same as the one with central bottom injection presented in previous sections for suitable comparison. The computational procedures were similar, as described in the previous sections, except that there was not a symmetry axis along the centerline of the system in this case. Therefore, the simulations conducted for this kind of systems were fully three dimensional; however, because of the radial symmetry plane available, only half of the system was needed as the computational domain. Figure 3-20 shows top and symmetry plane views of the computational domain and the grid was used in these calculations which involved a $25 \times 21 \times 20$ nonuniform cells. A typical calculation used about 6500 sweeps for the mesh mentioned above and required approximately 10 hours CPU time on a SUN Sparc 20 workstation.

A number of cases were run to investigate the fluid flow and mixing behavior of a

70
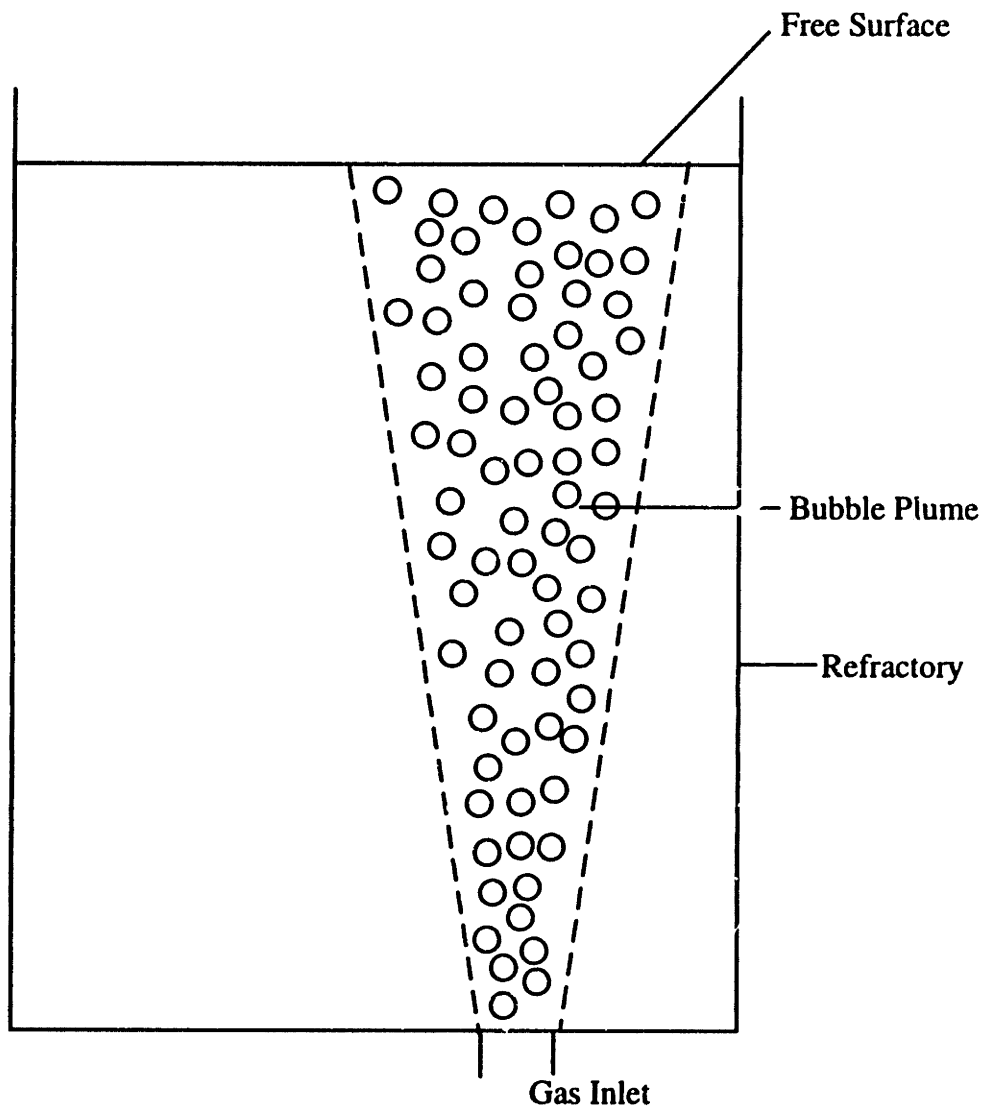
Figure 3-19: A schematic representation of a cylindrical reactor with eccentric gas injection at the bottom.
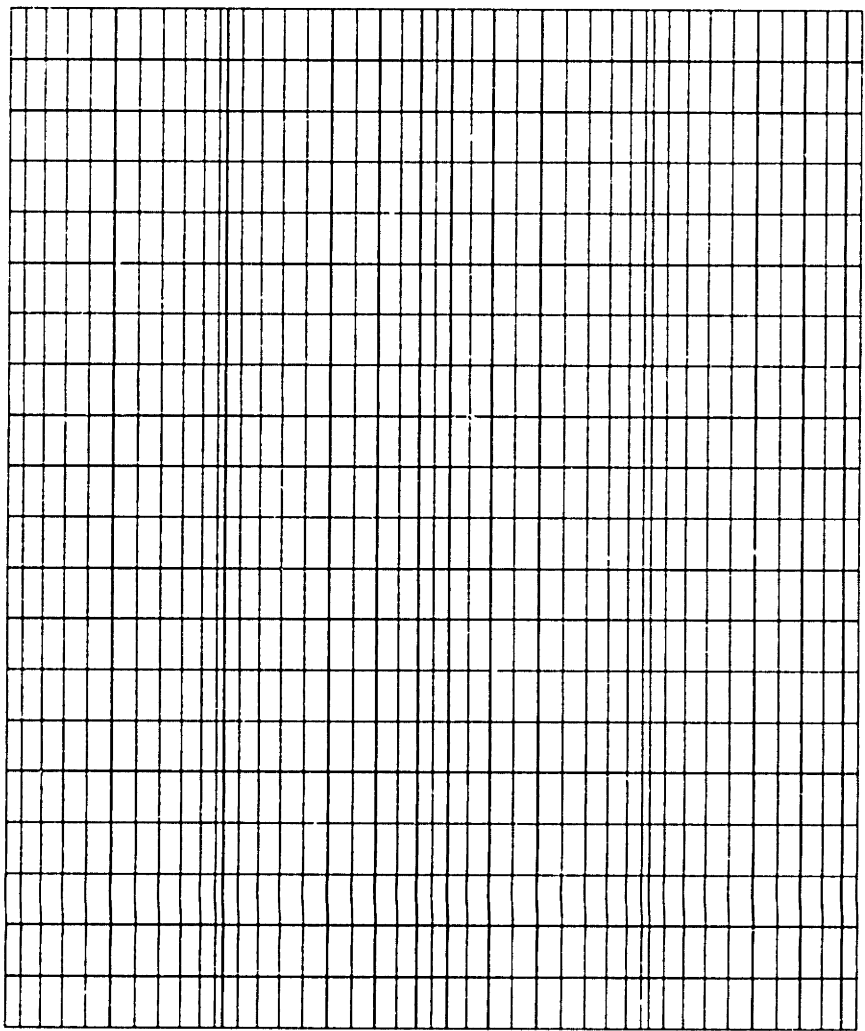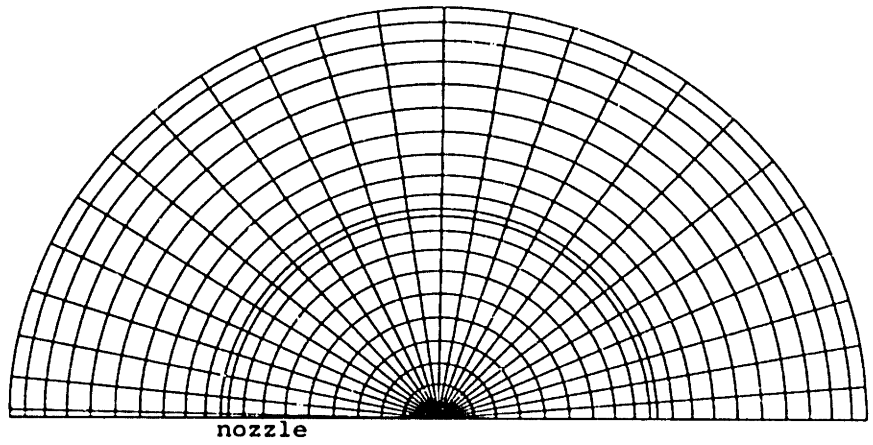
nozzle

Figure 3-20: Top and lateral views of the grid used for an eccentric gas stirred system where the nozzle was located at the half radius.

system with a eccentric bottom gas injection, where the eccentric nozzle was placed at different locations. The results are shown and analyzed as follows:

Figure 3-21 shows velocity fields on different planes for two different nozzle locations, which are 0.35R and 0.65R, respectively. The flow patterns shown in the figure indicate that the gas plumes are inclined to the closest wall when an eccentric gas injection is applied to a cylindrical system. This phenomena has been supported by related physical modeling work, but not been able to be predicted by other investigators using the quasi-one phase method, where a symmetric prescribed gas volume fraction distribution was assumed [57, 58].

3.2.2 Optimization of Locating the Nozzle

Mixing time analysis was also carried out to study the effect of the placement of the eccentric nozzle. In order to find an optimal nozzle location for a cylindrical reactor with an eccentric bottom gas injection, a comprehensive investigation was carried out by comparing the calculated system mixing times for different nozzle locations. As mentioned earlier, the effect of tracer measurement was eliminated from the simulation. Therefore, the only thing left which would affect the value of mixing time was the tracer addition locations.

In this study, nine different tracer addition points were selected for each nozzle configuration and computed mixing times were averaged to eliminated the effect from the different tracer addition locations. The results are shown in Figure 3-22 as averaged mixing time vs. nozzle location. The results indicate that mixing time required for complete mixing in an eccentric injected reactor are lower than in systems with a central injection. Among those nozzle locations, two positions offer the lower mixing times, which are at $\frac{1}{5}R$ and $\frac{2}{3}R$, respectively. The former location provides a slightly lower value of mixing time. It can be estimated that with an optimal nozzle location, an eccentric system should be able to improve the mixing time by about 43% relative to a central (symmetric) system.
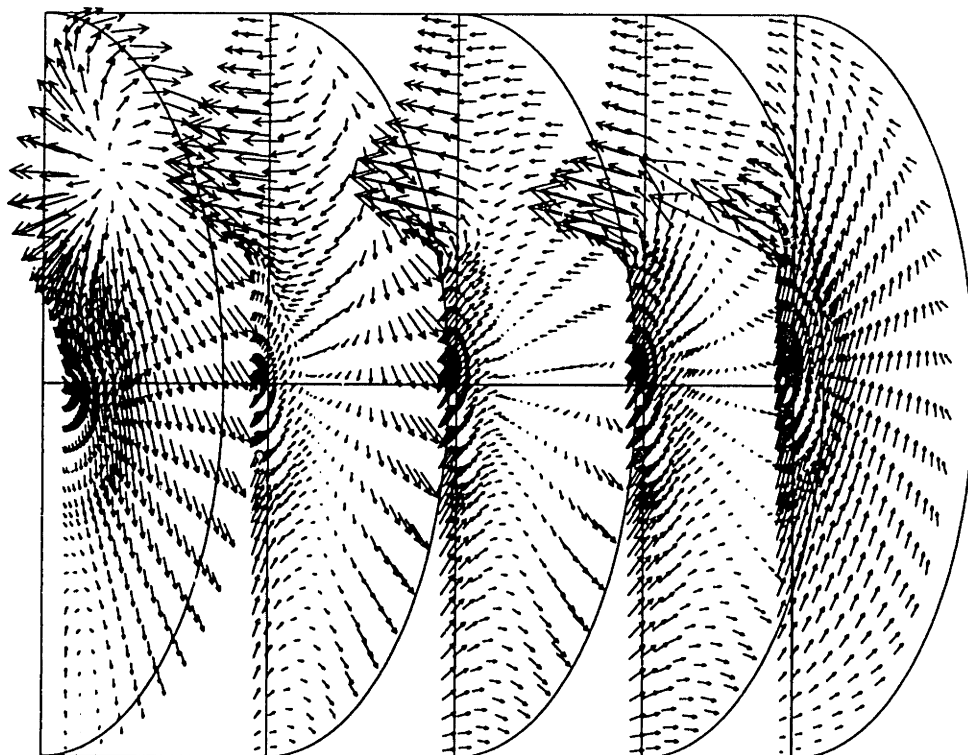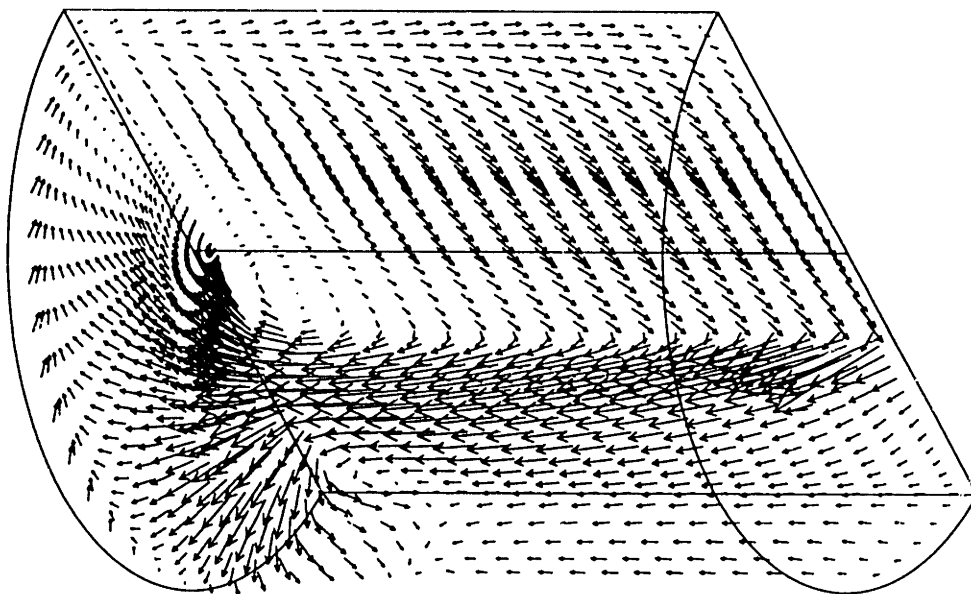
$\longrightarrow$ 0.40 m/s

$\longrightarrow$ 0.40 m/s

Figure 3-21: A three dimensional view of predicted liquid velocity field for a cylindrical system with eccentric bottom injection (a) 0.35R.

$\longrightarrow$ 0.40 m/s

$\longrightarrow$ 0.40 m/s
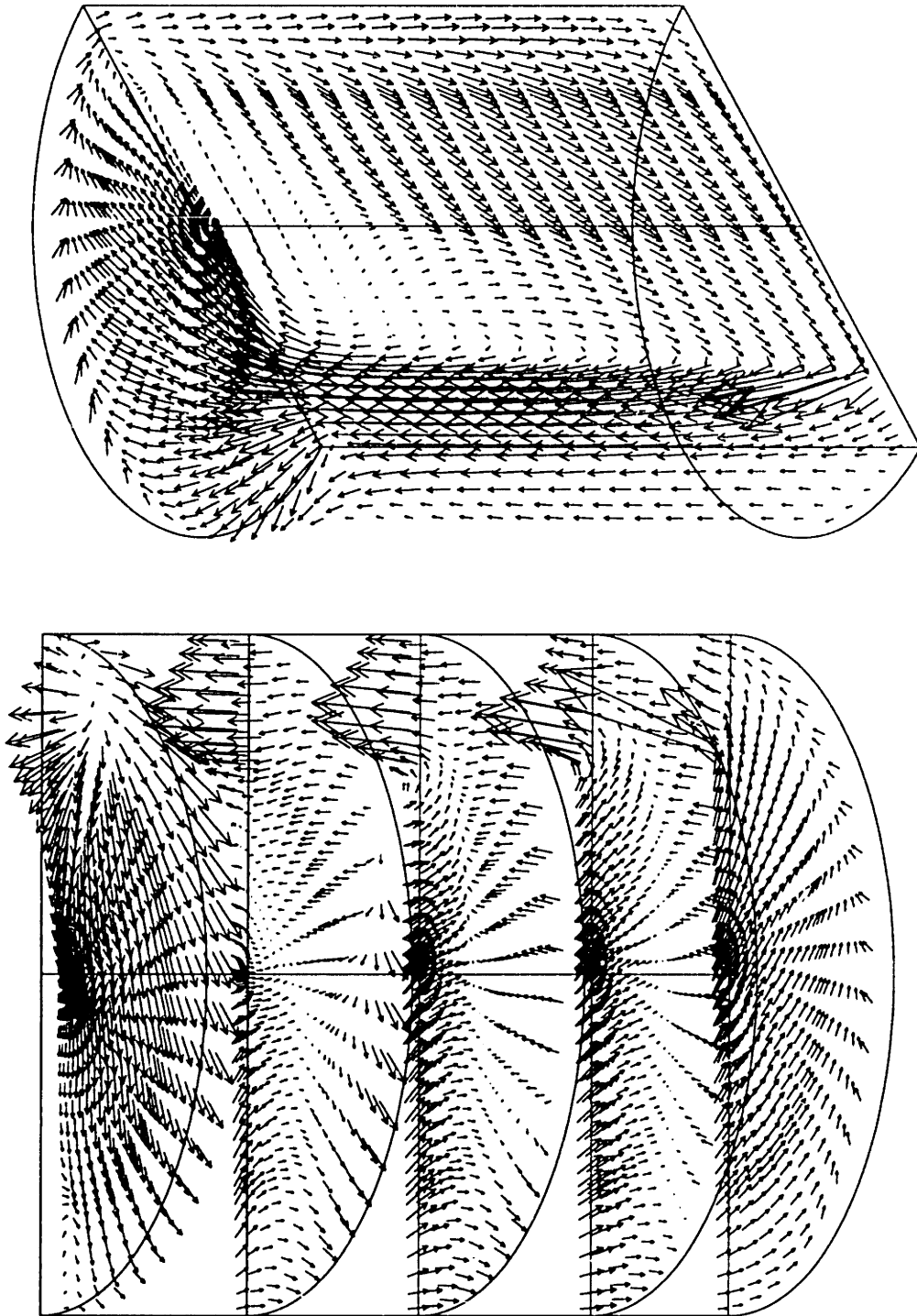
Figure 3-21: (continued) A three dimensional view of predicted liquid velocity field for a cylindrical system with eccentric bottom injection (b) 0.65R.

75
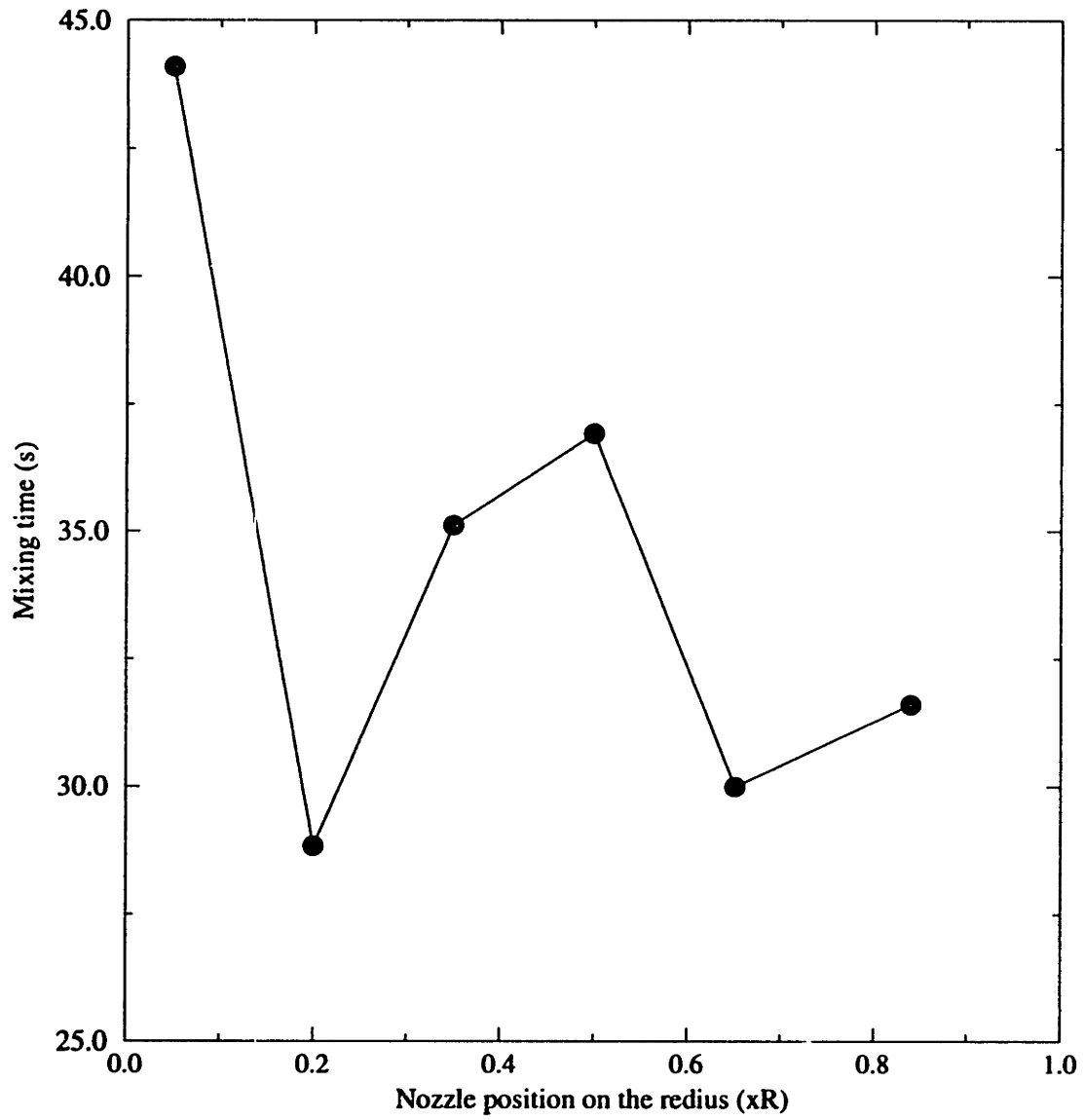
Figure 3-22: Computed mixing time as a function of nozzle location for a cylindrical system with eccentric bottom injection.

3.3 Summary

With the aide of computer simulation by using a two-phase model, a cylindrical metallurgical reactor with either central or eccentric bottom gas injection was investigated. Comparison of model predictions with two sets of experimental measurements shows that good agreement is generally reached.

The influence of operating and design parameters was also analyzed using a mixing time concept. A mixing time map, which is considered the first one in this kind of studies, shows exactly where the optimal location is for introduction of tracer addition (or other ingredients such as alloying additions). The results also suggest that there is a narrow band just outside the plume region where added tracer takes the minimum time to reach the whole system. On the other hand, by adding tracer at the recirculation "eye", the system takes the longest time to reach complete mixing.

The effect of operating parameters can be summarized as follows: Decrease of mixing time can be achieved by increasing the gas volume flow rates injected into the system, by introducing higher level of energy. The mixing efficiency can also be improved by increasing the system aspect ratio. This can be explained as the gas bubbles spend longer time in the system when the system has higher aspect ratio, and the total energy from the buoyancy is increased. The diameter of the nozzle seems not to have a significant effect on reactor mixing time.

It was found that a system with eccentric gas injection promotes better mixing than the one with central injection in terms of less mixing time, probably because an additional horizontal circulation is introduced into the system by using eccentric gas injection. The horizontal circulation certainly improves mixing by convection. The optimal position to locate the gas injector was found at $\frac{1}{5}R$.

Chapter 4

Channel-Type Reactors

4.1 Introduction

This chapter focuses on the analysis of the fluid flow and mixing characteristics in a channel-type reactor with bottom gas injections. The isothermal fluid flow behavior is presented in this chapter while the mass transfer analysis is deferred to the following chapter.

It is noted that the analysis presented here is specifically related to the physical model developed at the University of Missouri-Rolla (UMR). The main purpose of the mathematical modeling work was to support the experimental work by gaining some understanding of the main fluid flow characteristics for this type of system and hence to assess the feasibility of the counter-current reactor, and provide suggestions for better designs and experimental campaigns.

As recently suggested by Nelson and Robertson [8], channel-type reactors can be considered as an economic alternative for refinement operations in metallurgical systems due to a number of advantages, including:

1. Potential for the maintenance of significant driving forces for reaction along the whole length of the reactor.

2. Lower energy consumption and possibly improved yield.

3. Reduction in the volume of slag required for refining, which reduces the con-

sumption of expensive fluxes.

It is understood that channel-type reactors are very different from cylindrical ones in that fluid is continuously entering and exiting the system for the continuous ones. This means that the residence time of the fluid in the system is limited, while refining operations require sufficient time for completion. It is to believe that in order to have efficient refining operations and high quality products, it is best to keep high concentration gradient in the longitudinal direction, while having perfect mixing in the cross section direction. Several additional requirements have to be kept in mind when a successful channel-type reactor is considered. For instance, the length of the reactor is limited by space and economic restrictions. Toward this, it is required that the reaction rates between gas and liquid or liquid and liquid be high enough for all the necessary refining processes to complete before the fluid leaves the system. In the mean time, the production rate is also a concern, since one can always stick to the existing batch operations. And finally, as environmental regulations become more strict, the amount of slag used in the channel-type reactor has to be limited too.

A schematic representation of the experimental setup at UMR is shown in Figure 4-1. The figure shows the main components involved in the physical model, in particular, the counter-current flow of the two immiscible liquids (water and TCE) is indicated in the figure.

Taking the physical model as a reference, the mathematical modeling effort was carried out on a simpler representation of the system. The reason for this was twofold: first, because of the additional complexity in dealing with a three phase system mathematically; and second, most of the experimental runs carried out at UMR were on a two-phase system. A schematic representation of the model system is shown in Figure 4-2, where it is seen that the liquid is entering from one end and leaving at the other end of the reactor. In the mean time, the liquid is agitated by ascending gas streams injected from the bottom. Obviously the fluid flow in the system is highly turbulent and having other complications as well. Although the third phase is not considered directly in the calculations, some assumptions are made to incorporate some of the effects of the third phase by means of the boundary conditions at the top surface.
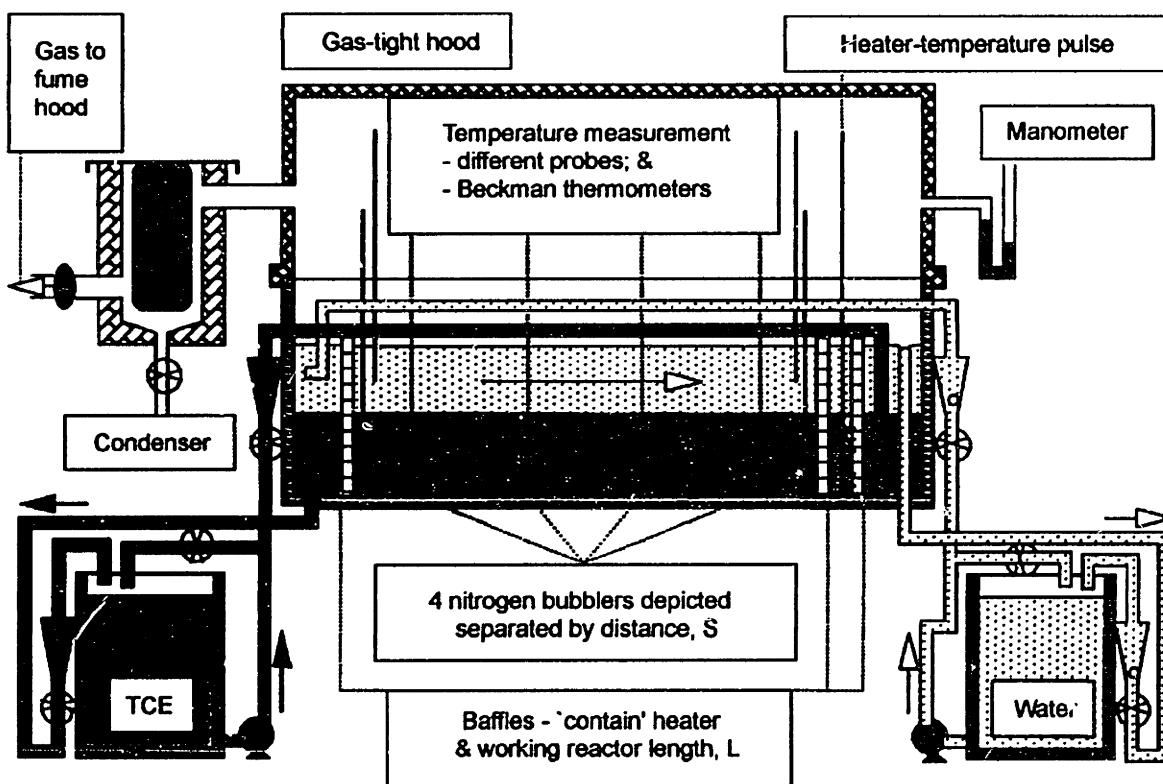
Figure 4-1: A schematic representation of the experimental setup at UMR.

Table 4.1: Standard operating parameters for the channel-type reactor.

Nozzle diameter	1 mm
Bubbler number	2, 4, 6, 8
Gas flow rate	4.52 l/min
Horizontal liquid velocity	0.35 cm/s

This point will be discussed later in this thesis.

The size of the system, which is identical to the physical model setup at UMR, is also shown in Figure 4-2. The model consists of a two phase system composed of water and nitrogen, the same system used in some of the physical modeling tests. The standard operating conditions are shown in Table 4.1.

4.2   Fluid Flow and Mixing

The simulation procedure carried out for a channel-type reactor was similar to the one used for the cylindrical system presented in the previous chapter. After obtaining the steady state solutions for the Navier-Stokes equations, a tracer dispersion equation was solved to obtain the dispersion number (the inverse Peclet number D_e/uL) which helps assess the deviation of the system from a plug flow behavior.

Since the system analyzed in this chapter has a rectangular shape, Cartesian coordinates, instead of cylindrical polar coordinates, were used. The x axis was used to represent the liquid phase flow direction which coincides with the longitudinal direction of the reactor. The z axis was used to represent the upward direction which is also the gas injection direction. Knowing that nozzles are distributed evenly at the center line of the reactor bottom, only half of the actual system is needed to be taken as the computational domain. This of course saved a great deal of computational time.

The actual CPU time required depends on the grid number that was chosen. For a system with four nozzles, a nonuniform grid of 52×20×20 was used in the simulation. A typical calculation used around 6000 sweeps to reach convergence for this mesh and required about 2~3 days of CPU time on a SUN Sparc 20 workstation.

81
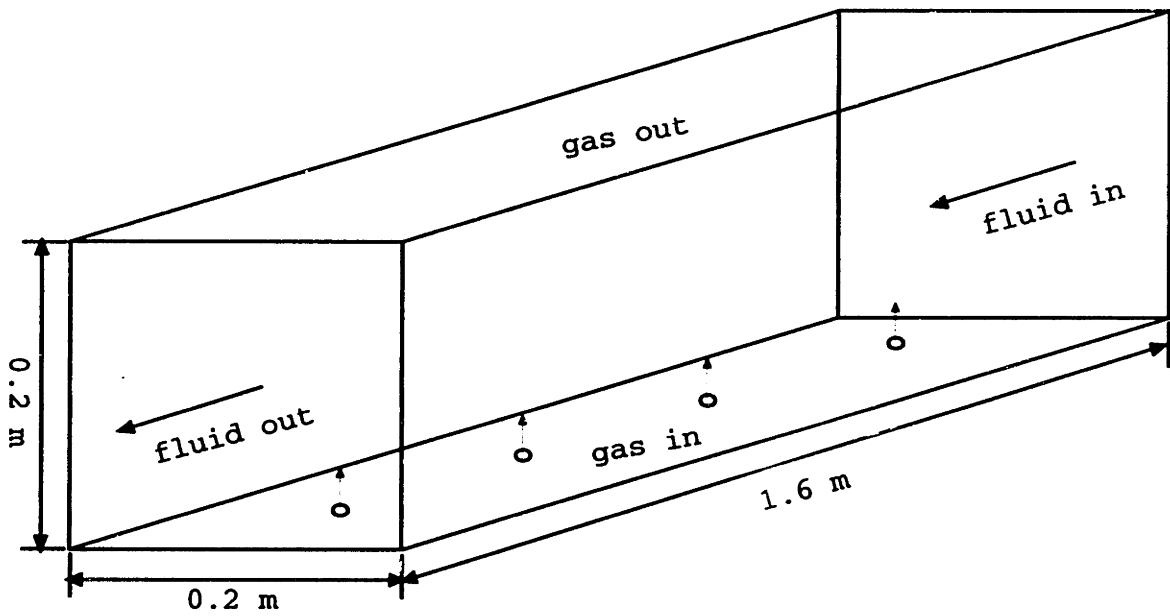
Figure 4-2: A simplified model of a channel-type reactor with bottom gas injections (not in scale).

4.2.1 Dispersion Analysis

The way to investigate the mixing behavior of the channel-type reactors was slightly different from the way used to analyze the cylindrical reactors. For a channel-type reactor, a pulse tracer (2.5 s in most of the cases) was introduced at the inlet along with the working fluid (water in this case), and the tracer concentration leaving the exit of the reactor was recorded at the outlet. By plotting the normalized concentration and normalized time, the conventional so called C-curves were obtained. The actual residence time and inverse Peclet number were obtained by integrating the C-curves as described in Chapter 2.

4.2.2 Particle Tracking

Particle tracking analysis is very helpful to understand the fluid flow patterns because of the complicate nature of fluid flow in this type of system (three dimensional and multiple bubblings). To do this, an additional equation describing the trajectory of each particle has to be solved as explained in Chapter 2 (equation 2.34).

"Lazy particles", which have the same velocities as the working fluid, were introduced from the inlet of the reactor to investigate the overall flow patterns and the residence time distribution of the fluid within the system. The number of particles used in this calculation was equal to the number of simulation cells representing the cross section of the reactor, which was 18 × 18 (324) in this study. The time each particle spent in the system was recorded and the average, as well as the standard deviation, was calculated. The results are to be shown and analyzed in the next subsection.

4.2.3 General Fluid Flow Characteristics

Some general characteristics of the fluid flow within the channel-type reactor can be obtained by solving the Navier-Stokes equations and using particle tracking techniques. Figure 4-3 is a plot showing two different three-dimensional views of the computed velocity field for an 8-nozzle system. Because the horizontal fluid flow

velocity is quite small in comparison to the vectors shown, the mean flow stream from inlet to outlet is not apparent. It is seen that the flow pattern in the reactor is mainly affected by the gas injections, which produces recirculatory flows both in the longitudinal and transverse directions.

Figure 4-4 shows the fluid flow patterns at the cross sections where nozzles are located. The figure shows that the flow patterns within the main recirculation loops change from nozzle to nozzle.

Figure 4-5 shows the trajectories of two representing lazy particles. The trajectories of the particles show that the fluids are moving spirally along the reactor, and if a plume is encountered by the fluids, the fluids will be trapped for longer time than otherwise. Therefore, it is appropriate to think the reactor is composed of a string of mini-mixers which are centered at locations where the nozzles are located. It is also feasible to see the plane where a plume acts as a barrier to the liquid flowing horizontally.

The results from the dispersion analysis were compared with the corresponding experimental measurements obtained at UMR. The comparison is shown in Figure 4-6 where a 4-nozzle system is considered. Computed longitudinal diffusivities are shown as a function of the horizontal fluid flow velocity. It can be seen that the predicted longitudinal diffusivities are within the same order of magnitude as the experimental values, which is promising since the measurements have been said to be only qualitatively correct, because of the drawbacks involved in the thermal tracer technique that was employed. It was also mentioned in the review by Mazumdar and Guthrie [3] that one order of magnitude difference between turbulence parameters values, from which the diffusivities are obtained, only results in an 11% difference in velocity values. Therefore, it can be suggested that the disparity in velocity would be within 10% if the flow velocities were measured instead.
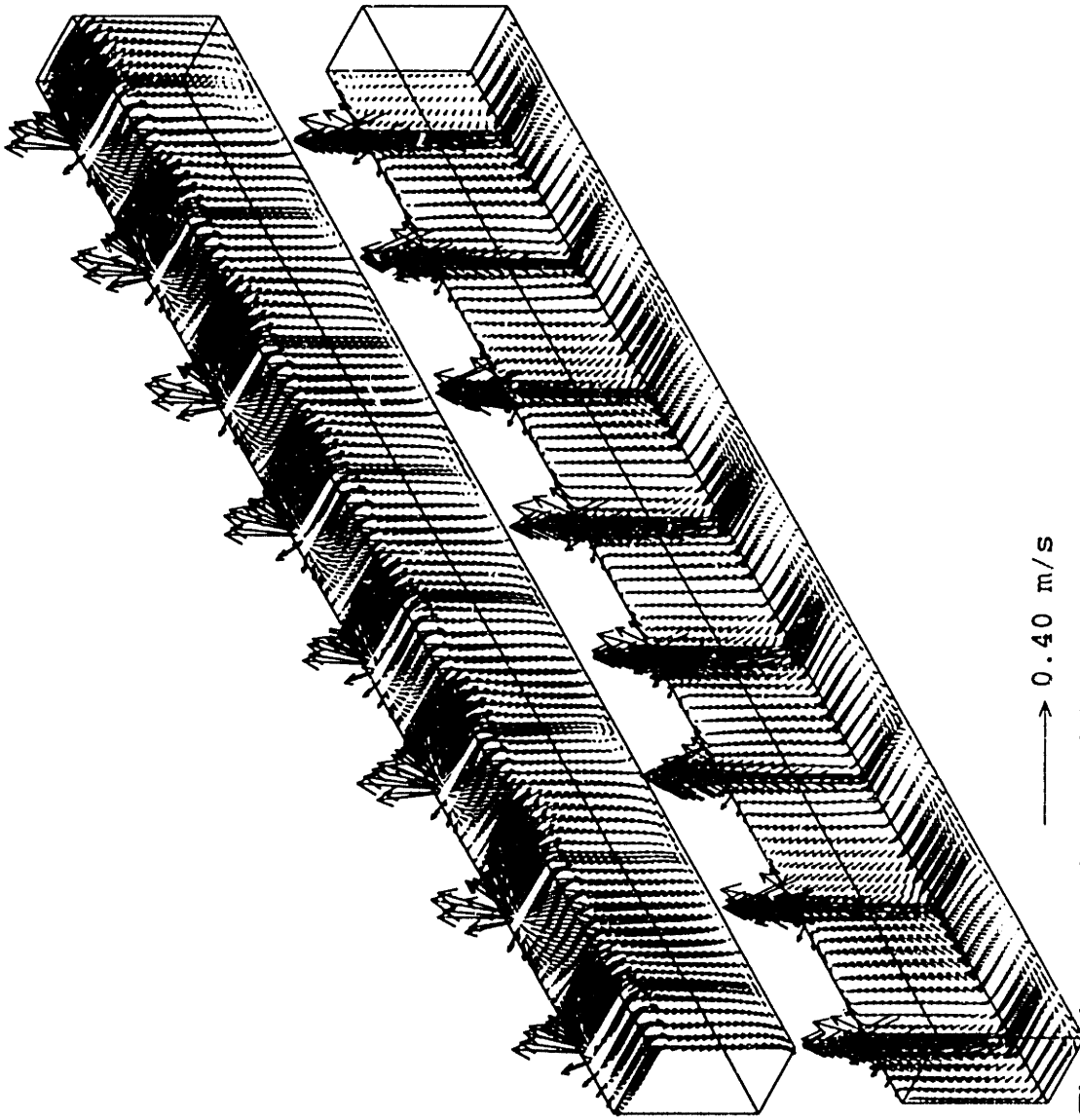
Figure 4-3: Three-dimensional views of the computed average velocity field for an 8-nozzle system ($Q = 9.04$ l/min, the fluid flows from right to left).
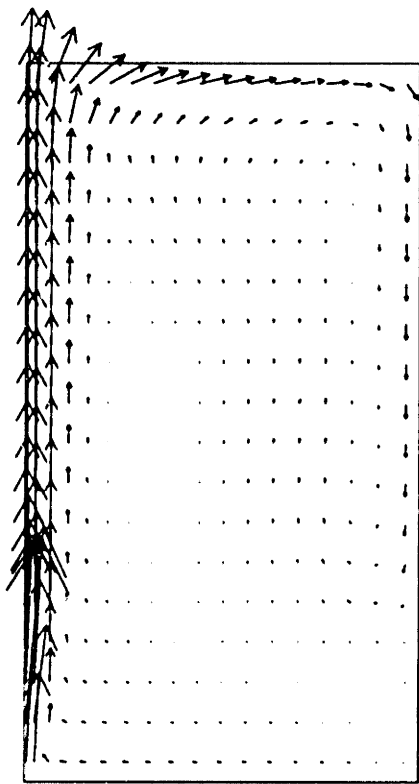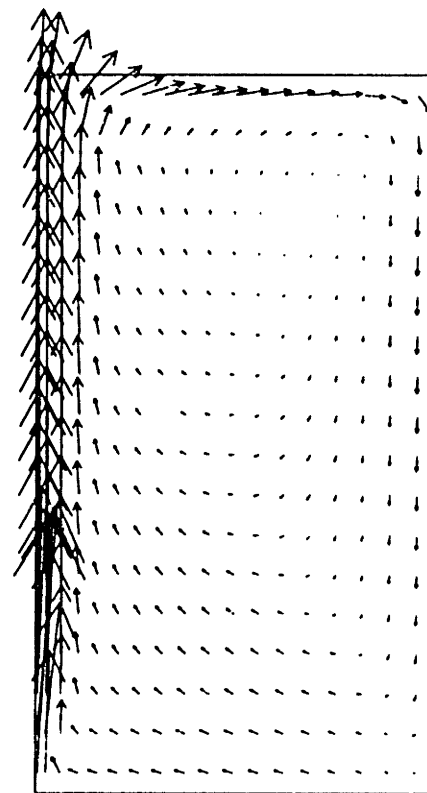
(a) nozzle 1   (b) nozzle 2
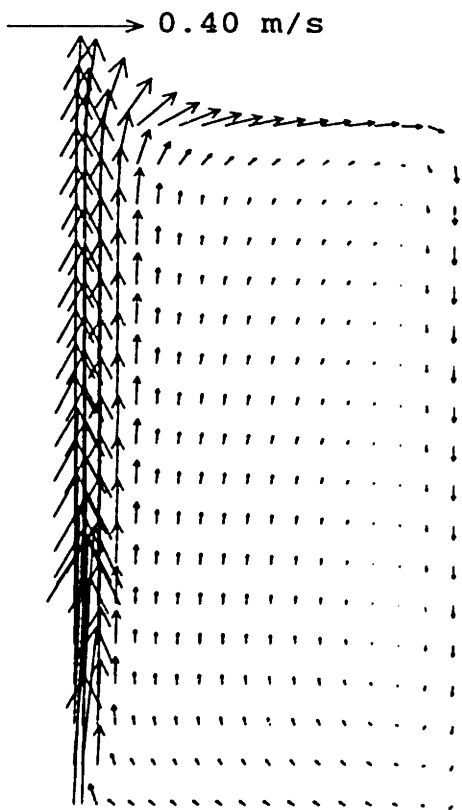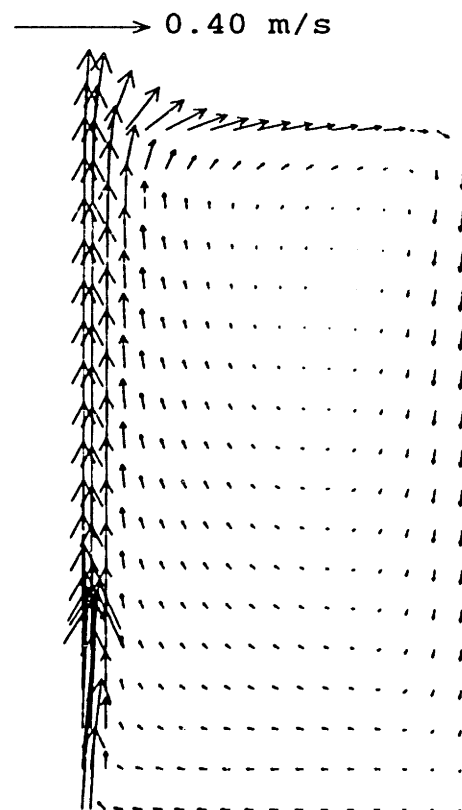
(c) nozzle 3   (d) nozzle 4

Figure 4-4: Fluid flow patterns at the nozzle planes perpendicular to the longitudinal direction of the reactor (8-nozzle, $Q = 9.04\,l/min$).
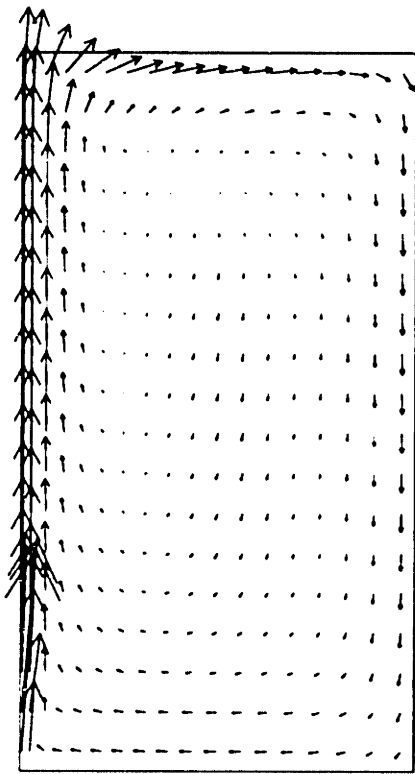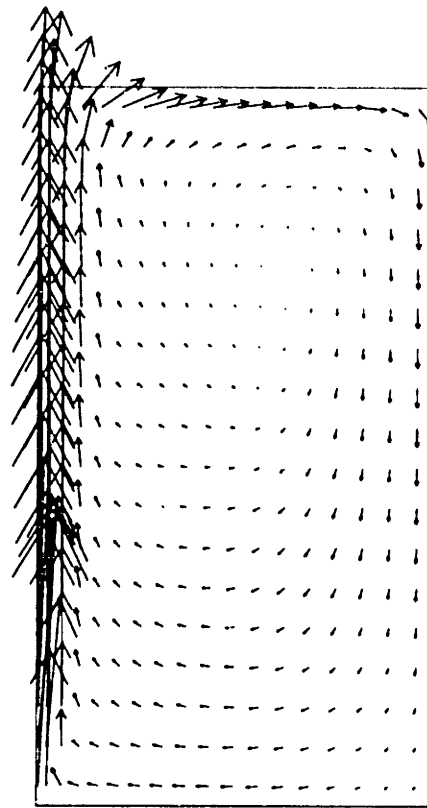
(e) nozzle 5

(f) nozzle 6
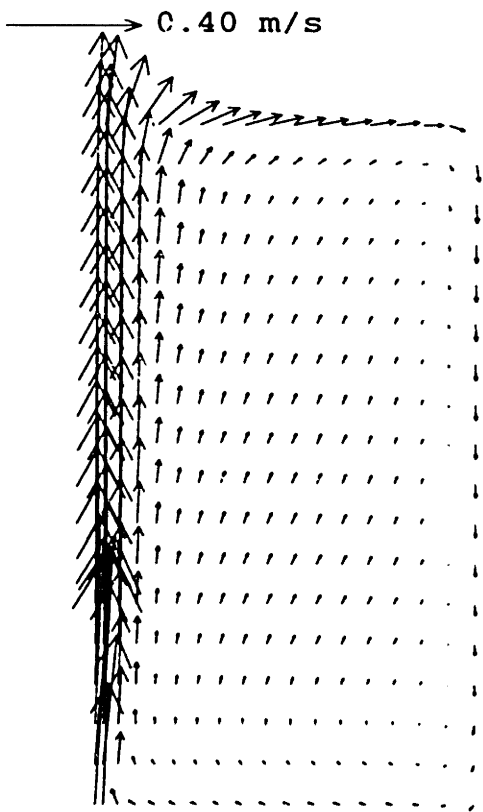
(g) nozzle 7
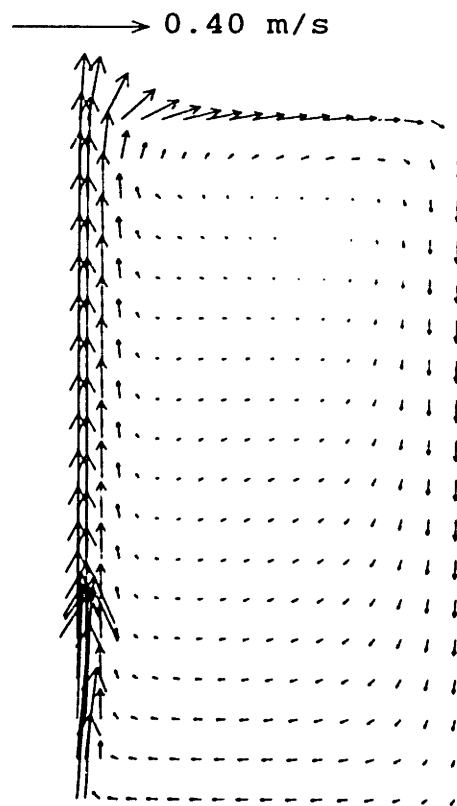
(h) nozzle 8

Figure 4-4: (continued) Fluid flow patterns at the nozzle planes perpendicular to the longitudinal direction of the reactor (8-nozzle, Q == 9.04 l/min).
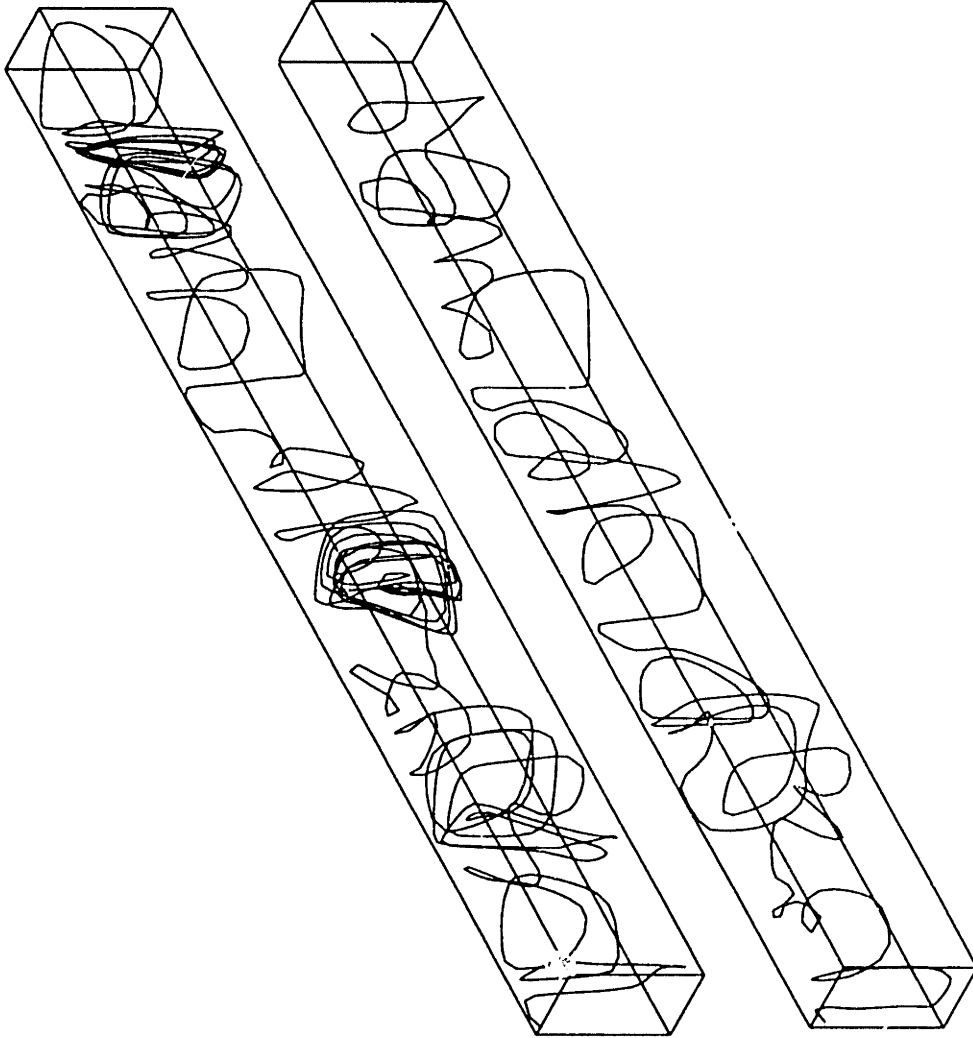
Figure 4-5: Two sample trajectories of "lazy" particles in an 8-nozzle system (particles enter the system from the right hand side, $Q = 9.041/\text{min}$).
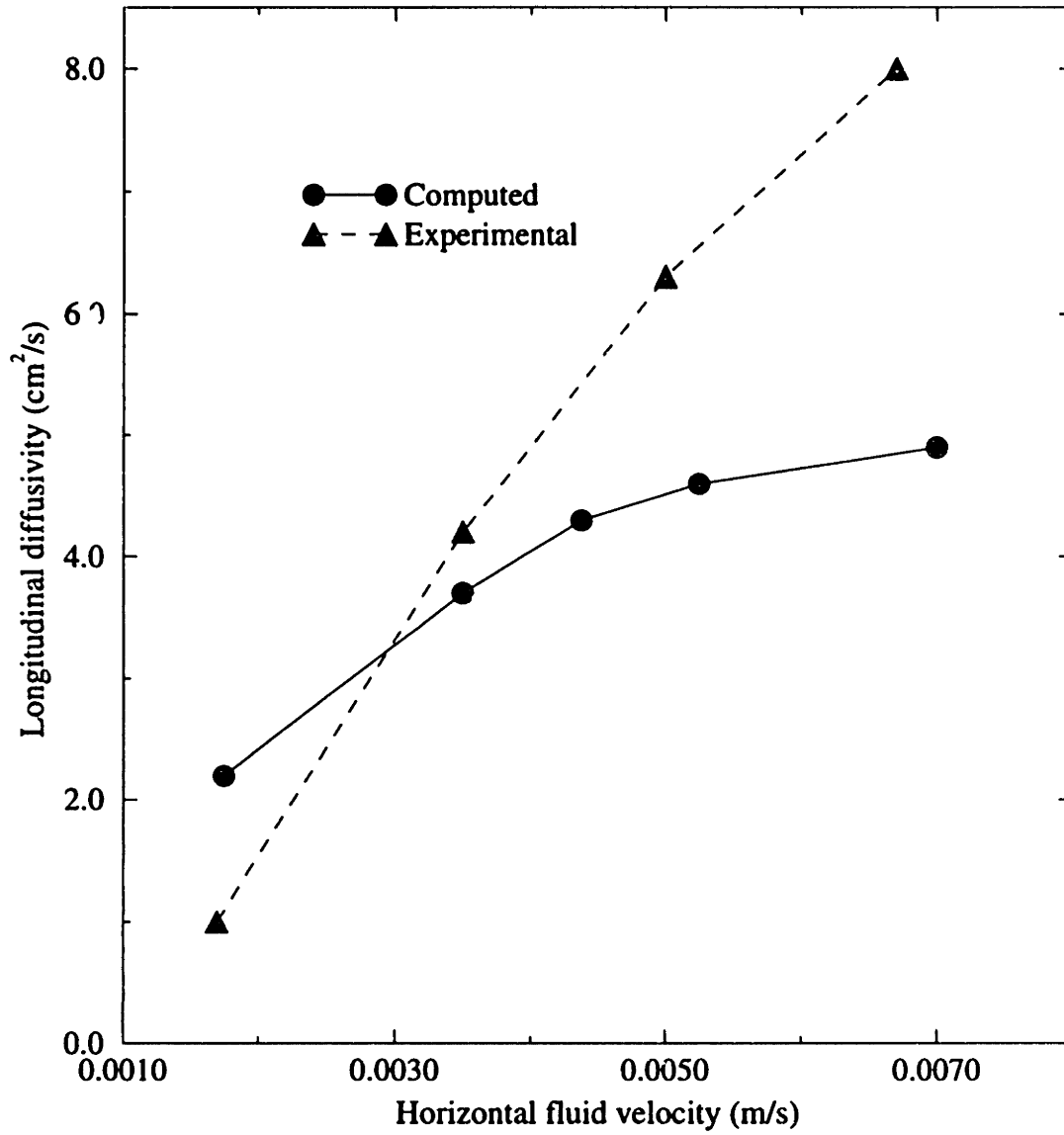
Figure 4-6: Calculated longitudinal diffusivities for a 4-nozzle system and the comparison with experimental measurements obtained at UMR.

4.3 Parametric Analysis of Operating Conditions

Figures 4-7 through 4-14 show the effect of individual operating parameters (such as the gas volume flow rate, reactor aspect ratio H/W, horizontal liquid flow rate and bubbler separation) on the vessel dispersion number, while keeping other parameters unchanged.

4.3.1 Gas Volume Flow Rate

Figure 4-7 shows a series of C-curves calculated for different gas flow rates from which the actual residence times and dispersion numbers were estimated. As indicated in the plot, the peak value of the C-curves decreases and the curve moves further left when the total gas volume flow rate is increased. This behavior indicates some departure from plug flow conditions (i.e., $t/t_{mean} = 1$) as the gas flow rate increases.

Figure 4-8 shows the effect of gas flow rate on the values of the inverse Peclet number for a 4-nozzle and an 8-nozzle system. It is seen that the inverse Peclet number in general increases as the gas flow rate increases. This is due to the fact that an increase in the gas flow rate leads to an increase in the energy injected into the reactor. A higher energy input causes more turbulence and recirculation which results in greater deviation from plug flow behavior. Results from residence time analysis shown in Figure 4-9 also supports this conclusion.

An interesting feature is also noted from Figure 4-8 where as the gas flow rate increases to some critical point, the value of the inverse Peclet number D_e/uL suddenly decreases. The possible reasons for this feature are:

1. As the gas flow rate reaches some critical value, the fluid flow pattern changes (e.g. gas plumes start interacting with each other), hence the dependency of dispersion number on the gas flow rate.

2. As the gas flow rate increases, the gas volume fraction in the system also increases. Since the interaction between the two phases are based on drag force, the formulations may not be representing any more after some critical gas flow

90
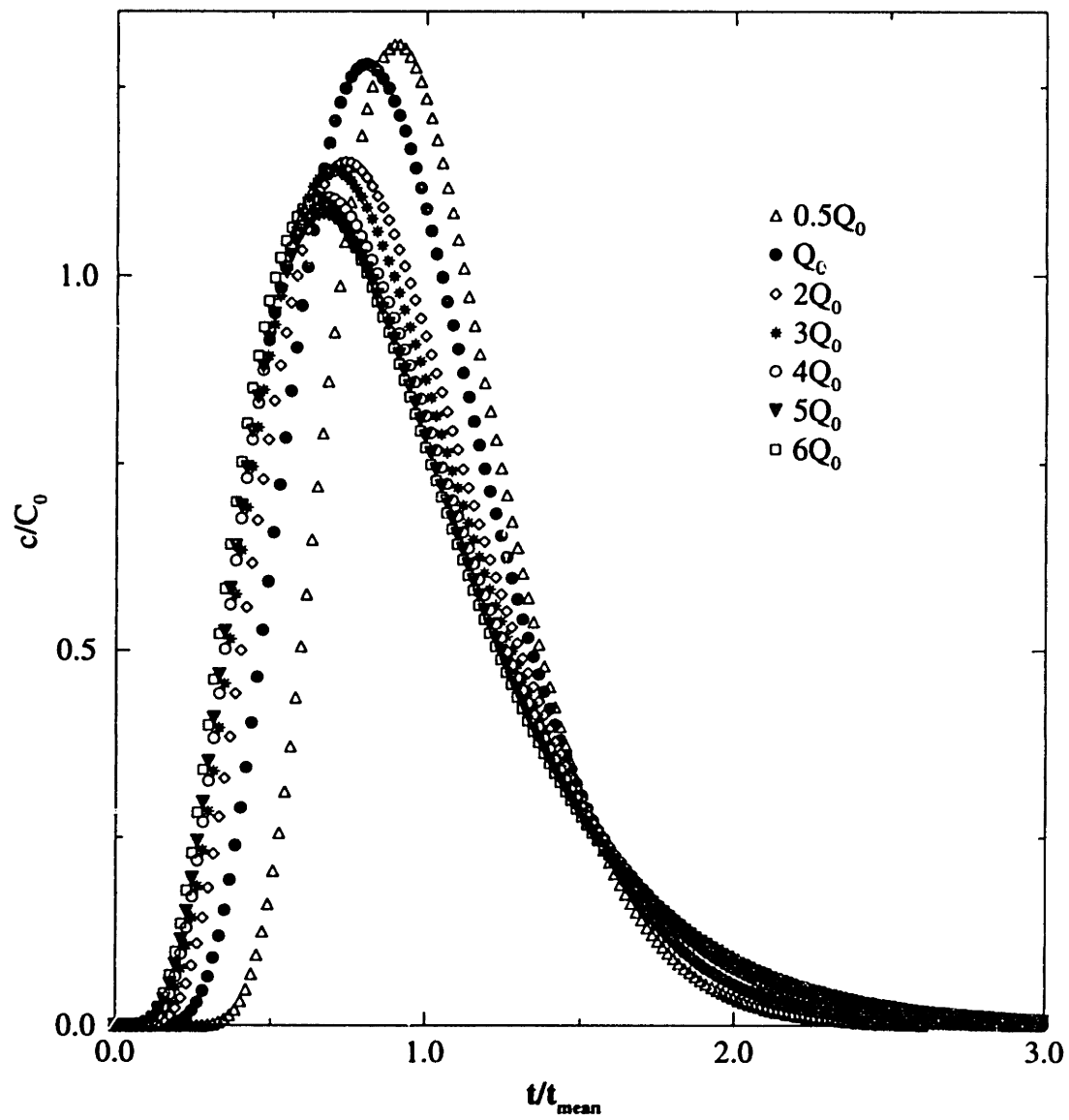
Figure 4-7: Variation of C-curves with the gas volume flow rate for a 4-nozzle system $(Q_o = 4.52 \, l/min)$.

rate value.

Further analysis is needed to find out the explanations for the sharp changes.

4.3.2 Reactor Aspect Ratio

A series of tests were conducted to investigate the effect of the reactor aspect ratio (i.e., H/W) on the mixing behavior of the system. The tested aspect ratios ranged from 0.6 to 1.4.

Figure 4-10 shows the effect of aspect ratio on the system inverse Peclet number D_e/uL. The results are analyzed as follows: When the aspect ratio is above a certain value around 0.8, it seems that the dispersion number D_e/uL increases as the aspect ratio increases, i.e., the system deviates from plug flow behavior. When the aspect ratio is less than around 0.8, the situation is just the opposite (i.e., as the aspect ratio decreases, the dispersion number increases). Therefore, it is considered that there is an optimal aspect ratio at which the system is closest to a plug flow reactor. From the figure shown, the optimal aspect ratio should be around 0.8. The actual residence time analysis for a 4-nozzle system confirms this suggestion, as depicted in Figure 4-11. The figure shows that an aspect ratio of about 0.8 corresponds to a normalized residence time of about 1.0.

4.3.3 Horizontal Liquid Velocity

The effect of the horizontal fluid flow rate on the mixing behavior of the reactor is shown in Figure 4-12. The values of the dispersion number D_e/uL decreases with increasing the horizontal fluid flow velocity, probably because an increase in fluid flow velocity decreases the average residence time of the fluids in the reactor, as well as the intensity of recirculation caused by the plumes. It is easily seen from the definition of dispersion number D_e/uL that increasing of u would decrease the value of the dispersion number. In order to isolate this effect, Figure 4-6 (plotted earlier as a comparison with the experimental results obtained at UMR) illustrates the variance of the longitudinal diffusivity D_e with the horizontal fluid flow rate. As
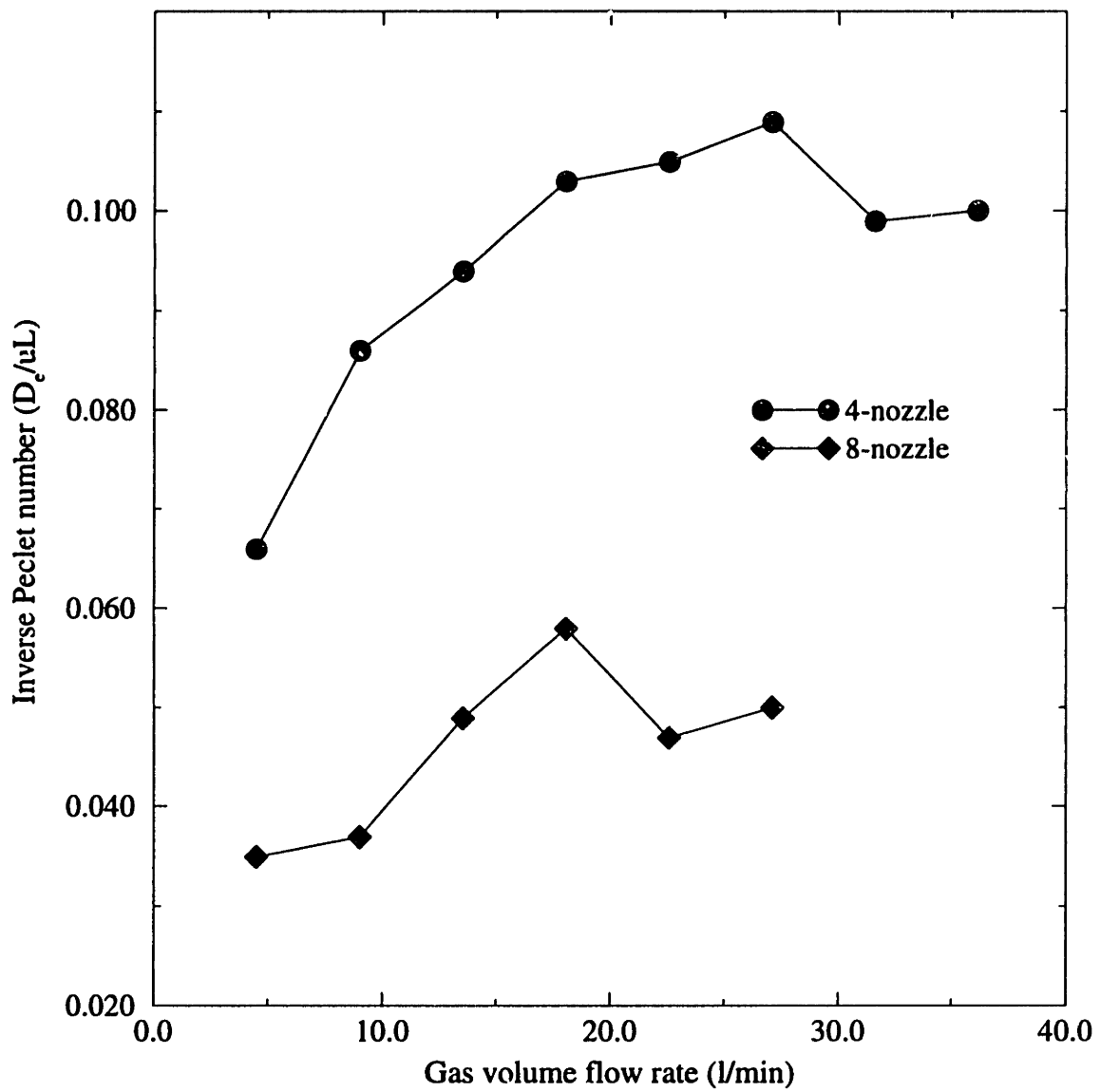
Figure 4-8: Variance of vessel dispersion number D_e/uL with the gas flow rate.
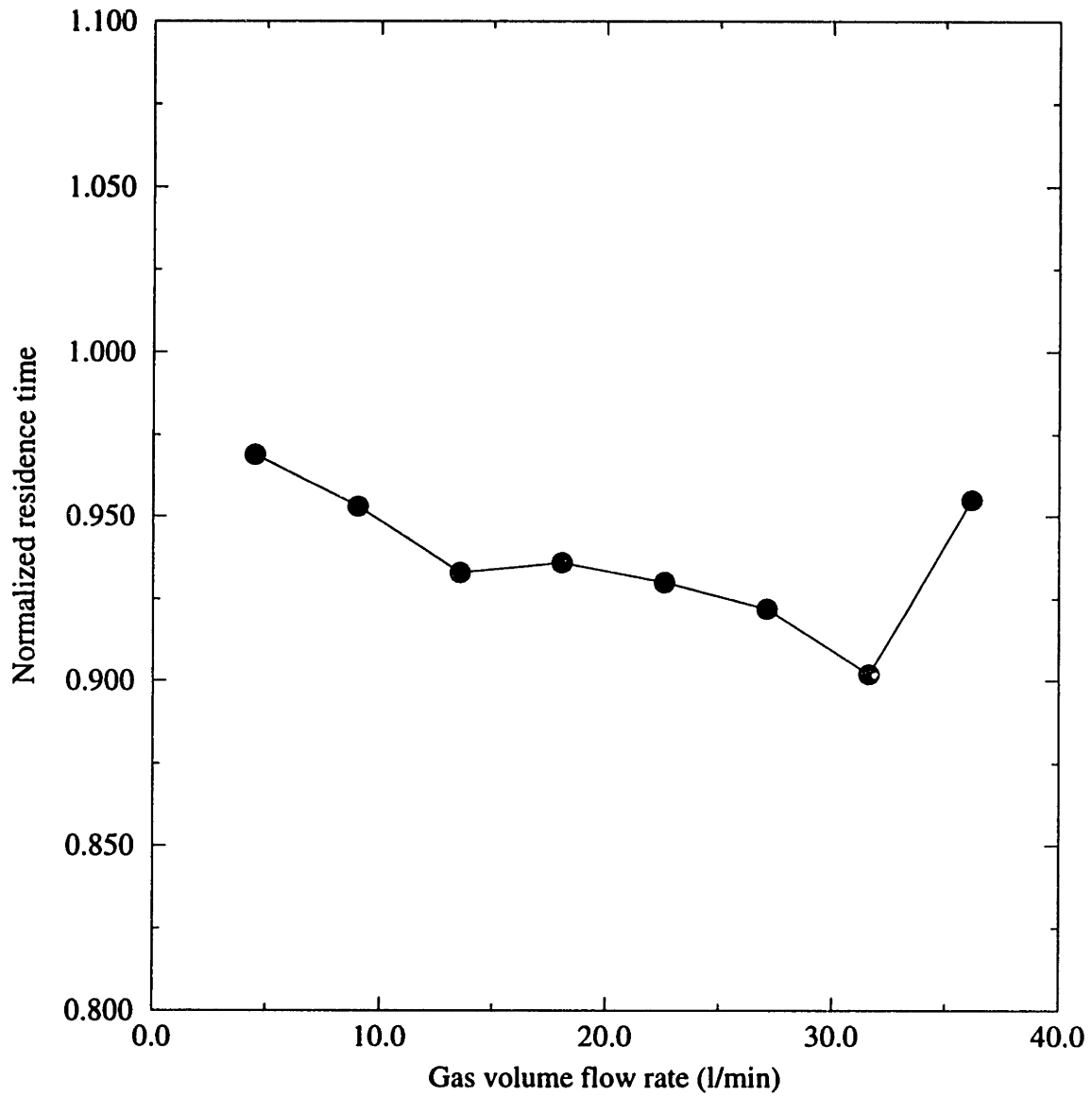
Figure 4-9: Variance of actual residence time with the gas flow rate for a 4-nozzle system.
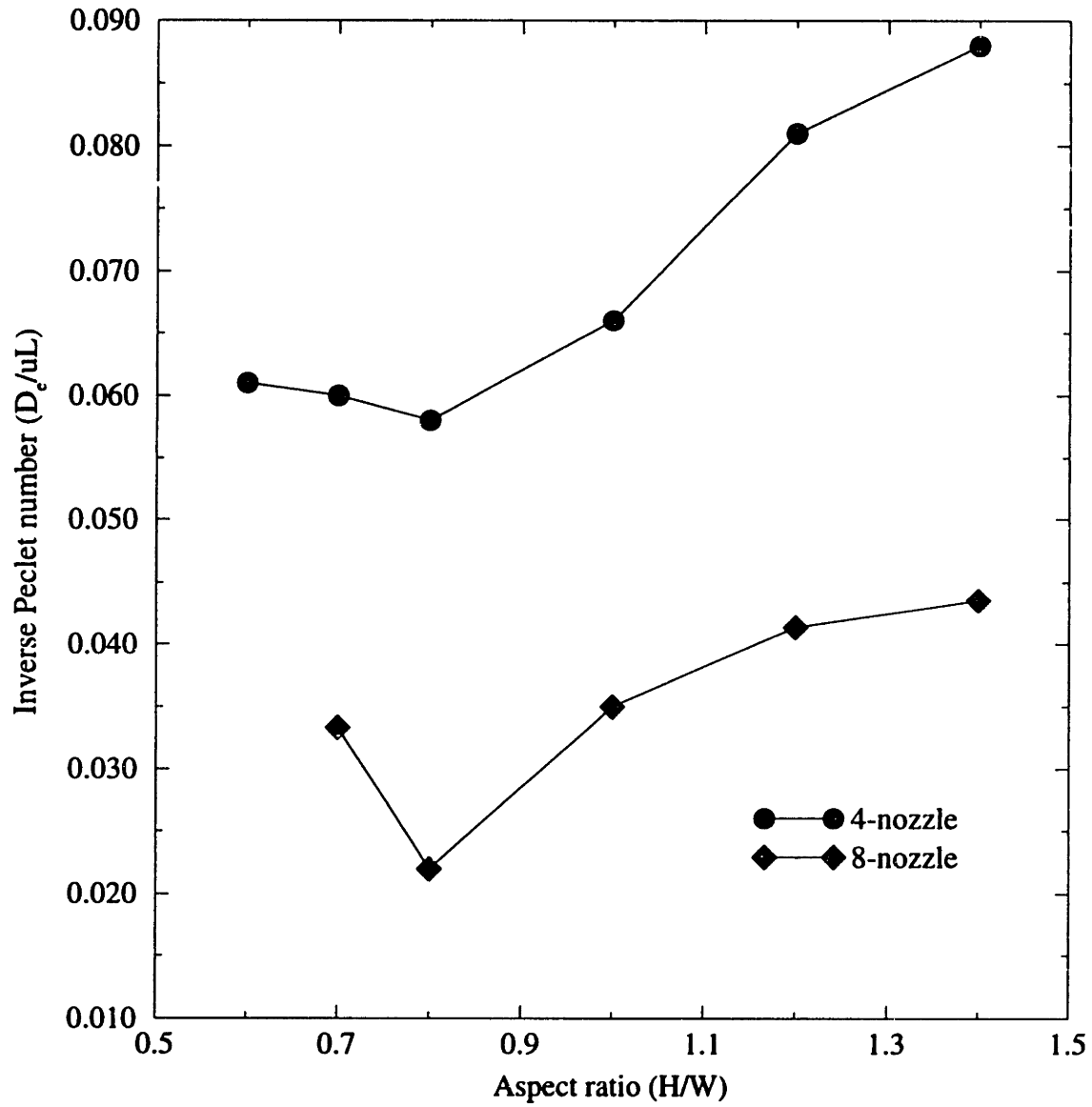
Figure 4-10: Variance of vessel dispersion number with reactor aspect ratio (H/W).
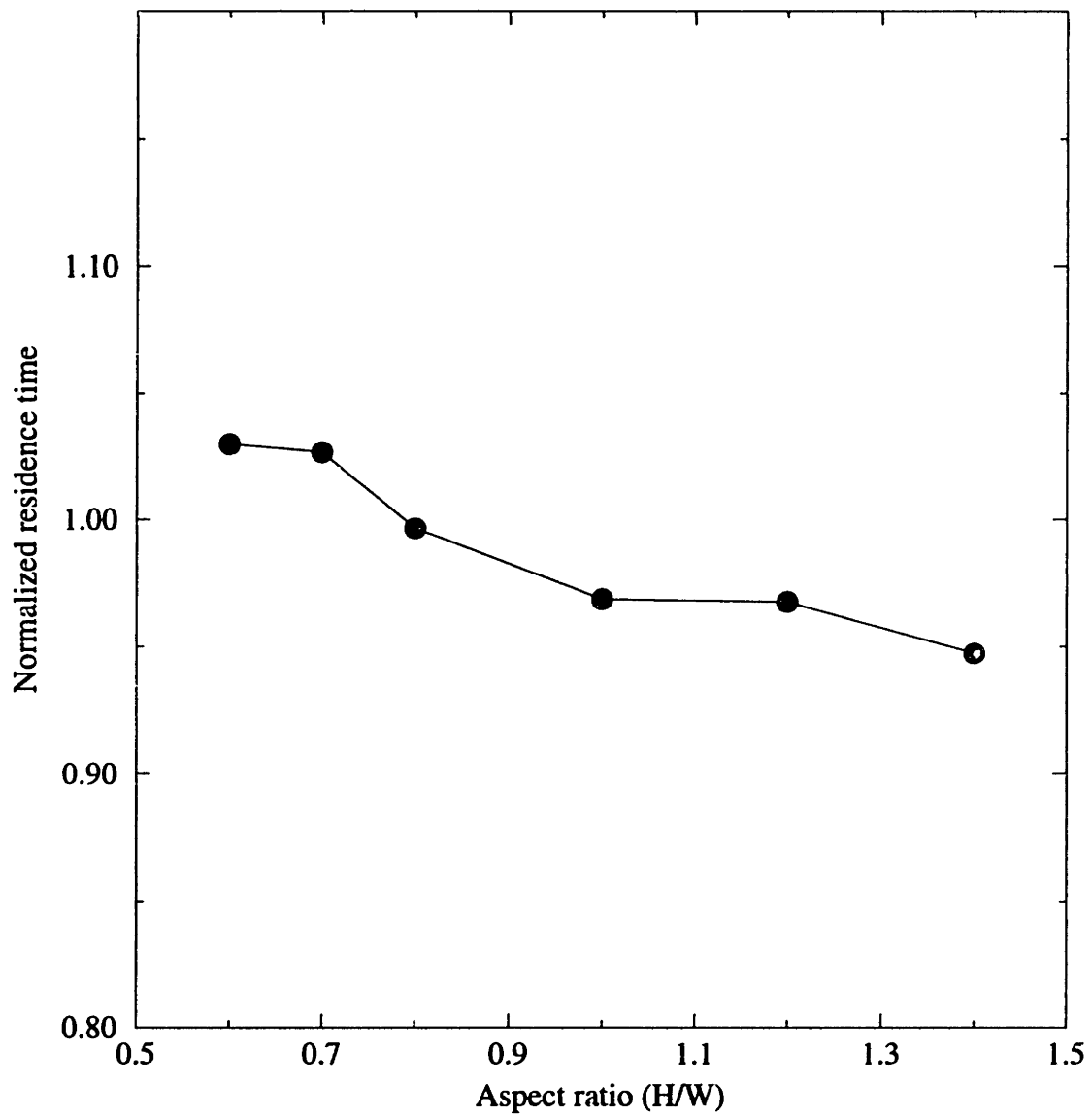
Figure 4-11: Variance of actual residence time with reactor aspect ratio for a 4-nozzle system.

one can see, increasing the horizontal fluid flow rates does increase the diffusivity, probably because of the increase of convection. The conclusion can be supported by the variance of the normalized residence time with the horizontal flow velocity, as shown in Figure 4-13. The normalized residence time approaches unity with the increase of the horizontal flow velocity, which means that the fluid flow approaches plug flow behavior.

4.3.4 Bubbler Separation

Most of the simulations carried out on channel-type reactors were first concentrated on the 4-nozzle and 8-nozzle systems. In order to investigate the effect of bubbler separation on the flow behavior in the reactors, additional systems with different number of nozzles were also considered. In addition to results presented in previous subsections, a 2-nozzle and a 6-nozzle system were simulated. The results of this analysis indicates that increasing the number of nozzles (i.e., decreasing bubbler separation) promotes plug flow condition, as other operating parameters are kept the same. This is shown in Figure 4-14 where the inverse Peclet number increases as the bubbler separation increases. The dependency is approximately linear.

4.4 More Detailed Studies on the Channel-Type Reactors

In order to understand the specific effect that each bubbler has on the overall longitudinal mixing behavior of the channel-type reactor, a more detailed study was conducted. Several cross sections of the system were chosen where tracer concentrations were recorded and the dispersion number for a particular section of the system was investigated. These sections were chosen at different distance from the inlet, corresponding to transverse planes located at the same position as different nozzles or planes at the mid-distance between nozzles.

The planes at or between the nozzles were numbered from low x to high x as 1,
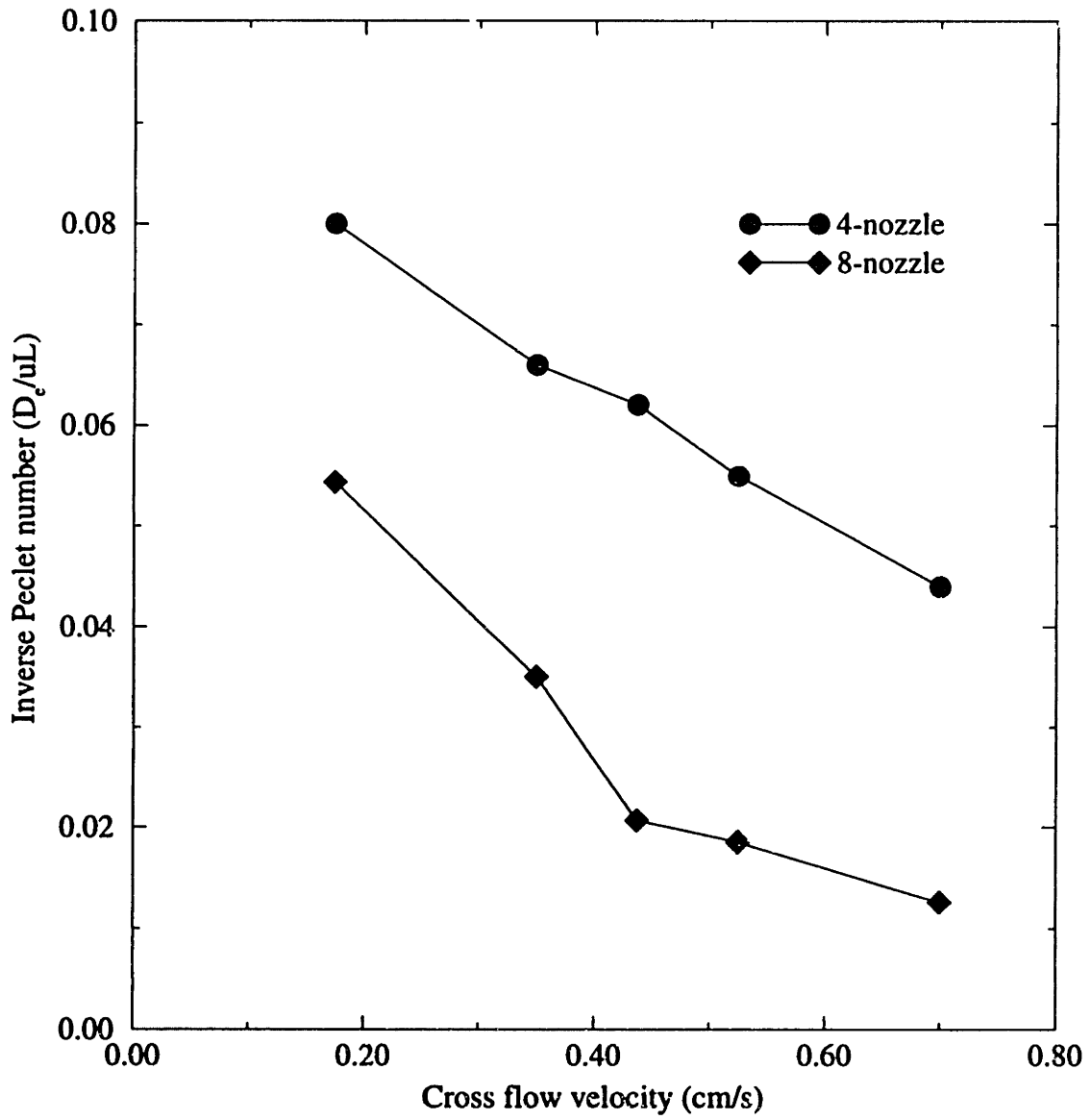
Figure 4-12: Variation of vessel dispersion number with the horizontal liquid flow velocity.
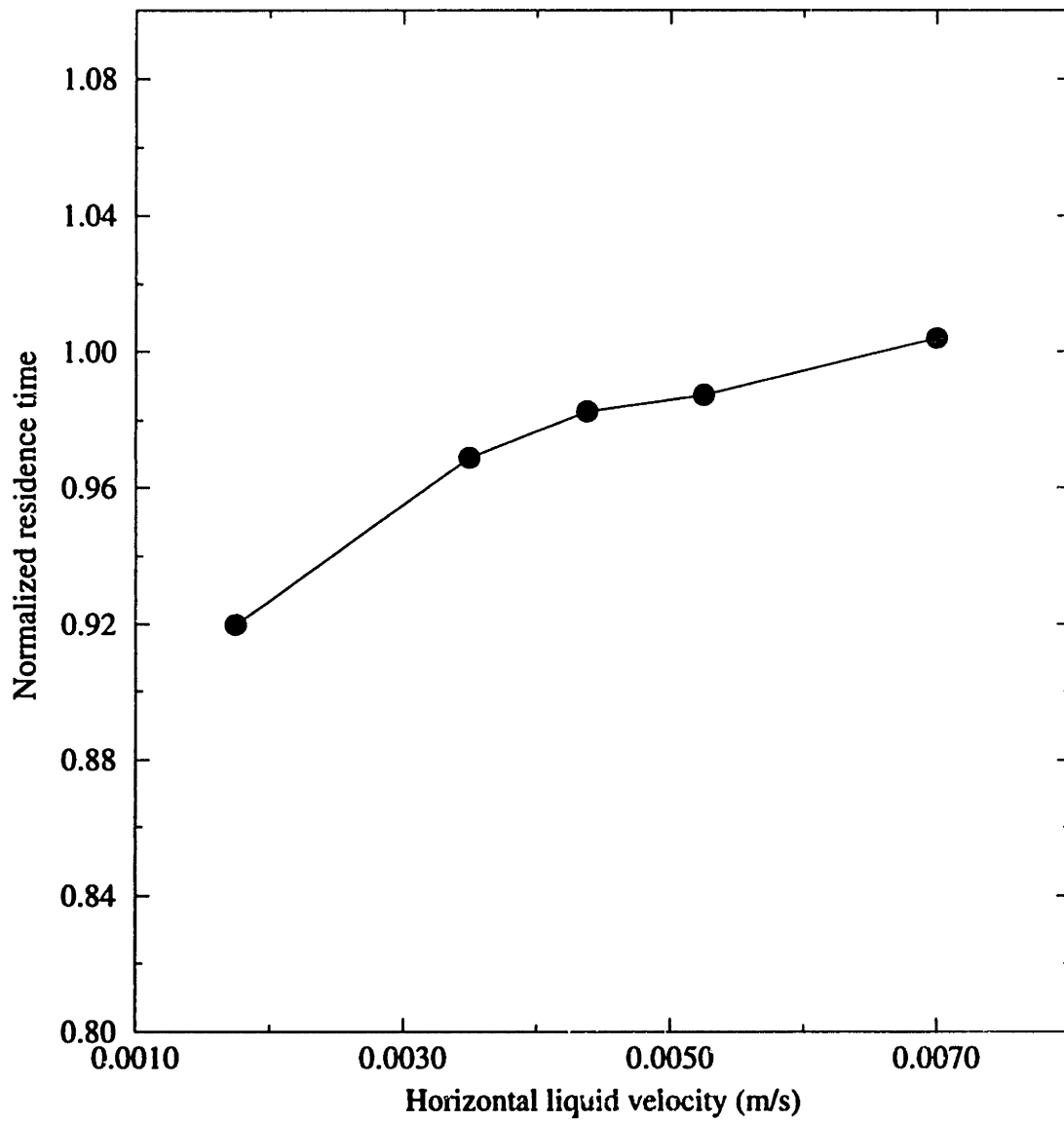
Figure 4-13: Variance of actual residence time with horizontal liquid flow velocity for a 4-nozzle system.
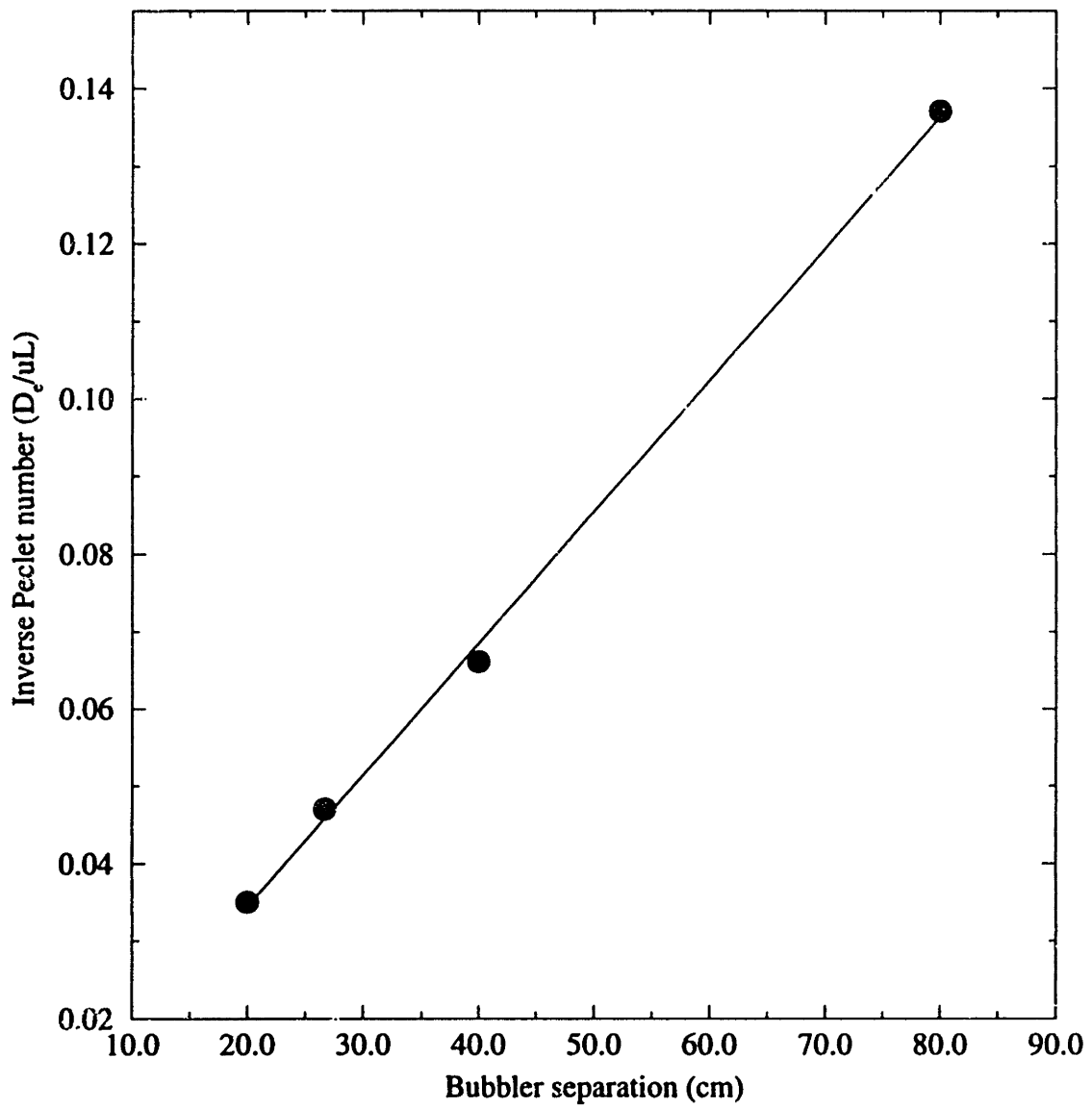
Figure 4-14: Variance of inverse Peclet number with the bubbler separation (small values of bubbler separation means more number of nozzles).

2, 3 ..., depending on the number of nozzles the system has. Each calculated C-curve represented the system behavior from the inlet of the reactor to that particular plane. For a 4-nozzle system used in this investigation, there were three mid-nozzle planes between the four nozzles. Three C-curves were obtained at the internal positions and the results are shown in Figure 4-15. The 4th curve shown in the plot is the one representing the behavior for the whole system (i.e., obtained at the outlet of the system). In order to normalize these curves and to be able to compare them on the same plot, the specific volumes and nominal residence times were taken into account for each one of the sections considered.

It is seen in the figure that as the flow moves down stream, passing increasing number of nozzles, the tendency is to approach plug flow behavior. In other words, the curves suggest that a more intense longitudinal dispersion is felt in the vicinity of the inlet, i.e., for less number of nozzles.

A similar plot shows the C-curves obtained at the four nozzle planes (see Figure 4-16). Similar tendency is observed in this figure, but an interesting feature (not found in the previous plot) is the "shoulder" that appears on the left side of the first C-curve. This behavior could be explained probably as an entrance effect or due to fluid by-passing.

Dispersion numbers were also calculated as a function of the distance x, and these are shown in Figure 4-17. It is seen that even for different nozzle configuration (4-nozzle vs. 8-nozzle) and flow rates, the inverse Peclet number tends to an asymptotic value of about 0.1, as the distance from the inlet increases.

In order to isolate the effects of the velocity and length on the dispersion number from the previous results, the longitudinal diffusivity alone is shown as a function of the distance in the longitudinal direction. These values were obtained by multiplying by the corresponding horizontal velocities and distances, and the resulting values are plotted in Figure 4-18. It is seen that the longitudinal diffusivity decreases as the distance from the reactor inlet increases.
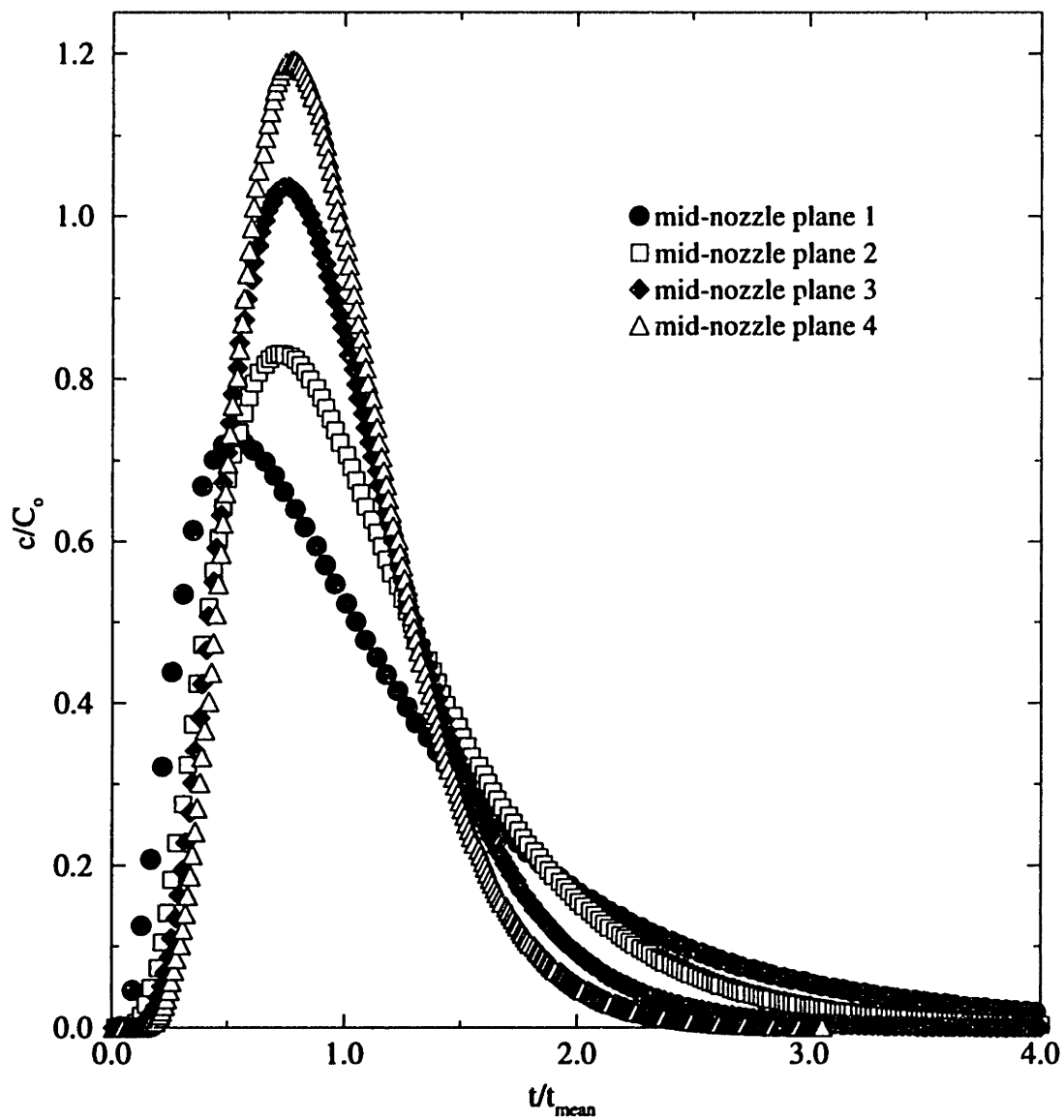
Figure 4-15: C-curves obtained at mid-nozzle planes showing the effect of each bubbler on the system behavior for a 4-nozzle system (Q = 9.04 l/min).
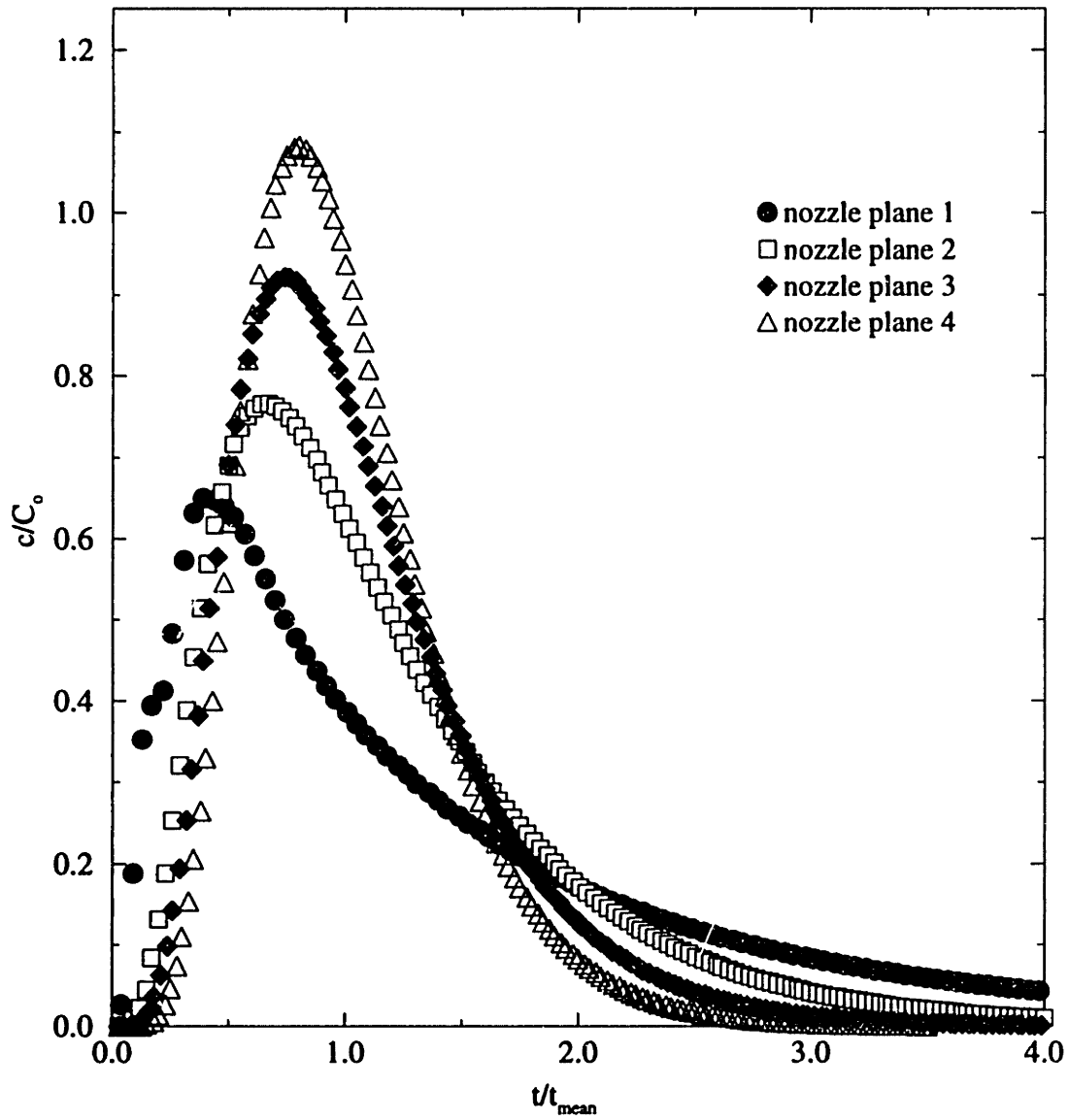
Figure 4-16: C-curves obtained at nozzle planes showing the effect of each bubbler on the system behavior for a 4-nozzle system ($Q = 9.04\,l/min$).
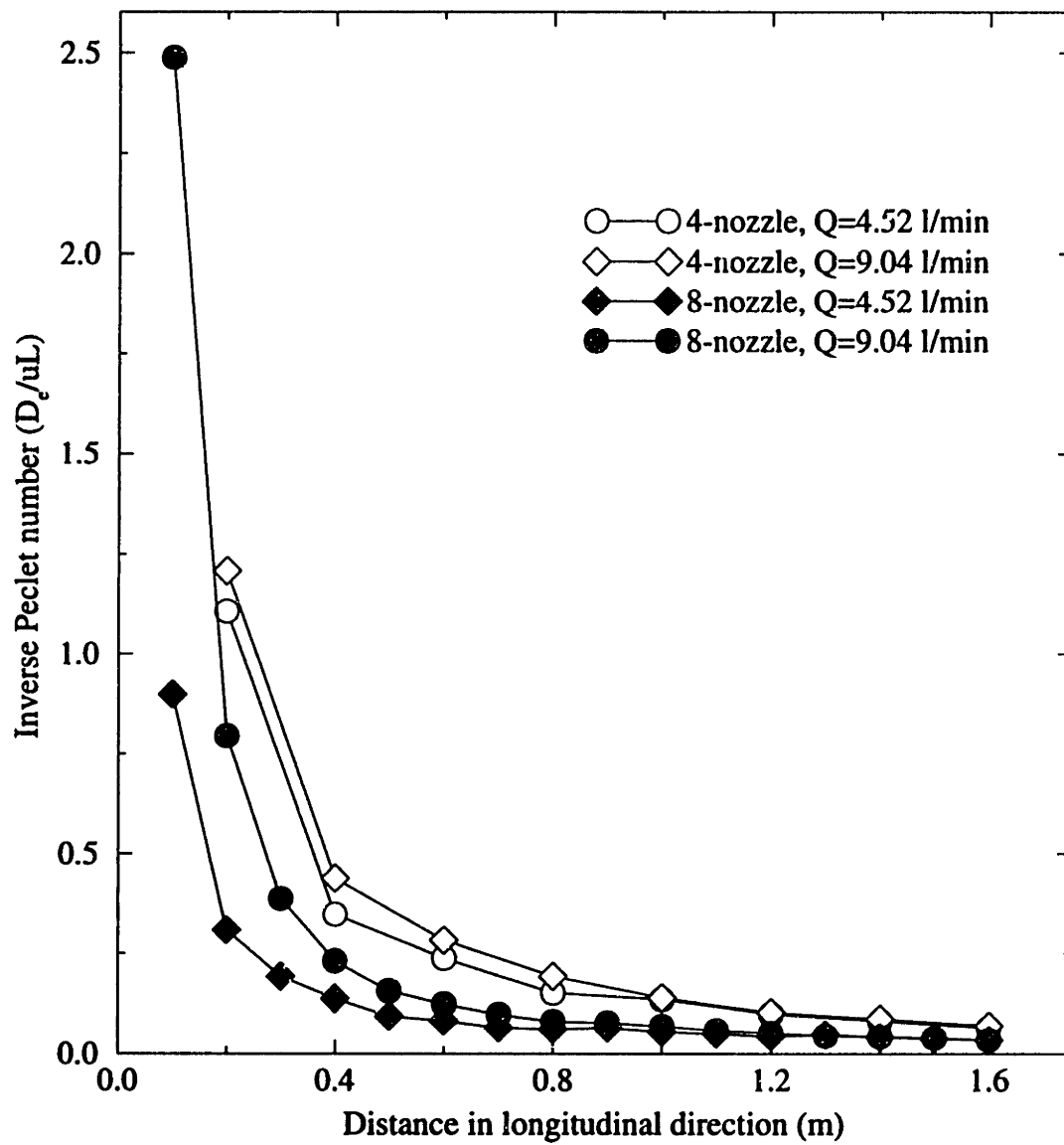
Figure 4-17: Dispersion number as a function of the longitudinal distance x.
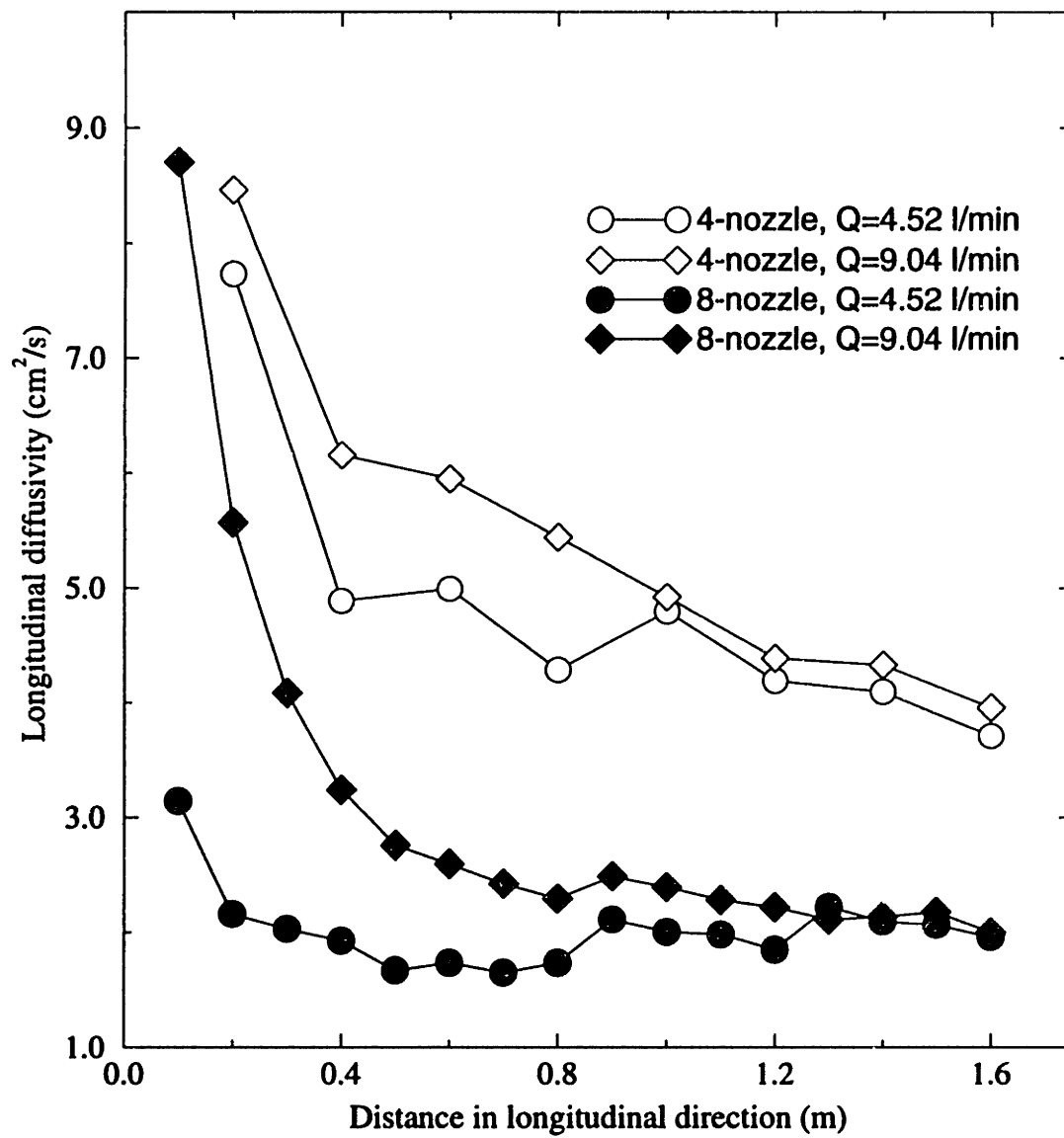
Figure 4-18: Axial diffusivity as a function of the longitudinal distance x.

4.5 Consideration of the Third Phase

Most of the physical modeling work reported in the literature includes only two phase systems due mainly to the complexity of making realistic measurements when an additional third phase is considered. Representing interfacial phenomena occurring in metal-slag system by using physical models (e.g., water plus organic solution) is indeed a difficult task and it is still in a state of early development.

From the point view of mathematical modeling, the situation becomes even more complicated. This is not necessarily because of having to solve an additional set of equations, but because the interactions between three simultaneous phases remains unknown.

4.5.1 Velocity Profile Near the Liquid-Liquid Interface

In order to assess the effect of a third phase on the simulation results reported so far, a simplified approach was taken. This consisted on assuming a counter-current system under laminar flow regime without gas injection at the bottom. The velocity profiles for each phase can be solved analytically if a slip velocity is assumed at the interface. The full derivation of the velocity profiles and the corresponding results are presented in Appendix B. The results of the simplified counter-current model suggest that the effect of a second top liquid phase on the lower liquid phase is negligible for the ranges of conditions in this study. As assumed in Appendix B, where considering an extreme case (i.e., V_{slip} is a minimum), the velocity at the interface for the lower liquid phase will be of the order of less than $1\,cm/s$. This value is two orders of magnitude less than the typical velocities promoted by the gas injections in the system that we are considering.

A sensitivity study was also performed to further investigate the effect of the third phase by imposing different values of velocities of the same order as in the experiments at the upper boundary of the computational domain, the results did not show any effects either on the resulting C-curves or on the local velocity profile (i.e., in the vicinity of the top surface).

4.6 Summary

Several fundamental conclusions can be drawn from the analysis conducted in this chapter regarding the prediction of fluid flow and overall longitudinal mixing characteristics in a channel-type reactor.

- Particle tracking analysis showed that the fluid moves from inlet to outlet of the reactor in a spiral fashion, indicating that the planes where the main fluid recirculation occurs is perpendicular to the longitudinal direction of the reactor. Velocity profiles confirm such overall flow patterns.

- As the gas flow rate injected into the liquid increases, the system departs from plug flow behavior.

- Increasing the horizontal fluid flow rate promotes plug flow behavior and increases longitudinal diffusivity.

- An optimal aspect ratio of around 0.8 (H/W) is suggested from fluid flow (mixing) considerations.

- Plug flow behavior is promoted by increasing the number of nozzles, under the same operating parameters.

- It seems that the fluid flow behavior approaches plug flow conditions even under gas flow rates as high as 40 l/min.

Chapter 5

Mass Transfer Analysis

5.1 Introduction

Gas injection into molten metals plays an important role in industrial refining operations since it is used to promote stirring in metallurgical vessels both to avoid concentration and thermal stratification and to increase the rate of different types of homogeneous or heterogeneous reactions. Gas stirring not only promotes turbulent mixing but also increases the contact area between interacting phases.

Mass transfer in metallurgical processes, involving refining operations of liquid melts, can be classified into three categories according to the type of interactions that occur: mass transfer taking place between gas and liquid (gas absorption or desorption or gas-liquid reactions), between liquid and liquid (slag-metal reaction), or between solid and liquid (reaction with particles, solid additions or refractories).

The main focus of this chapter is the analysis of liquid-liquid mass transfer processes (i.e., reactions taking place between a melt and a slag), since this represents the main component involved in the continuous counter-current reactor concept. In a similar way to the analysis presented in the previous chapter, we are concerned specifically in the analysis of the performance of the physical model developed at the University of Missouri-Rolla (UMR).

Although many studies have been reported addressing slag-metal systems, mass transfer phenomena at the metal-slag interface are not well understood, in particular

with regard to fluid flow aspects, including turbulence characteristics.

As mentioned in Chapter 1, there are several basic requirements for a successful continuous metallurgical reactor, from which the critical ones are: minimum (low) longitudinal mixing, maximum (high) transverse mixing, and sufficient interphase mass transfer rate. This is because it is necessary to keep a high driving force for mass transfer in the vertical direction (between the two liquid phases) and an enhanced mass transfer rate (promoted by the stirring gas).

Mass transfer analysis is an indispensable component for the assessment of the feasibility or the performance of a continuous metallurgical reactor. It is even more important in considering the design of a pilot or industrial size reactor.

In this chapter, the mass transfer behavior between two immiscible liquids is mathematically modeled. The distribution of concentration along the length of the reactor, as well as in a transverse cross-section, is analyzed. Particular attention is given to the assessment of conversion rates resulting from exploring different operating conditions.

5.1.1   Approach

Extending the development of the two-phase fluid flow model (described and used in previous chapters) to incorporate mass transfer capabilities can be considered a relatively easy task; however, given the limitations of such a model to deal with a third phase and the need for various experimental conditions/parameters required to deal with the mass transfer analysis, the task becomes rather more difficult. Therefore some assumptions need to be carefully defined.

In simple terms, we can consider that the main purpose of the counter-current channel-type reactor, from a purely mass transfer standpoint, is to efficiently transfer specific species from one phase to the other. To analyze this problem we need to consider a specific system so as to define the mechanisms governing the separation or exchange of such species, the limiting step(s) and, of course, the corresponding thermophysical properties involved for such system.

As already mentioned above, the scope of this research work is aimed at the analy-

sis of the counter-current channel-type system, which is based on a water model, with the intention to prove a concept; however, to date, mass transfer experiments on this system are not completely defined and only preliminary experiments have been carried out to measure parameters related to mass transfer, such as overall mass transfer coefficients. As will be discussed in subsequent sections, such parameters have been measured indirectly, since the experiments employed a thermal tracer technique and used the analogy between mass and heat transfer to obtain mass transfer coefficient.

Given the above background, it should be stated that it is necessary to reformulate some key aspects of the system under study in order to establish an appropriate formulation of the problem and to be able to perform meaningful calculations on the mass transfer characteristics in the UMR physical model. These key issues involve:

- Selecting a system with suitable species or components to represent mixing and mass transfer across the liquid-liquid interface in the water model which can guarantee some similarity with a relevant metallurgical operation.

- Establishing an approach to evaluate mass transfer coefficients between immiscible liquids.

- Seeking a way to incorporate the effect of the third (top liquid) phase.

- Establishing the criterion to evaluate reactor performance and compare its sensitivity in terms of process conditions.

The above aspects constitute the critical issues that need to be resolved in order to study the mass transfer behavior in the continuous counter-current reactor concept. These aspects are discussed and justified in the subsequent sections.

Some Background The reactions which occur between the phases in a metal refining process are frequently very complex because they involve the coupled transfer of many components and the evolution of gases.

Steel refining operations, for example, in general include decarburization, desulfurization, dephosphorization, inclusion flotation, hydrogen removal and nitrogen removal, to name a few. Among them, desulfurization and dephosphorization represent

important steps required to guarantee high quality products, and they are mainly achieved by slag-melt extraction processes. The overall chemical reactions describing the thermodynamics of these two processes are:

$$3(CaO) + 2\underline{Al} + 3\underline{S} = 3(CaS) + (Al_2O_3) \tag{5.1}$$

and

$$5(FeO) + 2\underline{P} = (P_2O_5) + 5\underline{Fe} \tag{5.2}$$
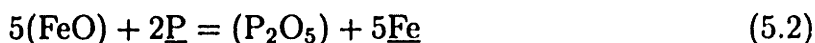
where the parentheses represent species dissolved in the slag phase and the underlines indicate species dissolved in the metal phase.

A great deal of experimental work has been reported in the literature describing the analysis of mass transfer process between melts and slags. Whether water models or metallic systems in lab size scales are used in representing mass transfer processes (i.e., physical modeling) between metals and slags, desulfurization operations have received wide attention [6, 32, 59, 66, 74, 84, 87-89, 95]. For a brief description of the desulfurization process in steelmaking, the reader is referred to Appendix C.

In the following sections we review some of the important studies involving the mass transfer operation between two liquid phases. This previous work represents the basis on which we fundament the calculations and analysis subsequently presented in this chapter.

5.1.2   Relevant Experimental Work on Liquid-Liquid Mass Transfer Studies

A number of experimental groups have addressed the study of mass transfer rates involved in refining operations. Their main purpose was to determine the controlling mechanisms for specific processing systems and to establish the overall mass transfer rates (i.e., mass transfer coefficients across the interface involved in the refining processes).

Asai et al. [74] published an excellent review of mass transfer operations involved

in ladle refining processes. In their article, they presented a comprehensive summary describing mass transfer phenomena between liquid-liquid phases. They also included correlations relating the effect of the gas flow rate on the rate of mass transfer between typical slag-metal systems.

In a more recent review, Mazumdar and Guthrie [3] also presented a brief summary of the relevant work involving the study of mass transfer processes in liquid-liquid metallurgical systems. As stated in their paper, a great deal of experimental work has been reported, dealing with water model systems and focusing mainly on the study of desulfurization operations in steelmaking refining.

Table 5.1 summarizes some of the relevant physical modeling work involving mass transfer phenomena between two immiscible liquids (metal-slag). In most cases, the rate of slag-metal mass transfer was determined by monitoring the rate of transport of a tracer in the experimental system. It should be stressed that, in order for a physical model to be able to represent the characteristic behavior of steelmaking metal-slag systems, a number of similarity conditions, between model and prototype, have to be satisfied. These include geometric, dynamic, and chemical constraints, just to name a few. In particular, for the cases involving separation or chemical reactions between adjacent phases, the partition ratios of the species in the phases have to be the same. This condition represented the main focus in selecting the specific systems listed in Table 5.1. As seen in the table, experiments using physical models normally involve water and an organic liquid (e.g., benzene) to represent slag-metal systems. In analogy to the transfer of species between metal and slag such as sulfur or phosphorous, tracers of organic species are usually employed, such as thymol or caprylic acid. It has been generally found that the mass transfer rate between a metal and a slag can be increased significantly (a factor of 10 to 100), depending on the blowing conditions used (i.e., geometric arrangement, aspect ratio, gas flow rate, etc.) [83].

As shown in Table 5.1, a wide range of values of the mass transfer coefficient were experimentally determined in the different studies, although some of the results are presented in parameters other than mass transfer coefficients because of the dif-

Table 5.1: Mass transfer coefficients from experimental work.

Model system	Transferred species	Mass coeff.(cm/s)	Investigators and ref.
water/tetraline	benzoic acid	1.0×10 (1/s)	Asai et al. [74]
TCE/water	none	0.004, 0.02	Robertson et al. [78, 79]
water/oil	thymol (S)	$0.6 \sim 2.1 \times 10^{-2}$	Kim and Fruehan [32]
water/oil	caprylic acid (S or P)	$4.5 \sim 8.5 \times 10^{-3}$	Gerlach and Frohberg [82]
water/benzene	acetophenone	$0.5 \sim 2 \times 10^{-2}$	Taniguchi et al. [66]
water/cyclohexane	iodium (S)	$5 \sim 35 \times 10^{-4}$ (1/s)	Mietz et al. [59]
water/oil	caprylic acid	2.13×10^{-2}	Koch et al. [7]
water/benzene	iodine	50 (cm^3/min)	Paul and Ghosh [95]
Cu/slag	Si	$0.01 \sim 0.1$	Hirasawa [84]
iron/slag	S	$5.52 \sim 29.02 \times 10^{-3}$	Deng and Oeters [88]
iron/slag	Mn, Si	$0.005 \sim 0.03$	Xie and Oeters [89]
iron/slag	S	$0.156 \sim 1.03 \times 10^{-2}$	Gupta et al. [87]

ficulties in making direct measurements. Of course, they involve not only different experimental systems but also conditions, and almost all of them are based on a cylindrical shaped system. It is important to note, however, that the values for the mass transfer coefficient reported in the different studies are in the range from 10^{-3} to 10^{-1} cm/s.

Experimental Work at UMR As mentioned in Chapter 1, the main focus of the experimental work at University of Missouri-Rolla was to characterize experimentally the performance of the counter-current reaction launder (CCRL) in terms of establishing the rate of mass transfer process involving refining operations. Experimental measurements for both two-phase (water-nitrogen) and three-phase (TCE-water-nitrogen) systems were conducted at UMR as the counterpart of this project. In the experiments, they used a technique based on thermal tracers (heat pulses from a heating element and continuous temperature measurements) for the determination of the longitudinal mixing, together with the interphase heat transfer coefficient. A heat pulse of about 150 kJ was applied during a period of 30 seconds. The evolution of the temperature response (thermal tracer) through the reactor was then monitored until the thermal effect had dissipated. The sensors were positioned in such a way

113

that it was possible to monitor the "dispersion" of the thermal tracer both along the independent liquid phases (to provide longitudinal mixing) and across the immiscible liquids (to determine the interphase heat transfer coefficient). The longitudinal mixing analysis was based on the calculation of the RTD's (residence time distributions), from which D_e/uL was estimated. The interphase mass transfer coefficient was estimated using relationships from the heat and mass transfer analogy. Their experimental results suggested the possibility of maintaining acceptably low longitudinal mixing ($D_e < 20$ cm^2/s and $D_e/uL <0.1$) in the CCRL. Interphase mass transfer coefficients of the order of 0.004 cm/s (for Q = 24 l/min) and 0.02 cm/s (for Q = 40 l/min) were predicted from the measured interphase heat transfer coefficients.

5.1.3   Estimation of Mass Transfer Coefficients

In doing mathematical modeling work involving mass transfer between two immiscible liquids, ideally, one will need to first define the possible mechanisms and identify the rate limiting step(s). Furthermore, one will require specific values or appropriate correlations to set up the model (e.g., mass transfer coefficient); which should be measured experimentally for the similar conditions (i.e., geometric configurations, flow rates, densities etc.).

Most of the measured mass transfer coefficients for liquid-liquid interfaces reported in the literature have been obtained from a cylindrical system (e.g., from physical models or industrial measurements); however, experimental correlations are not available for the kind of configuration of interest in this thesis (i.e., channel-type system).

The current experimental measurements carried out at UMR have provided some preliminary data for the mass transfer coefficient of the system; however, these values are currently assumed to be only qualitative in nature at this point.

Alternatively, the mass transfer coefficient can be estimated using theoretical models, such as the ones based on the film theory and penetration theory which will be briefly described in the following paragraphs.

Film Theory In this model [96], a stirred fluid such as a liquid metal is considered whose bulk is in a state of fully developed turbulent motion. This turbulence is damped out at the surface of the liquid, e.g., at the slag-metal interface, in a way similar to that near a solid surface. In the vicinity of the interface, it is assumed that mass transfer of a species i occurs solely by molecular diffusion, and this represents the total resistance to mass transfer in the fluid. The thin layer next to the interface is assumed to be stagnant with a thickness L. Under the assumption of the film theory, the mass transfer coefficient at the interface is represented as

$$k = \frac{D}{L} \tag{5.3}$$

where D is the diffusion coefficient of species i in the liquid phase.

This rather simplistic model represents a first attempt to establish the rate of mass transfer at the interface. The important limitations of this model are the simplicity of the concept of a thin stagnant layer and the difficulties of predicting the value of thickness L.

Penetration Theory This theory also assumes a fluid which is fully turbulent. However, it is considered in this model that the turbulence extends all the way to the interface. Numerous eddies or "packets" of fluid from the bulk penetrate to the surface. At the interface, the solute in the packet diffuses across into the second phase. After a certain time the packet of fluid at the interface is swept back into the bulk by more eddies, and a new packet takes its place. From this model, the average mass transfer coefficient can be obtained as

$$k = 2\sqrt{\frac{D}{\pi t_c}} \tag{5.4}$$

where t_c is the lifetime or contact time of the fluid packet, or so called the surface renewal time. The penetration theory [97] is also the called surface renewal theory. For more detailed information regarding the two theoretical models, the reader is referred to references [90, 91].

Table 5.2: Experimental correlations and theoretical models for predicting mass transfer coefficients.

Exp. correlations	Investigators	Theo. models	Investigators
$kA = 8.3Q^{1.2}$ (small vessel) $kA = 16.8Q^{1.2}$ (large vessel)	Gerlach and Frogberg [82]	$k = 2\left(\frac{D}{\pi t_e}\right)^{1/2}$	Higbie [97]
$k = \left(\frac{BDQ}{d_c}\right)^{1/2}$	Robertson and Staples [93]	$k = 1.46(D\overline{u'}/\Lambda_f)^{1/2}$	Fortescue and Pearson [99]
$kA = 138D^{0.5}Q^{0.5}r_1$	Taniguchi et al. [66]	$k = 0.5(\frac{\varepsilon}{\nu})^{1/4}D^{1/2}$	Kataoka et al. [77]
$kA = 18.2Q^{0.5}$	Paul and Ghosh [95]	$k = c(\frac{\varepsilon}{\nu})^{1/4}D^{1/2}$	Lamont and Scott [100]
$kA \propto Q^n$ $n = 0.27 \sim 0.398$ for $Q < Q^*$ $n = 0.132 \sim 0.14$ for $Q > Q^*$	Singh and Ghosh [104]	$k \propto (\frac{\overline{u'}^3 \Lambda_f D}{\nu})^{1/2}$	Henstock and Hanratty [101]

** See Nomenclature on page 14 for the meaning of the symbols

On the basis of the "penetration theory," various mass transfer models to estimate the rate of turbulent mass transfer have been suggested. Table 5.2 summarizes some of the theoretical models available and some experimental correlations for comparison. It is well known that turbulent flows contain numerous eddies with various length scales. Fortescue and Pearson [99] have assumed that the surface is renewed only by the largest eddies. On the contrary, Kataoka et al. [77] derived their model by assuming that the surface is renewed by the smallest eddies, which have the highest renewal frequency. Lamont and Scott [100] proposed a model similar to the one by Kataoka et al., but they assumed that the surface renewal must occur by every eddy with its scale ranging from the smallest one to the largest one. Theofanous et al. [103] have suggested an alternative model, the augmented large eddy and dual regime model, developed for open channel flows and defined in terms of the Reynolds number. The model supported the small-eddy model at eddy Reynolds numbers greater than 500, and the large-eddy model at Reynolds numbers less than 500.

Of the above models, the following comments can be made: They report alternative ways to estimate the mass transfer coefficient at a free surface of the liquid in

the turbulent regime; however these models and experimental correlations are only applicable within a range of specific conditions and particular geometries.

5.2   The Mathematical Formulation

The mathematical model employed in this study has been described in Chapter 2. In comparison to the results presented in the previous chapter, an additional component was included here to deal with the solution of the species concentration equation. In particular, the key component required involves the estimation of the mass transfer coefficient.

Assumptions   The main assumptions used to represent the system include:

1. Mass transfer at the lower liquid phase is the rate controlling step.

2. The mass transfer coefficient is only related to the flow behavior of the lower liquid phase.

3. No back-diffusion from the upper phase to the lower phase is considered (i.e., when the upper phase reaches saturation, the mass transfer rate is zero).

4. Only two phases (the gas and the lower liquid phase) are considered directly.

Mass Transfer Coefficient   The model derived by Kataoka et al. [77, 66], which assumes the surface is renewed by the smallest eddy having the highest renewal frequency, was adopted in this work to represent the mass transfer at the liquid-liquid interface. In a separate experimental work by Prasher and Wills [107], the small eddy model was supported by their study of mass transfer in an agitated vessel. In the present work, the mass transfer coefficient at the interface is calculated by:

$$k_o = 0.5(\epsilon/\nu)^{\frac{1}{4}} D^{\frac{1}{2}} \tag{5.5}$$

where ϵ and D are values of the turbulence dissipation rate at the liquid-liquid interface and the diffusion coefficient of solute in the lower liquid phase, respectively. The

diffusion coefficient was taken to be $2 \times 10^{-5}\,\text{cm}^2/\text{sec}$ [79].

Concentration in the Upper Liquid Phase The species concentration in the upper liquid phase was calculated by balancing the total mass of species entering and leaving the system and that being transferred between the "two phases." The mass balances for a species can be written as:

For the lower phase:

$$[\text{rate of mass in}] - [\text{rate of mass out}] = [\text{rate of mass to upper phase}] \tag{5.6}$$

For the upper phase:

$$[\text{rate of mass in}] + [\text{rate of mass from lower phase}] = [\text{rate of mass out}] \tag{5.7}$$

The upper phase concentration was then imposed at the top free surface of the computational domain as a variable boundary condition. In this way, iterations were needed to reach convergence in solving the species concentration equation.

The initial concentration in the upper phase was taken as 0.2% in mass fraction at the inlet of the reactor, and the saturation concentration was taken as 2% [73]. A moderate equilibrium partition ratio of 300 was used for most of the calculations in this study.

5.3 Results

Some simple back-of-the-envelope calculations may help to understand the overall mass transfer behavior between two immiscible liquids being stirred by gas injections and to establish a reference for comparison.

Let's assume that we have a perfect plug flow reactor exchanging species with an outside environment at one of its boundaries with a mass coefficient k. The conversion ratio, defined as the ratio of the concentration extracted at the boundary to the initial concentration at the reactor inlet, $\frac{c_i - c_o}{c_i}$, can be estimated by an overall balance using

the following expression:

$$\text{Conversion Ratio} = 1 - \frac{c_o}{c_i} = 1 - e^{kat_R} \qquad (5.8)$$

where a is the surface area per unit volume ($\frac{A}{V}$) and t_R is the average residence time of the reactor. For the derivation of the above formula, please see Appendix D.

Based on the experimental conditions at UMR, the following estimates for the conversion rate can be calculated:

In the first set of experiments, they used a lower range of gas flow rates where the maximum was Q = 24 l/min and a mass transfer coefficient of 0.004 cm/s was reported [78]. The calculated residence time for this case was 457 s. Using the above formula, the conversion ratio would be 8.7%, which is very low.

In the second set of experiments [79], they used a higher range of gas volume flow rates, with a maximum value of Q = 40 l/min. In order to keep the longitudinal mixing low under these conditions, they increased the horizontal liquid flow velocity from 0.35 cm/s to 1.0 cm/s. Accordingly, a shorter residence time of 160 s can be obtained. The mass transfer coefficient they obtained under the new conditions was around 0.02 cm/s. The calculated conversion ratio in this case would be 14.78%, which is still quite low.

If the same residence time of 457 s were used, and the mass transfer coefficient could be kept as high as 0.02 cm/s, the conversion ratio would only reach 36.68%. This value represents a very poor reactor performance in practice.

5.3.1 General Behavior of Mass Transfer in a Continuous Reactor

Based on the fluid flow analysis in Chapter 4 and combined with the solution of the mass transfer equation, various operating parameters were tested to study the sensibility of system conversion ratio to each parameter, such as the gas volume flow rate, lower phase and upper phase heights, upper phase velocity, and the equilibrium partition ratio.

The standard operating parameters used in this study were as follows: a 4-nozzle or an 8-nozzle system, $Q = 4.52\,l/min$, $H_1 = 0.2\,m$, $H_2 = 0.05\,m$, $W = 0.2\,m$, $U_1 = 0.0035\,m/s$, $U_2 = -0.0065\,m/s$, and $\frac{\rho_1}{\rho_2} = 1.65$.

Figure 5-1 shows a 3-D concentration contour on selected planes where it is seen that the species concentration decreases as the fluid moves towards the exit. The concentration uniformity on each x-plane is largely achieved, although some degree of nonuniformity is apparent in the figure.

Calculated mean concentration profiles of the upper and lower phases along the reactor are shown in Figure 5-2 for a 4-nozzle system. The general behavior shown in this figure indicates more or less a linear dependence in the extraction of the species being considered for both phases. Also shown in the figure is the large difference in the slopes of the two curves, which is due to the large difference in volumes and densities of the two liquid phases. The conversion ratio predicted for this case was 23.35%. There are several "steps" that one can see from the concentration profile for the upper phase. A similar pattern would be shown on the concentration profile in the lower phase if the scale of the figure were changed. These steps coincide with the locations of the 4 plumes.

Figure 5-3 shows a contour of the mass transfer coefficient at the "two-phase" interface with the lower liquid phase flowing from right to left. The predicted mass transfer coefficient is in the range from 0 to 0.034 cm/s, with an average value of 0.0136 cm/s; this is about 3 times the value of 0.004 cm/s obtained from the measurements at UMR. The figure clearly indicates that the higher values of the mass transfer coefficient also correspond to the locations of the 4 nozzles.

5.3.2 Analysis of the Operating Parameters

Gas Volume Flow Rate Figure 5-4 illustrates the effect of gas volume flow rate on the system's conversion ratio. As seen in the figure, the conversion ratio increases with increasing gas volume flow rate. For the 4-nozzle system, the gas volume flow rate was increased from 4.52 l/min to 36.16 l/min and this resulted in an increase in the conversion ratio from 18.73% to 32.45%. Similarly, for the 8-nozzle system,

120
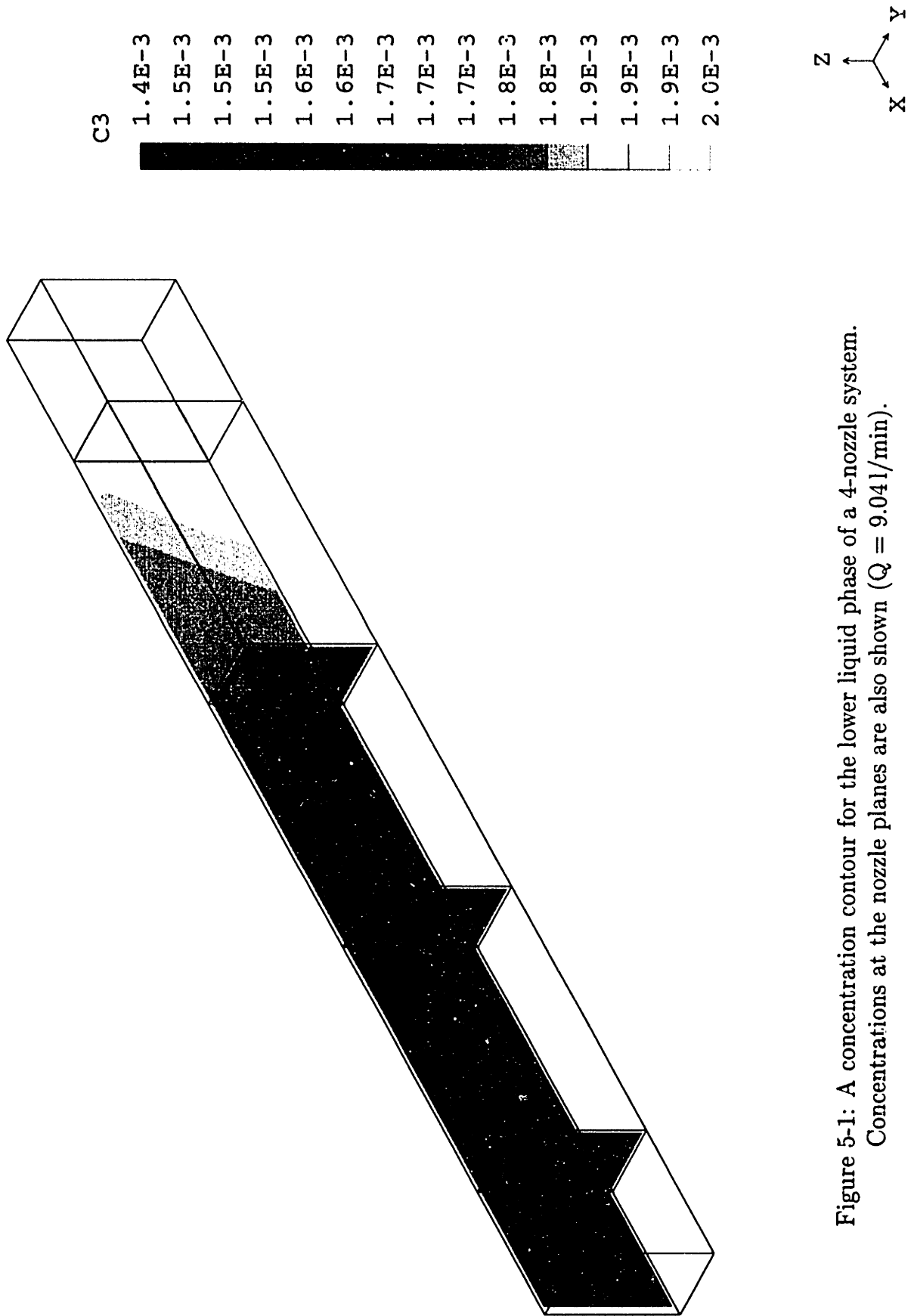
Figure 5-1: A concentration contour for the lower liquid phase of a 4-nozzle system. Concentrations at the nozzle planes are also shown (Q = 9.04 l/min).
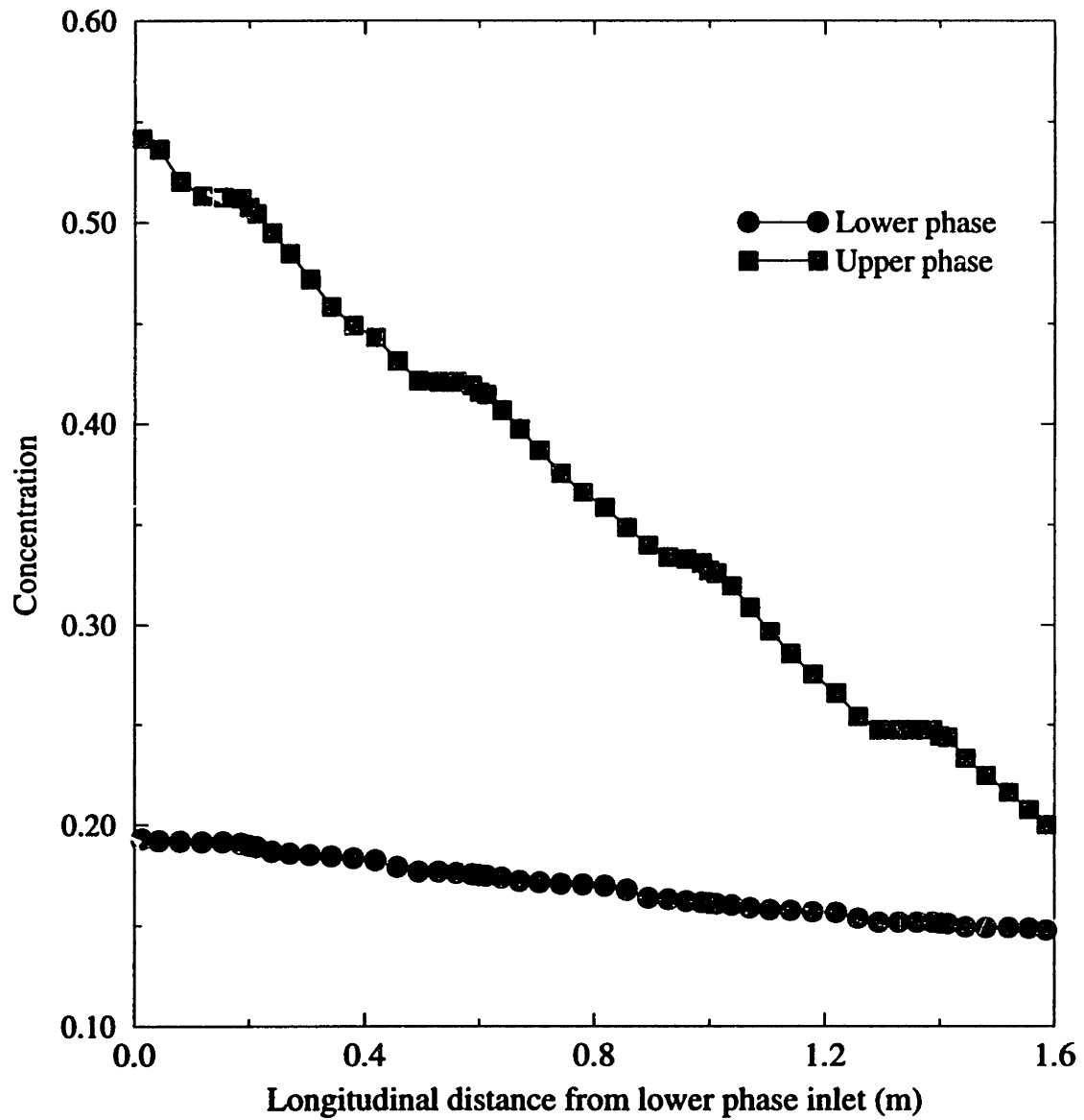
Figure 5-2: Predicted concentration profiles of both lower and upper liquid phases along the length of the reactor with 4 nozzles.

MASS

0.00
0.02
0.05
0.07
0.10
0.12
0.15
0.17
0.20
0.22
0.25
0.27
0.29
0.32
0.34
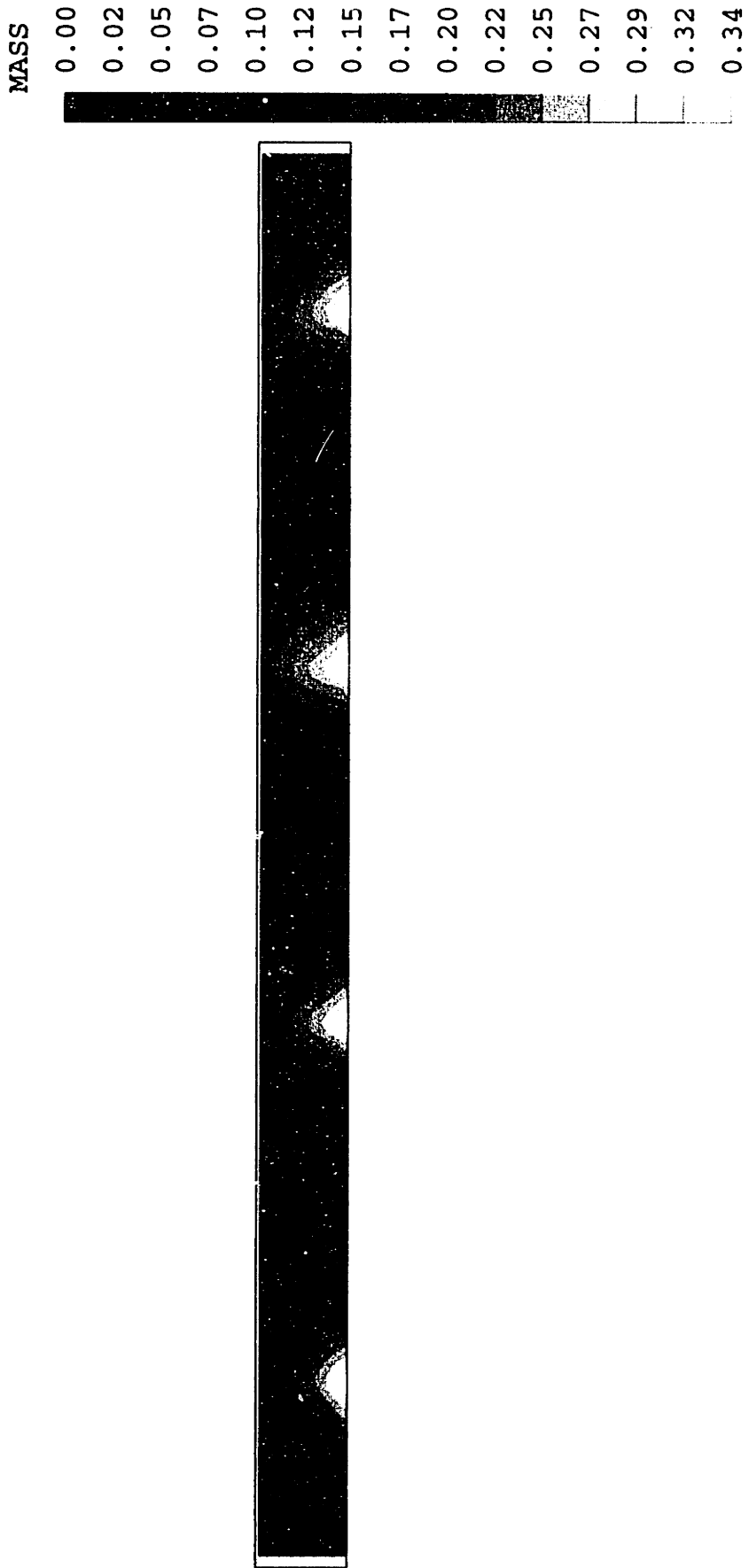
Figure 5-3: A contour showing the mass transfer coefficient at the "two-phase" interface ($\times 10^{-3}$ m/s, only a half of the reactor is shown because of the symmetry plane).

the resulting change of conversion ratio was from 23.36% to 39.71% under the same gas flow rate changes. These results indicate that, for the range of values considered in these calculations, the resulting conversion ratio is still quite poor for practical purposes.

Figure 5-5 shows the effect of the gas volume flow rate on the overall mass transfer coefficient calculated at the "two-phase" interface. The averaged mass transfer coefficient at the interface was increased from 1.06×10^{-2} to 2.17×10^{-2} cm/s (only a factor of two), when the gas volume flow rate increased from 4.52 l/min to 36.16 l/min. The correlation from the figure is best represented by:

$$k \propto Q^{0.26 \sim 0.34} \tag{5.9}$$

Lower Liquid Phase Height Figure 5-6 shows the predicted reactor conversion ratio as a function of the lower liquid phase height. It is seen that as the height of lower phase increases, the conversion ratio decreases. It is noted, however, that the volume is not the same for each case, which results in a difference in the throughput level.

Figure 5-7 shows the predicted mass transfer coefficients at the two phase boundary as a function of the lower liquid phase height. It is interesting to see that an opposite trend is shown between the 4-nozzle and the 8-nozzle systems, although the difference in the actual mass transfer coefficient values is quite small. It can be suggested that the difference in trends between the two curves may be due to the interactions between plumes which are more likely to occur in the 8-nozzle system. These interactions could change the local distribution of the turbulence kinetic energy dissipation ϵ, which would result in a lower mass transfer coefficient k at the interface.

Lower Liquid Phase Flow Rate The effect of the horizontal flow rate of the lower liquid phase on the reactor performance was also investigated, although the tested cases are not comparable to each other since the corresponding production levels are
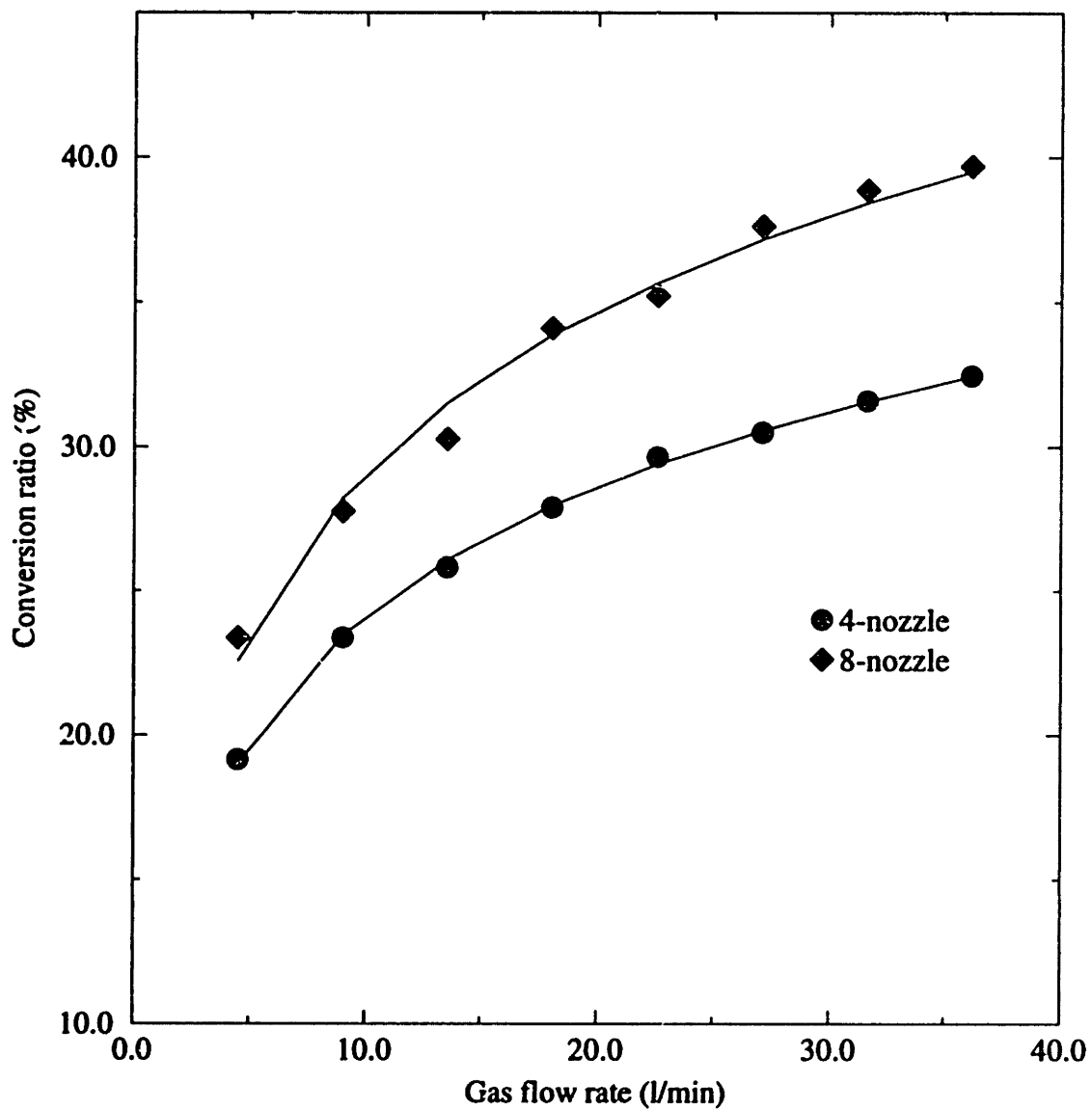
Figure 5-4: Predicted conversion ratio as a function of the gas volume flow rate.
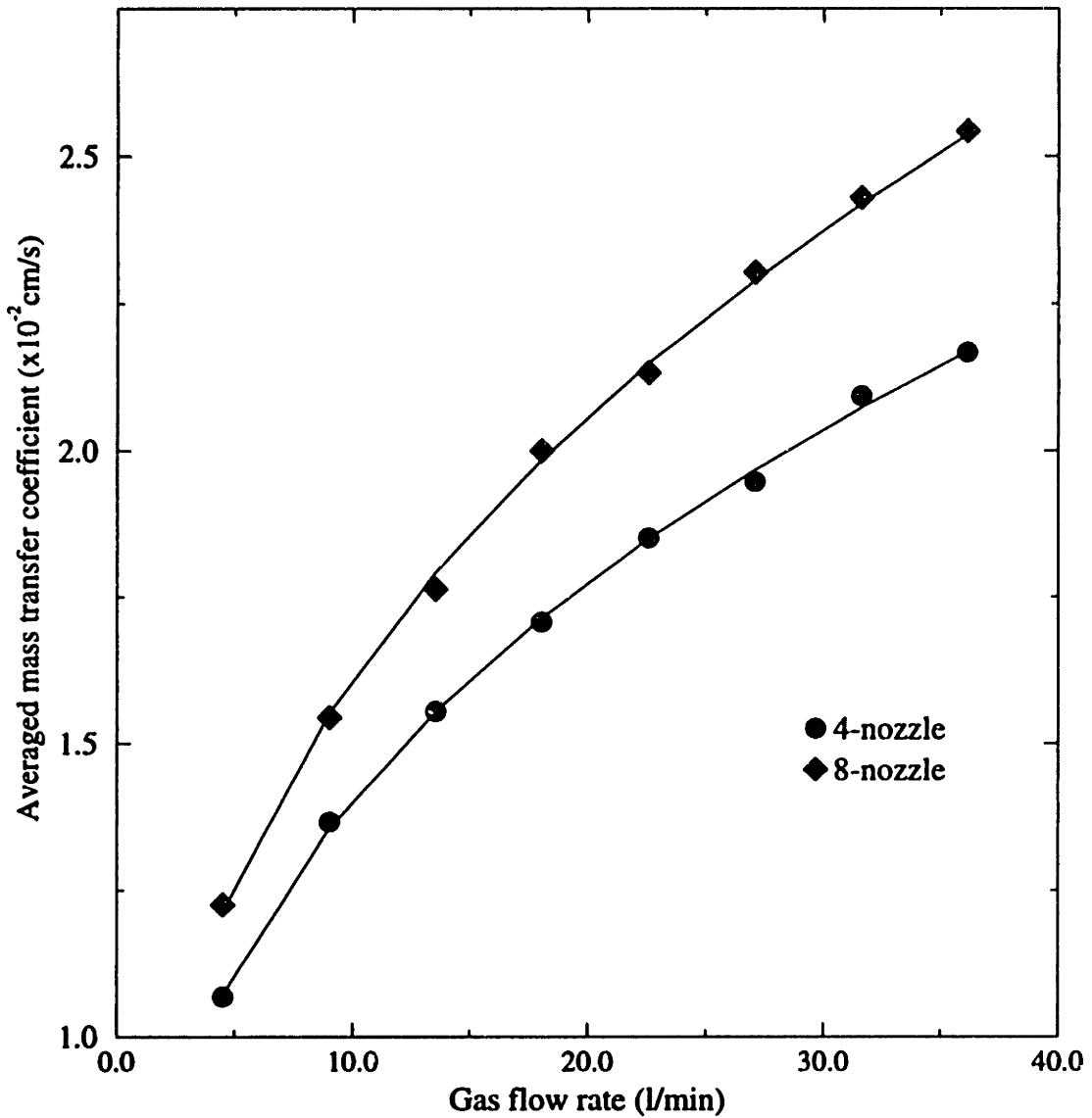
Figure 5-5: Predicted mass transfer coefficient at the "two-phase" interface as a function of the gas flow rate.
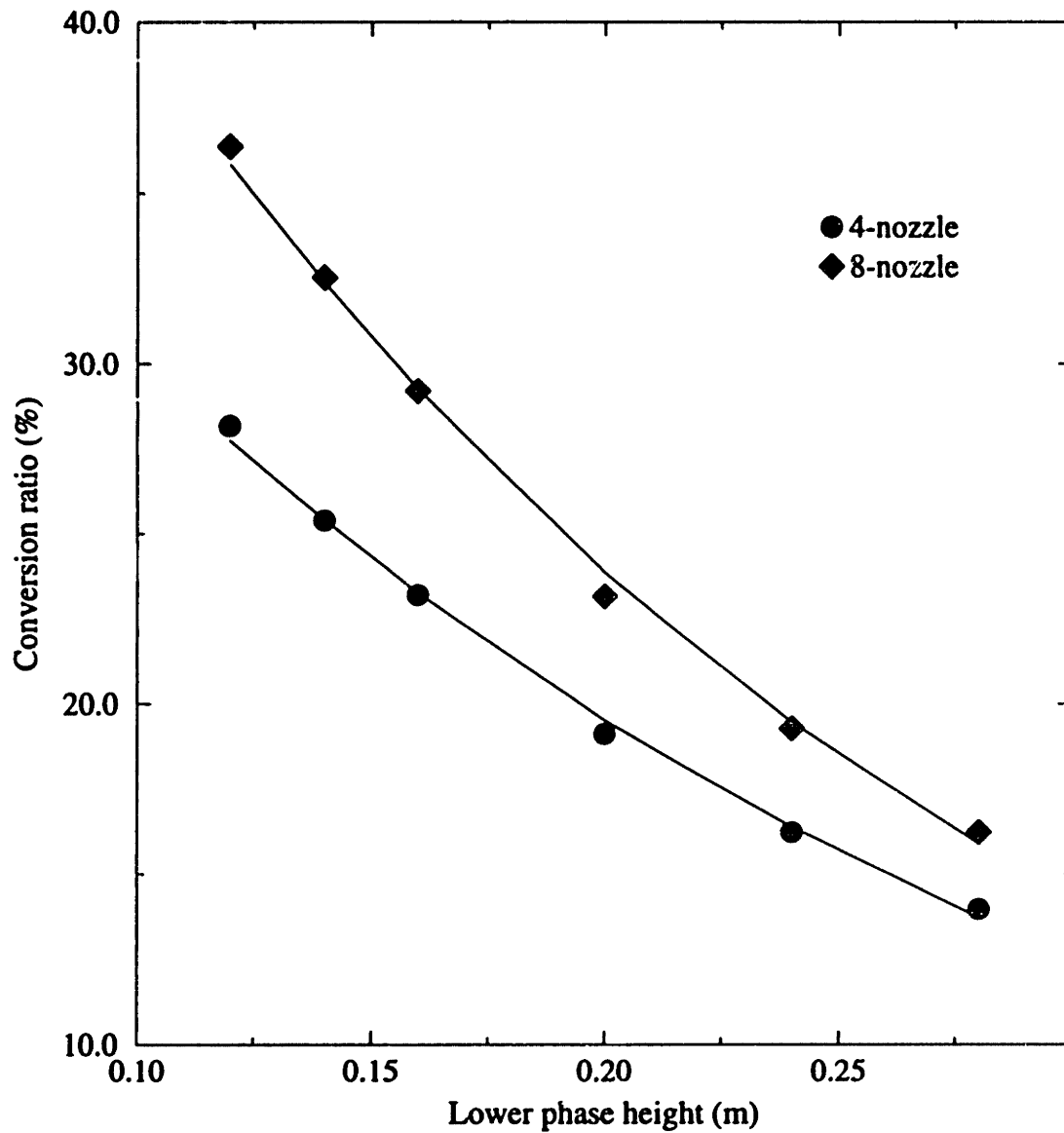
Figure 5-6: Predicted reactor conversion ratio as a function of the lower liquid phase height.
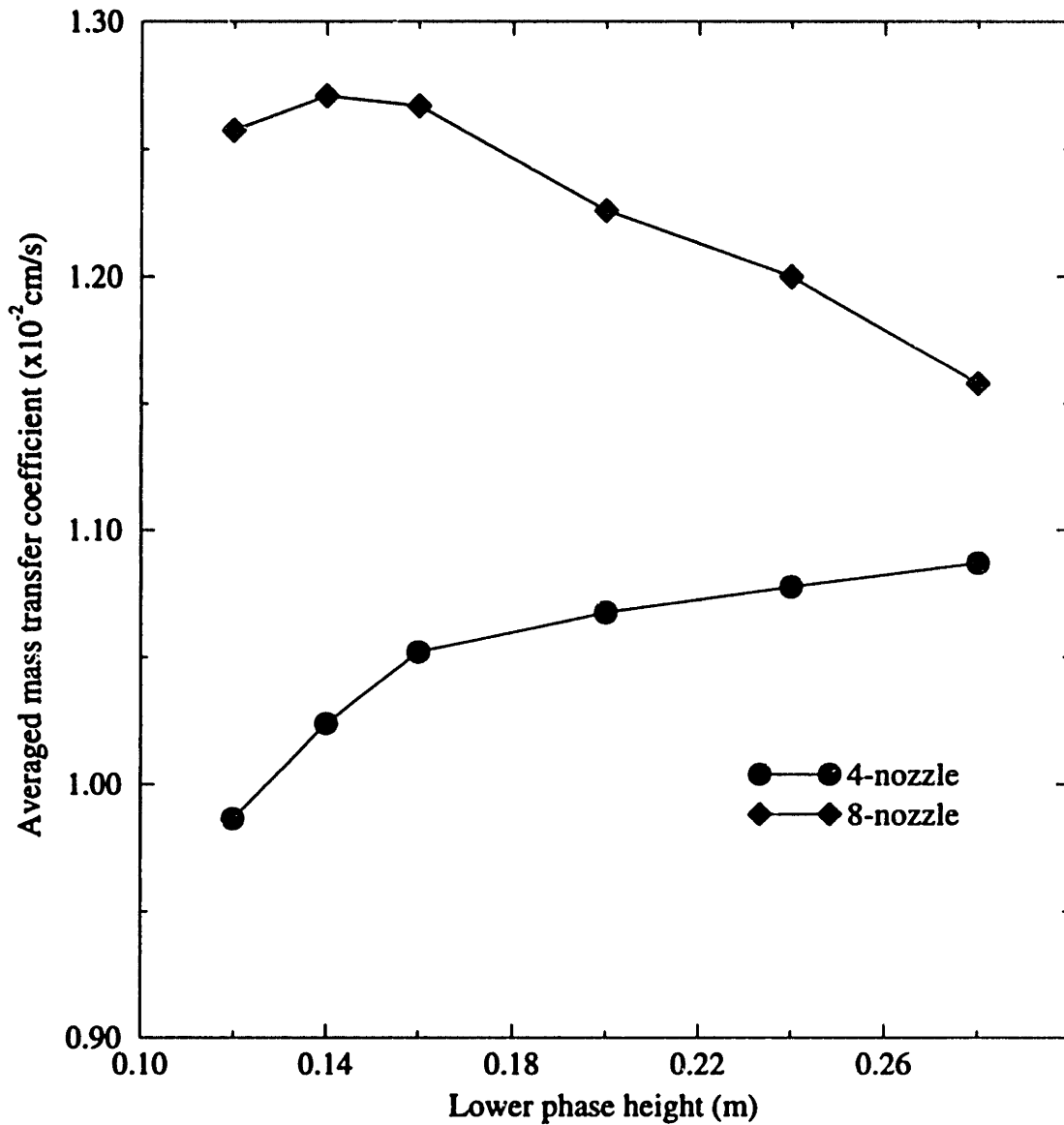
Figure 5-7: Predicted average mass transfer coefficient at the "two-phase" boundary as a function of the lower liquid phase height.

different. The calculated conversion ratios of the system for different horizontal liquid velocities are shown in Figure 5-9, where it is seen that the conversion ratio decreases as the horizontal liquid velocity increases, apparently because of the decrease of the average residence time of the liquid in the reactor.

By examining the averaged mass transfer coefficients calculated at the "two-phase" interface, which are shown in Figure 5-8, the above conclusion is confirmed. The changes of the mass transfer coefficients are negligible as the horizontal liquid flow velocity is increased, in the range from 0.15 cm/s to 0.7 cm/s.

Bubbler Separation The effect of the bubbler separation on the reactor conversion ratio is shown in Figure 5-10, where it is seen that the conversion ratio increases as the distance between nozzles decreases, while the other operating parameters are kept the same.

Figure 5-11 shows how the distance between nozzles affects the average mass transfer coefficient at the two liquid interface. It is seen that the mass transfer coefficient increases as the bubbler separation decreases (i.e., more nozzles). Therefore, it is beneficial to the reactor performance to increase the number of nozzles.

This point is also justified in terms of the difference in the mass transfer coefficient distribution along the reactor length as shown in Figure 5-12. As shown in this figure, the variation of the average mass transfer coefficient is more uniform (i.e., smaller difference between peak and trough values) when the number of nozzles is increased, which also results in a higher mean value of the mass transfer coefficient.

Effect from the Upper Liquid Phase A minimal effect was shown from the change of the upper liquid phase height. Analysis of the results suggests that as the upper phase height increases from 0.02 m to 0.2 m, the conversion ratio only increases about 1%. The effect of the upper phase height on the interphase mass transfer coefficient was not considered in this study.

There are two limiting cases concerning the effect of the upper phase velocity:

1. To assume that the upper phase moves with an infinite velocity in the horizontal
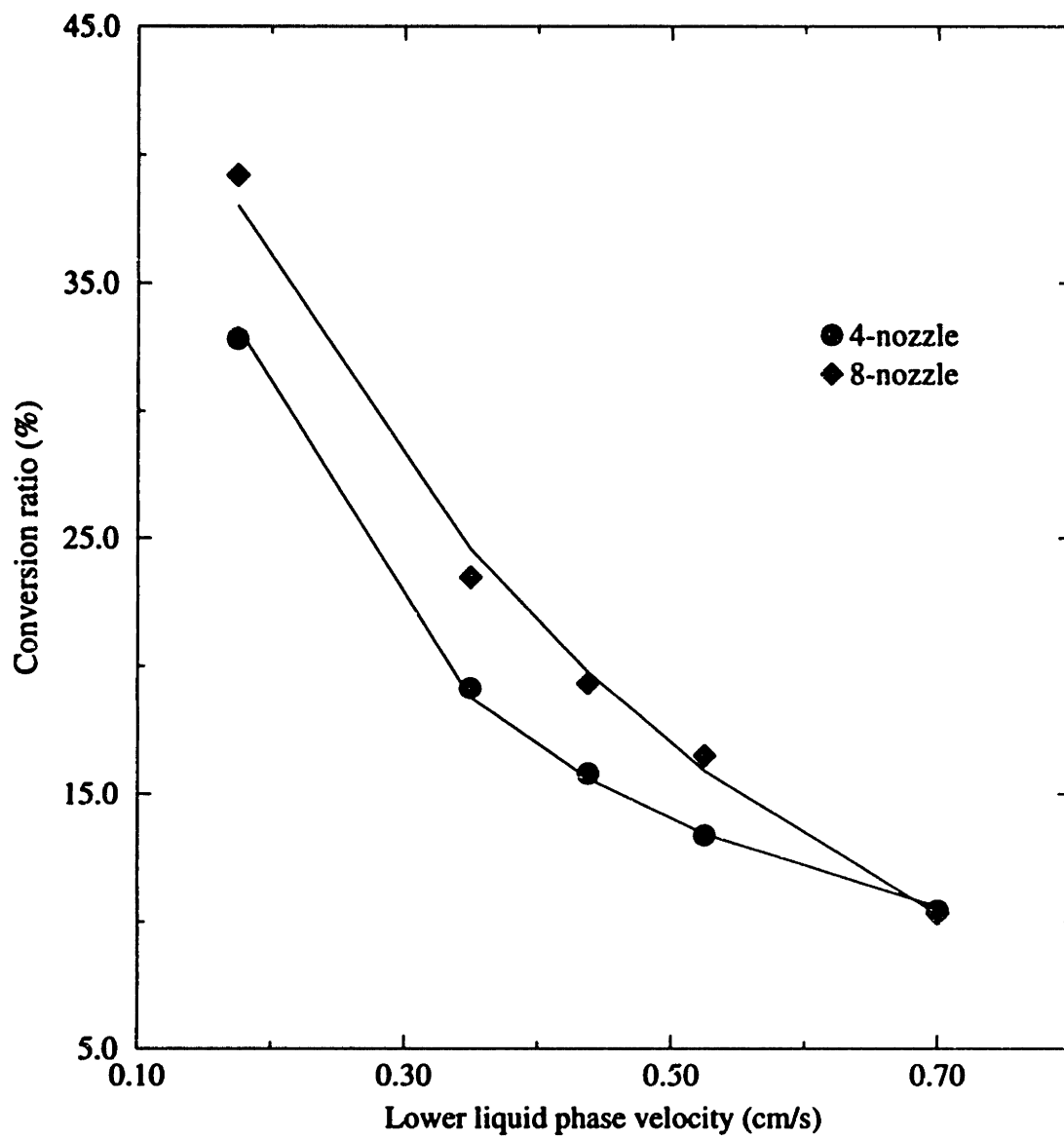
Figure 5-8: Predicted conversion ratio as a function of the lower liquid phase flow velocity.
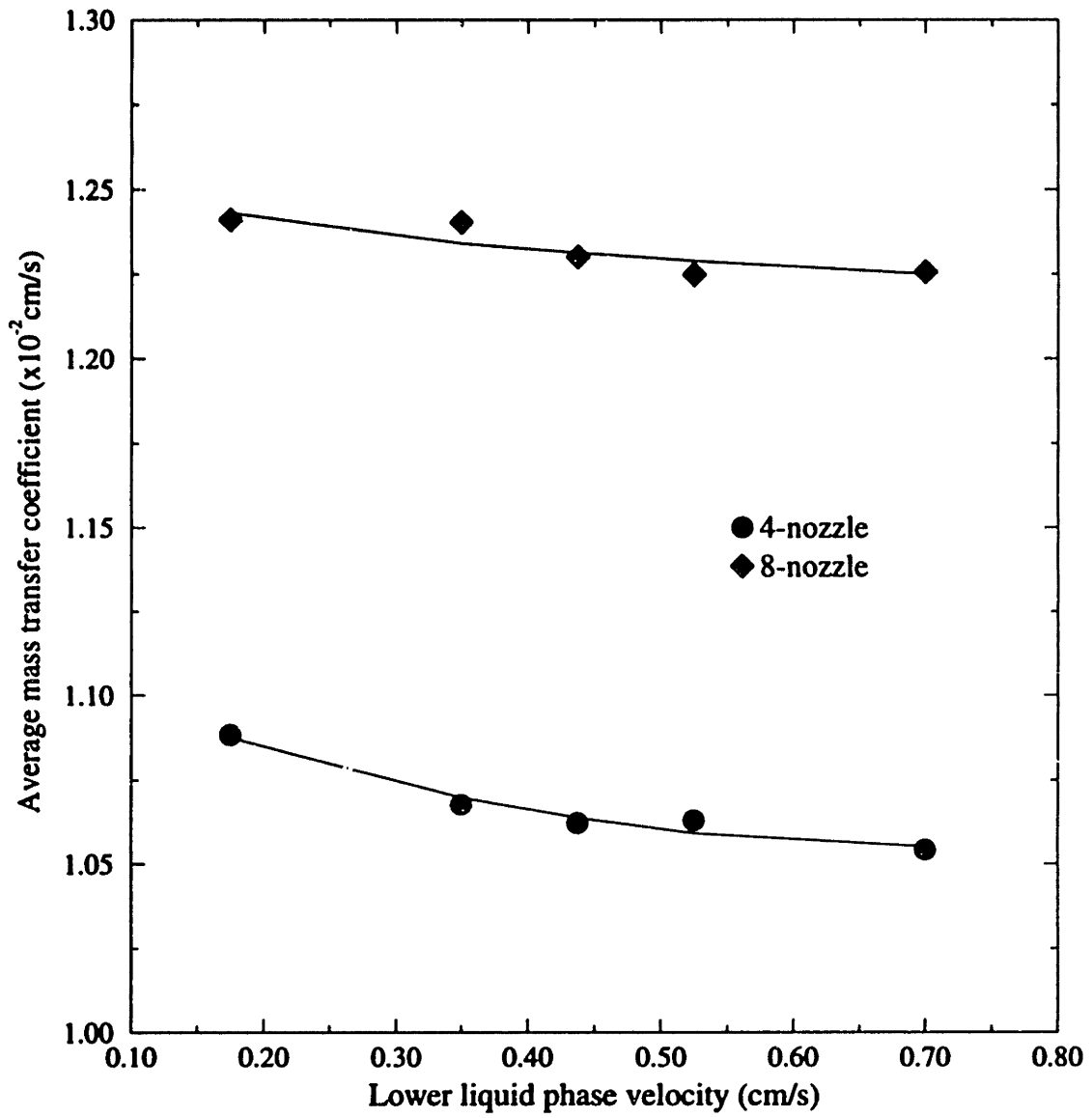
Figure 5-9: Predicted average mass transfer coefficient at the "two-phase" boundary as a function of the lower liquid phase flow velocity.
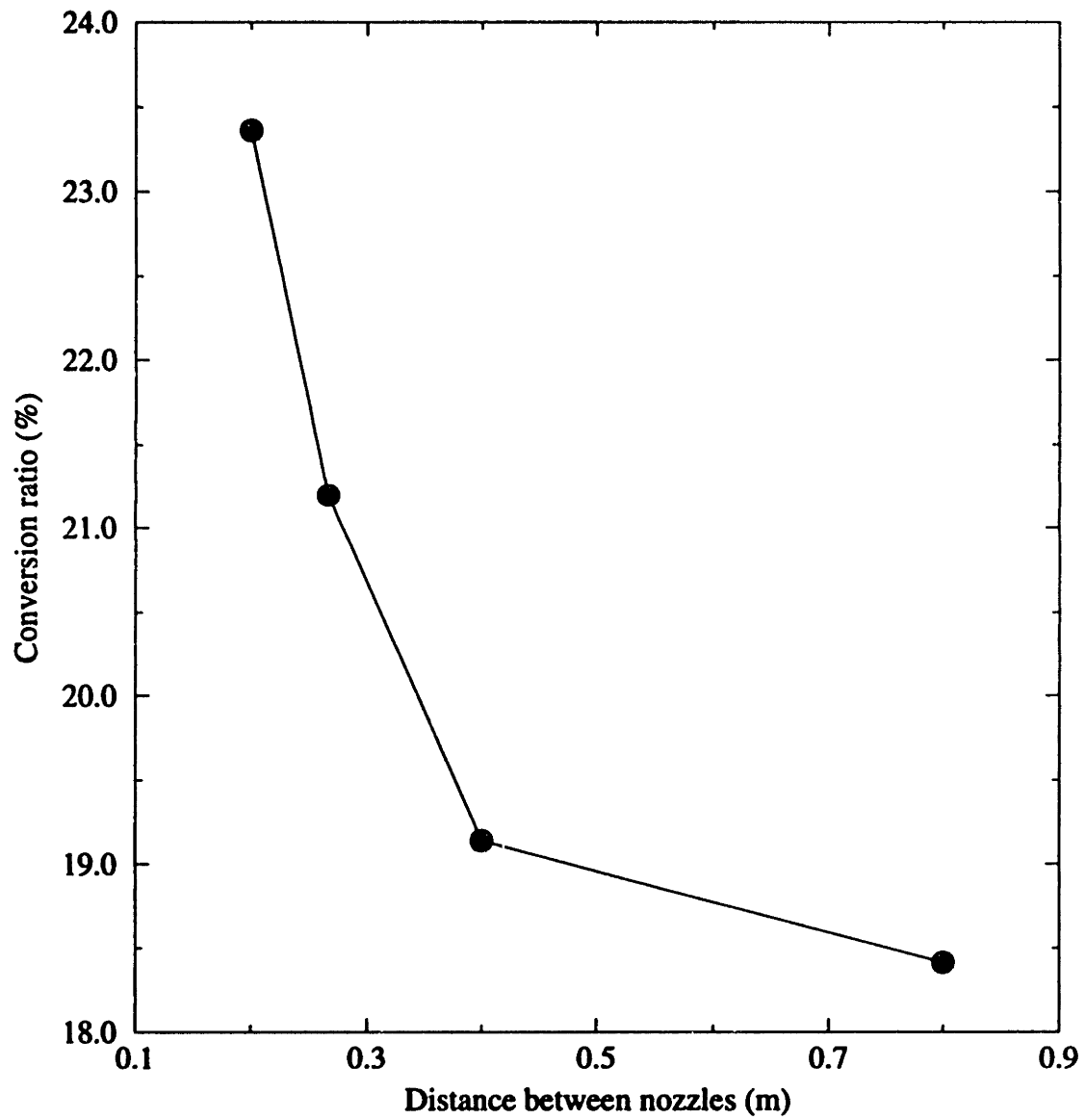
Figure 5-10: Bubbler separation effect on the conversion ratio of the reactor.
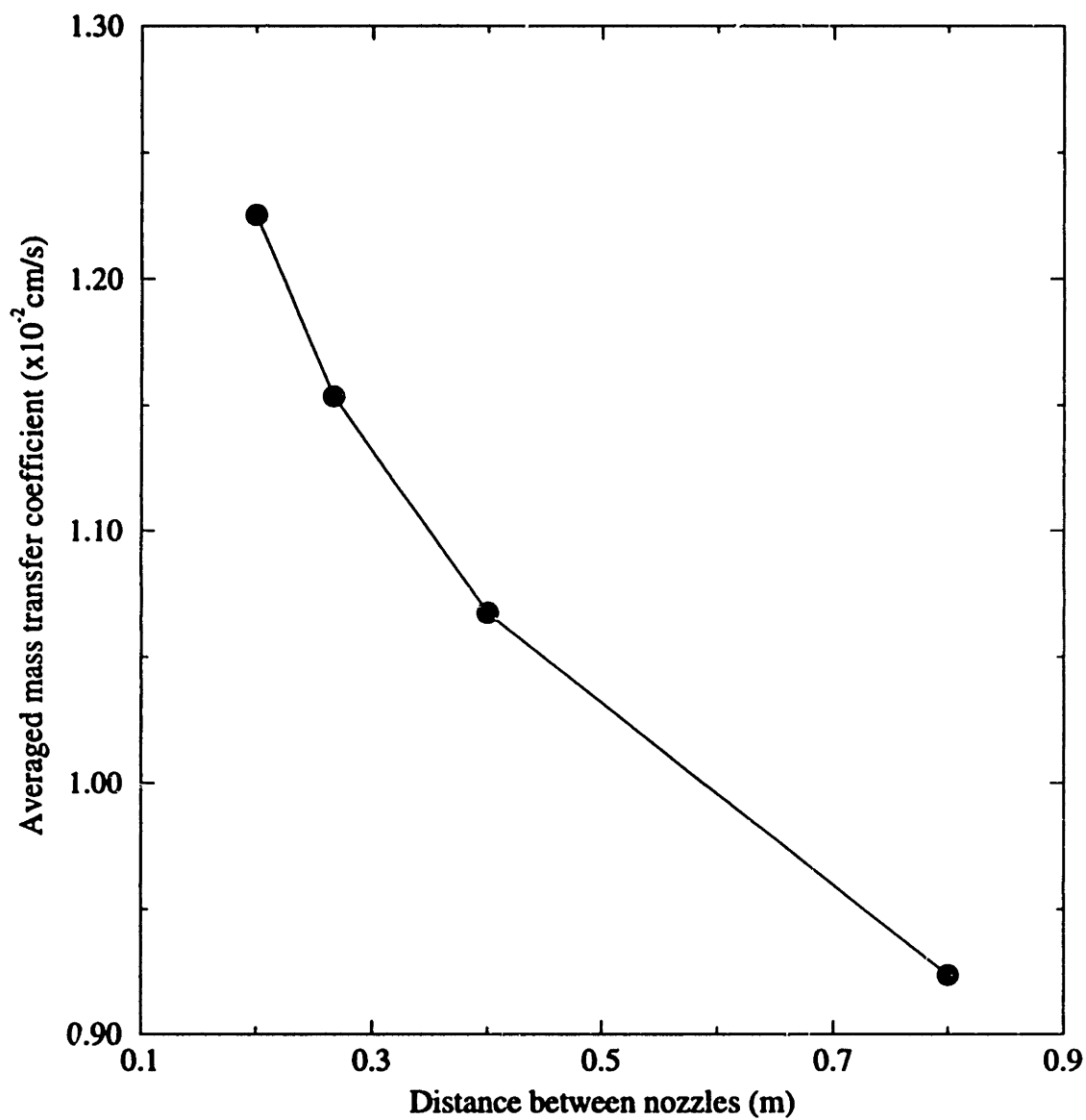
Figure 5-11: Bubbler separation effect on the averaged mass transfer coefficient at the "two-phase" interface.
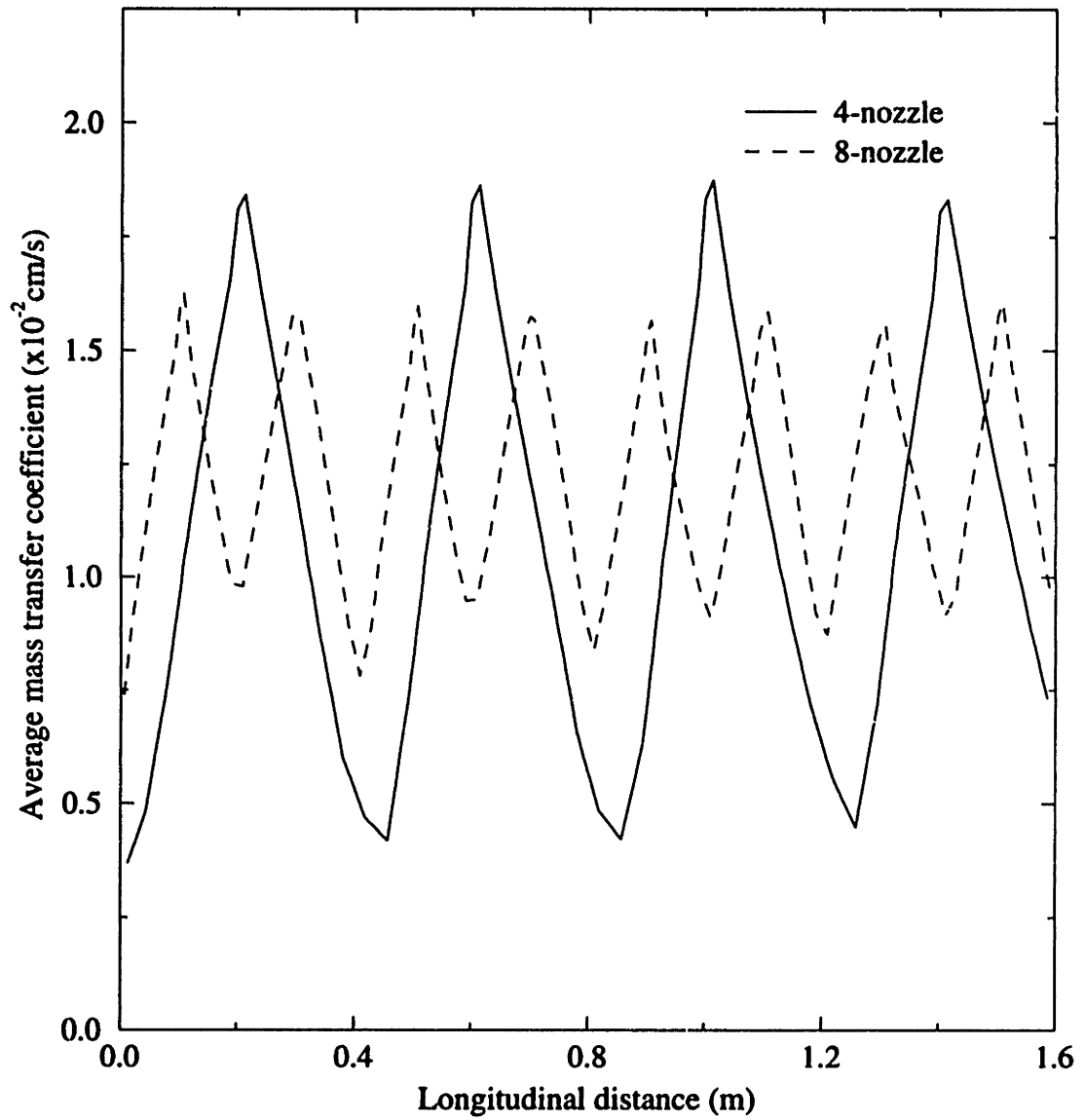
Figure 5-12: Bubbler separation effect on the averaged mass transfer coefficient along the reactor length.

direction, which would result in a constant upper phase concentration equal to the inlet value. The driving force in this case would be the maximum.

2. To assume that the upper phase is stagnant, in which case the upper phase would reach the highest concentration level (i.e., possibly the saturation level). The driving force in this case would be minimum. This is of course a hypothetical case, since in reality, if the upper phase is stagnant, the problem will become transient.

The predicted minimum and maximum conversion ratios for the two limiting cases are 23.36% and 23.50%, respectively. As shown by these values, there is essentially no effect from the upper phase flow rate on the conversion ratio. This can be explained in the following way: under the assumptions used to incorporate the effect of the liquid upper phase, it was considered that the main resistance to mass transfer was from the lower phase and only the concentration of the upper phase plays a role in the calculation as a boundary condition. In addition, the changing concentration of the upper phase due to flow rate has a minimal effect on the concentration gradient between the two liquid phases (i.e., the driving force used to consider mass transfer between the two liquid phases).

In a similar way, there is only a minimal effect from the equilibrium partition ratio between the two phases, since the upper liquid phase is far from saturation. Therefore, the effect of different equilibrium partition ratios on the driving force between the "two phases" is also minimal. A test suggested that an increase of the equilibrium partition ratio from 200 to 500 only results in less than a 0.2% increase in the conversion ratio.

5.3.3 Baffles

Continuous reactors with baffles were investigated in order to explore alternative ways to modify the flow patterns in the system by providing additional partitions between gas plumes in an attempt to decrease the degree of longitudinal mixing and increase the conversion ratio of the reactor.

Table 5.3: Effect of baffles on system behavior

	No baffles	Bottom	Side	Center
Dispersion number	0.066	0.04	0.047	0.062
Mass transfer coefficient $(\times 10^{-4} m/s)$	1.0677	1.0148	0.9979	0.9646
Conversion ratio (%)	19.14	18.08	19.83	17.54

Systems with different baffle configurations were tested to investigate their effect on the system's longitudinal mixing behavior and the resulting conversion ratio. The baffle configurations that were tested include center baffles, side baffles and bottom baffles. A schematic showing the different baffle configurations is given in Figure 5-13, where three baffles are placed in between the four nozzles of the reactor. The simulation results are presented in Table 5.3 from which it can be concluded that there is no apparent baffle configuration which can be considered as a way of increasing the reactor conversion ratio. In more detail, it was found that both side baffles and bottom baffles decrease longitudinal mixing significantly, while the center baffles only decrease longitudinal mixing slightly. In contrast, the mass transfer coefficients decreased with different baffle configurations, which resulted in almost no change in the system conversion ratio.

5.4   Discussion

In this section, we will discuss the mass transfer coefficient model used in the calculations presented in this chapter and its implications on the conversion ratios predicted.

In the mass transfer coefficient model that was adopted, the turbulence energy dissipation rate ϵ is a variable that relates to the fluid flow and turbulence characteristics in the lower liquid phase. This was obtained by solving the Navier-Stokes and the corresponding turbulence model equations as explained in Chapter 2. The turbulence energy dissipation rate ϵ, can also be estimated from the overall energy balance of the system. A comparison of values for ϵ, and the resulting mass transfer coefficients k_o, calculated from the two methods would be helpful to establish some confidence in the mass transfer model employed in the calculation.
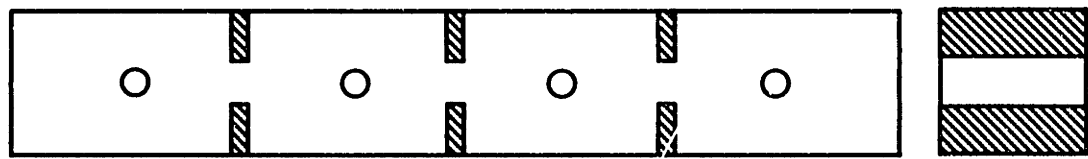
(a) Side baffles
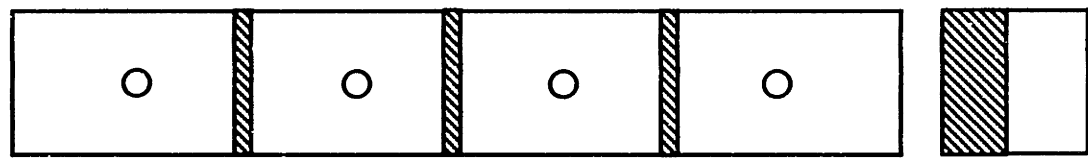
(b) Bottom baffles
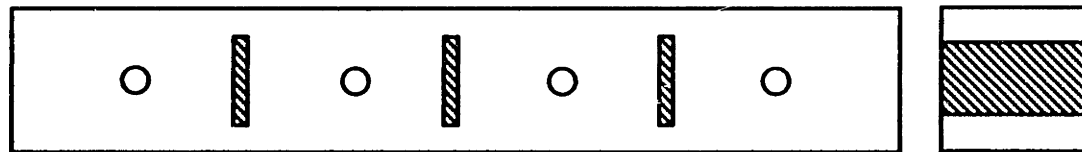
(c) Center baffles

Figure 5-13: A schematic of different baffle configurations in a 4-nozzle system.

137

Table 5.4: Various expressions for potential energy input rate to the gas stirred system (Units are in SI system except otherwise noted).

Investigators	Expressions
Nakanishi et al. [105]	$\epsilon = \frac{0.028 Q T_l}{W} log(1 + \frac{H}{148})$**
Themelis and Stapurewicz	$\epsilon = \frac{742 Q T_l}{W} ln(1 + \frac{H}{10.34})$
Mazumdar and Guthrie [108]	$\epsilon = \frac{\rho_l g Q H}{\rho_l \pi R^2 H}$
Sinha and McNallan [106]	$\epsilon = \frac{854 Q T_l}{W} log(1 + \frac{\rho_l g H}{P_a})$
Krishnamurthy et al. [109]	$\epsilon = \frac{4 Q P_a T_l}{298.2 \pi D^2 H} ln(1 + \frac{\rho_l g H}{P_a})$

**H(cm); Q (l/min); W(tons)

The expressions commonly used to estimate the potential energy input rate ϵ have been summarized in a review paper by Mazumdar and Guthrie [3] and are reproduced in Table 5.4. They presented different correlations that have been suggested for various geometrical arrangements and ranges in process conditions. Among those correlations, two are limited to cylindrical reactors while the other three can be used to estimate the potential energy input rate for a channel-type reactor.

Assuming all the energy input is dissipated into the flow system, the values of ϵ obtained from the correlations are equal to the turbulence kinetic energy dissipation rate. The calculated turbulence kinetic energy dissipation rate was plugged into equation (5.5) to estimate the mass transfer coefficients. The results are compared in Figure 5-14, together with the results presented earlier in this chapter. One can see from the figure a good agreement in the trends between the results of the mathematical model and the data obtained from the correlations. The difference in the actual values is within a factor of 2-3 (with the values of the mathematical model being smaller). In contrast, as it was mentioned earlier, the mass transfer coefficient from simulations are higher the values obtained at UMR where values of 0.004 cm/s and 0.02 cm/s were suggested. This comparison indicates that the values estimated for the mass transfer coefficient in our three-dimensional calculations are conservative with respect to other correlations available. However, the main outcome of using our model is that the results for the conversion ratio are optimistic in comparison to the experimental system being studied.

138
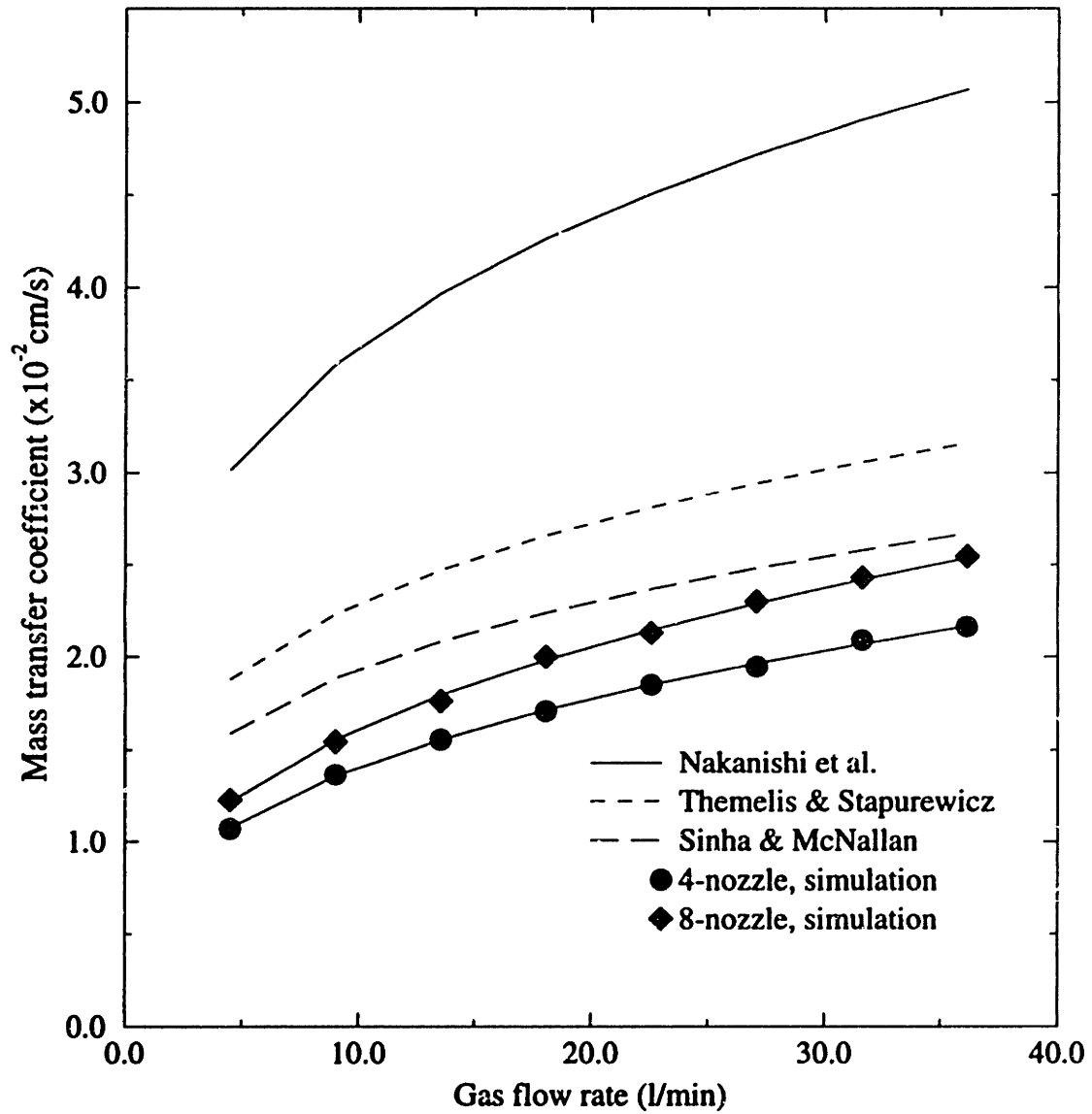
Figure 5-14: A comparison of predicted mass transfer coefficient with the data from different correlations of calculating ϵ.

5.5 Summary

A comprehensive liquid-liquid mass transfer analysis was carried out in this chapter to study the feasibility of a channel-type continuous metallurgical reactor. Based on the assumption that the mass transfer of species in the lower liquid phase is the controlling mechanism in the reactor, a mass conservation equation for species was solved to explore the mass transfer rate at the "two-phase" interface. Parametric studies were carried out to study the relative sensitivity of each operating parameter. The important findings from the analysis in this chapter are summarized as follows:

- The conversion ratios obtained using the existing design parameters are generally low, suggesting the need for a longer system together with changes in other parameters.

- An 8-nozzle system is selected over a 4-nozzle system (other things being equal) both in terms of increasing the interphase mass transfer coefficient and the reactor conversion ratio.

- Increasing the gas flow rate is generally beneficial to enhance interphase mass transfer (although this also has the effect of increasing the longitudinal mixing). The curve fitting from the modeling results shows that $k_o \propto Q^{0.26 \sim 0.34}$.

- A lower reactor aspect ratio is good for interphase mass transfer, although the throughput is also lower.

- A small bubbler separation is needed both for a higher conversion ratio and a larger mass transfer coefficient at the interface (under the same operating conditions).

- The height of the upper liquid phase, the equilibrium partition ratio and the upper phase velocity have negligible effect on the reactor conversion ratio, under the conditions used in the physical model setup, because the upper phase concentration is still far from saturation when it leaves the reactor and it was

140

considered in the model that the main resistance to mass transfer was within the lower liquid phase.

- The use of baffles does decrease the longitudinal dispersion in the reactor, but the negative effect it has on the mass transfer coefficient makes it an unpromising opportunity.

Chapter 6

Discussion and Conclusions

A mathematical model has been developed to represent a two-phase (liquid-gas) gas-stirred flow system. The verification of the model has been carried out by comparing the predictions with both experimental measurements from the literature and results obtained at the University of Missouri-Rolla (UMR). The two-phase model was adapted to take into account a second liquid phase by making some approximations that were implemented as an upper surface boundary condition. A great deal of "numerical experiments" were conducted to analyze the system's longitudinal mixing behavior and conversion ratios, under the prevalent operating conditions.

A discussion on the main implications of this work is presented in this chapter, together with a summary of the most important findings.

6.1 Discussion

An ideal counter-current launder reactor should be a system in which each of the counter-current phases approaches plug flow in the longitudinal direction (i.e., $Pe^{-1} = D_e/uL \ll 1$), while there is a complete mixing in the vertical direction and rapid mass transfer between the phases (very high mass transfer coefficient and concentration gradients). Low values of Pe^{-1} are required to avoid longitudinal dispersion in order to keep high concentration gradients between the counter-current phases.

Clearly this ideal situation cannot be realized, but the extent to which one may

approximate it by the judicious selection of the system geometry and operating conditions represented the main focus of this investigation.

The results of the fluid flow analysis (Chapter 4) can be combined with those including mass transfer behavior (Chapter 5) to discuss the main implications of this study in an attempt to provide an overall picture of the system behavior. This can be done by summarizing all the results in terms of two dimensionless groups: the inverse Peclet number (D_e/uL) and the Damköhler number, defined as $kA\rho/\dot{m}$, where k is the effective rate constant or mass transfer coefficient; A represents the area available for reaction (i.e., interface); ρ is the density of the liquid and $\dot{m}$ is the horizontal mass flow rate of the liquid.

For a given level of longitudinal dispersion (determined by the inverse Peclet number), the Damköhler number represents the important factor in determining the level of refining or mass exchanged between the phases. This number defines the relative importance of the rate of chemical reaction or mass transfer across the interface with respect to the bulk mass flow rate.

A useful parameter for assessing the effectiveness of a channel counter-current reactor can be obtained by taking the ratio of the above two dimensionless numbers, which, for the purpose of comparison, we can name it the performance parameter (i.e., kL^2/D_eH, where H is the height of the lower liquid phase). High values of this ratio will then indicate good reactor performance (i.e., maximum rates of mass transfer with minimum longitudinal dispersion).

Figure 6-1 shows a plot of the conversion ratio as a function of the above dimensionless performance parameter, in which most of the results from the previous two chapters are included. By inspection of this plot, the following comments can be made:

- For the range of conditions employed in the calculations (those limited by the physical model set up at UMR), the plot clearly indicates the overall trends caused by the different process parameters by the individual curves and given by the positive slopes which indicate that high conversion ratios are provided by high gas flow rates, low liquid flow rate, small vessel height and small nozzle

143
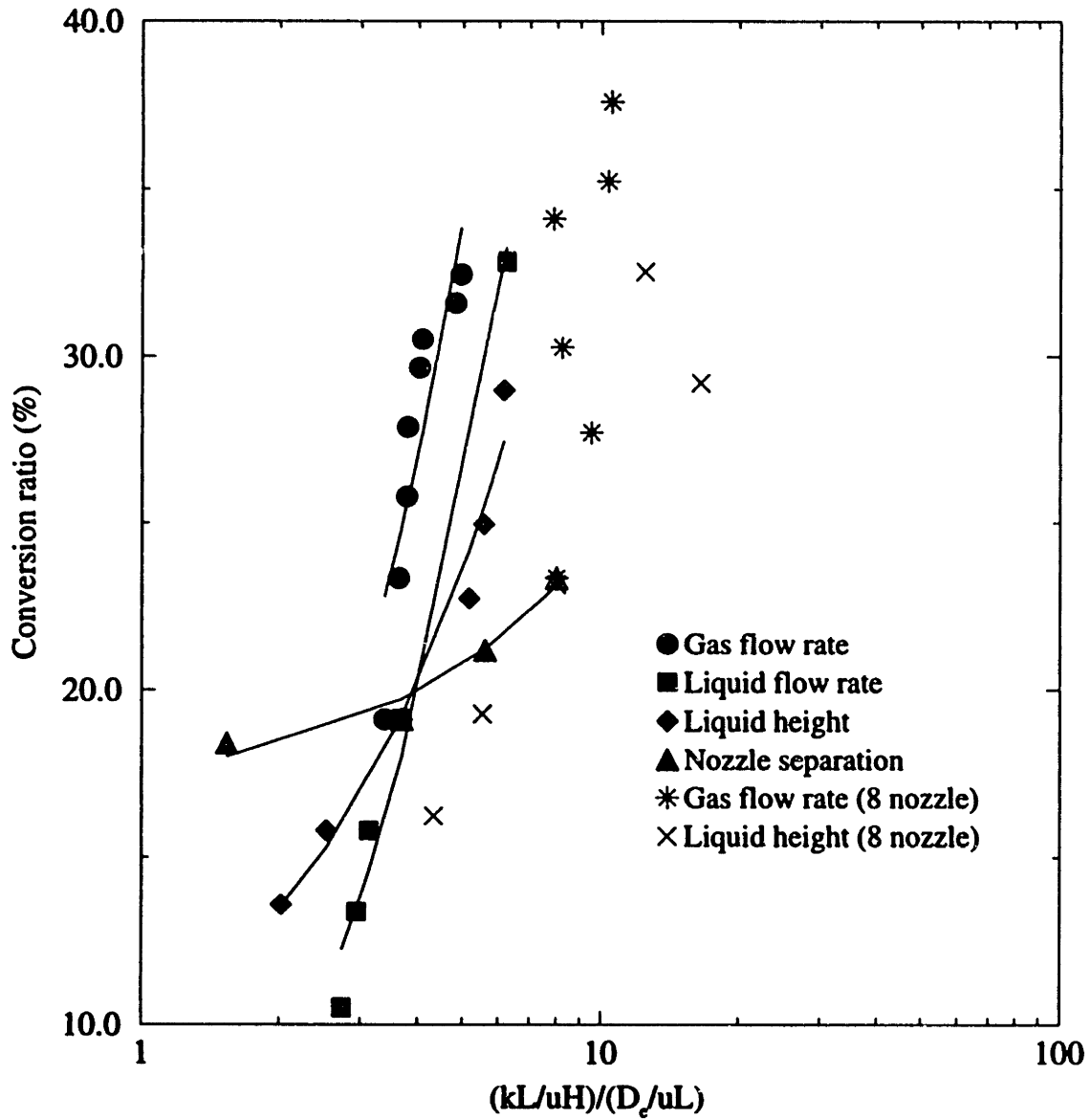
Figure 6-1: A summary of conversion ratios under different operating conditions.

separation.

- The maximum levels of conversion only reach about 40%, indicating a rather poor performance, for the current experimental conditions.

- The key process parameters that directly influence the conversion ratio are the gas flow rate and the separation between nozzles. There are, nevertheless, physical limits imposed up to how much these parameters can be modified. For example, excessive flow rates will eventually change the operating regimes into a splashing and foaming mode, which can be undesirable.

- The effect of other parameters such as the reactor aspect ratio (H/W) and liquid flow rate can improve the conversion ratio but also have a negative effect on the production levels, which may be unacceptable from a practical point of view.

- The plot clearly indicates the overall trends caused by the different process parameters by the individual curves.

As far as alternative ways to improve the reactor conversion ratio, the only possibility that appears feasible is by increasing the length of the system. The main implication in doing this would be having a very long system.

Table 6.1 shows a comparison of the performance for different channel-type reactor designs, including the predictions regarding how long the reactors have to be for a desirable conversion ratio. The contents of each column in the table are explained as follows: The third column in the table presents the parameters of the current physical model setup at UMR, the experimental measured mass transfer coefficient and the conversion ratio calculated using formula (5.8). The fourth column represents the predictions from the mathematical model, using the same operating parameters as in column three. The fifth column is an optimized design based on the experience from mathematical simulations carried out in this work. The criterion used to seek the optimal operating conditions includes maximizing the conversion ratio for a minimal reactor length, while keeping the reactor production level a constant.

Table 6.1: Evaluation of different designs of physical mode setups.

Variables	Symbols	Physical model (UMR)	Math model I (Based on UMR)	Math model II (MIT)
	H_1	0.2	0.2	0.21
Size (m)	W	0.2	0.2	0.265
	L	1.6	1.6	1.6
	H_2	0.05	0.05	0.05
Velocity (m/s)	U_1 (lower)	0.0035	0.0035	0.0025
	U_2 (upper)	-0.0065	-0.0065	-0.0065
Residence time (s)	t_R	457.14	457.14	640.0
No. of nozzles	n	8	8	10
Gas flow rate (l/min)	Q (N_2)	40	40	40
Production	(tons/hr)	5.04E-01	5.04E-01	5.01E-01
Longitudinal diffusivity	D_e (m^2/s)	7.E-04	5.6E-04	1.34E-04
Mass transfer coefficient	k_o (m/s)	2E-4	2.63E-04	3.59E-04
Conversion ratio using (5.9)	(%)	36.69%	45.16%	66.52%
Conversion ratio from math model	(%)	—	41%	50%
Length for 90% conversion	(m)	8.06	6.13	3.37
Length for 99% conversion	(m)	16.12	12.26	6.73

From the experience developed from the numerical simulations and the analysis of the effect of the various operating parameters, an optimized 10-nozzle system was suggested which resulted in a conversion ratio of 50% .

The results shown in the table suggest that a length-to-height ratio of about 20 is required for a conversion ratio higher than 90%. By extrapolating the results, it can be suggested that a conversion ratio of 99% can be obtained by almost doubling the length just mentioned.

6.2 Conclusions

The important findings from this study can be summarized as follows:

Cylindrical Reactors A cylindrical reactor with either a central or an eccentric gas injection at the bottom was investigated. Mixing time was used as the criterion to evaluate the performance of this kind of reactor in terms of the degree of homogenization. The conclusions that can be drawn from this part of the work are:

1. Very good general agreement was obtained between the model predictions and two independent sets of experimental results.

2. Increasing the gas flow rate injected into the system generally decreases the mixing time. A correlation from the simulations suggested the relationship: $t_m \propto Q^{0.5}$.

3. The optimal tracer addition location for an axisymmetric system was found to be in the region just outside the gas plume ($\frac{1}{3}$R) and the upper half of the reactor, as suggested by the simulations under two very different gas flow rates.

4. A reactor having an eccentric gas injection has a shorter mixing time than a centric injected one, probably due to the enhanced horizontal recirculation, which is absent in the axisymmetric system. The optimal nozzle location to obtain a minimal mixing time was found to be at about $\frac{1}{5}$R on the radius. A 43% decrease in mixing time can be expected from changing a reactor with central gas injection to an eccentric configuration.

Channel-Type Reactors The dispersion number (inverse Peclet number) was used to evaluate the longitudinal mixing for channel-type reactors. By taking into account fluid flow only, the study was focused on finding the conditions that will result in quasi-plug-flow behavior (i.e., $Pe^{-1} \ll 1$), having the physical model setup at UMR as the basis for the analysis. As suggested by the calculations, an efficient counter-current channel-type reactor for metal refining should have the following general characteristics:

1. A small nozzle separation. The minimum nozzle separation explored in our analysis was 16 cm (10 nozzles).

2. A reactor aspect ratio of about 0.8.

3. High gas flow rate generally increases the longitudinal mixing of the system (resulting in a departure from plug flow behavior), but it promotes good mixing in the transversal direction.

4. Increasing horizontal flow rate generally decreases the system dispersion number, i.e., promotes plug flow behavior.

From Mass Transfer Analysis Additional conclusions were obtained from the analysis of the liquid-liquid mass transfer behavior where the reactor conversion ratio was used as the criterion for performance assessment.

1. An 8-nozzle system is preferable to a 4-nozzle system (other things being equal) both in terms of higher interphase mass transfer coefficients and reactor conversion ratios. Small bubbler separation is needed for higher mass transfer coefficients at the interface and hence higher conversion ratios.

2. Increasing gas flow rate is generally beneficial to the interface mass transfer (but this has the tendency of increasing the longitudinal mixing). A correlation was obtained as $k \propto Q^{0.26\sim0.34}$.

3. Lower aspect ratio is good for interface mass transfer in terms of conversion ratios only (although the throughput is also lower).

4. Higher conversion ratio can be obtained by increasing the residence time of the liquid (i.e., by increasing the length of the reactor or decreasing the lower liquid flow rate), hopefully without sacrificing too much in terms of production rate.

5. The height of upper liquid phase, the equilibrium partition ratio between two liquid phases and the upper phase velocity seem to be not very sensitive pa-

rameters in affecting the reactor conversion ratio because, under the conditions studied, the upper phase is still far from saturation when it leaves the reactor.

6. Baffles appeared not to be able to improve the reactor conversion ratios significantly.

7. An optimized design suggested that a length-to-height ratio of 20 is required for a reactor to reach conversion ratio of higher than 90%.

Chapter 7

Future Directions

It is believed that, in its current state, the model is capable of representing the most important features of a counter-current gas-stirred system under isothermal conditions. However, further developments are required in order to obtain a more sound representation of the phenomena involved. This will require incorporating some of the characteristics not included in this work and devoting more attention to some of the details considered here.

In this final chapter, we will summarize those areas that should be the basis for future work.

7.1 Fluid Flow and Mixing

1. Explore more realistic and well tested turbulence models to represent the flows involving gas bubbles and recirculations caused by buoyancy.

2. Further consideration on the appropriate boundary conditions for turbulence equations at the free surfaces.

3. Investigate the swirling motion of the gas plumes which happens as the gas flow rate reaches some critical value.

4. Analysis of multiple injections in cylindrical system, for example, electric arc furnace (optimal nozzle number and arrangement).

5. Heat transfer analysis is important to complete the current two phase model and extend the model to analyze a real industrial system.

6. Consider the entrainment of upper liquid phase into the lower liquid phase as the gas stirring gets very intense.

7. Non-flat surface and surface waves (not so important in channel type reactor because this kind of phenomena is really harmful to the performance of the reactor)

8. Complete simulation of three phases (melt-slag-gas) after knowing the quantitative relations between gas-liquid and liquid-liquid interactions.

7.2 Mass Transfer

1. Incorporate different controlling mechanism when the species concentration in the lower liquid phase is higher than some critical value.

2. Analysis on the increase of mass transfer rate between liquid-liquid interface by the increasing of interface area (entrainment).

3. Effect of upper liquid phase height on mass transfer coefficient at the interface.

4. Resistance from upper liquid phase.

5. Additional reaction involving the gas phase.

7.3 Others

Additional issues need to be addressed to determine the feasibility of a counter-current reactor used for metal refining. These include:

- Cost estimation.

- Environmental concerns.

- Issues related to scale-up of model results (physical and mathematical).

- Reactor stability and control issues.

- Energy consumption and production level.

In the mean time, some suggestions are given to the type of laboratory scale experimental measurements required for better validation of mathematical models.

- Additional characteristics of fluid flow and turbulence, such as velocities, gas holdup, bubble size and frequency, should be measured.

- A steady state tracer analysis is suggested from both heat and mass transfer point of view.

Bibliography

[1] Mills, L. A., Hallett, G. D. and Newman, C. J., 1976, *Extractive Metallurgy of Copper*, editors Yannopoulos, J. C. and Agarwal, J. C., vol. 1, pp. 458-487.

[2] Queneau, P. E. and Siegmund, A., 1996, *JOM*, April, pp. 38-44.

[3] Mazumdar, D. and Guthrie, R. I. L., 1995, *ISIJ International*, vol. 35, pp. 1-20.

[4] Iguchi, M., Ilegbusi, O. J., Ueda, H., Kuranaga, T. and Morita, Z., 1996, *Metallurgical and Materials Transactions*, vol. 27B, pp. 35-41.

[5] Sahai, Y., 1988, *Metallurgical Transactions*, vol. 19B, pp. 603-612.

[6] Koch, K., Bruckhaus, R., Korte, E., Roth, C. and Falkus, J., 1994, *ISIJ International*, vol. 34, pp. 234-240.

[7] Koch, K., Steinmetz, E., Lamut, J. and Korte, E., 1990, *Proceedings of The Sixth International Iron and Steel Congress*, Nagaya, pp. 386.

[8] Nelson, L. R. and Robertson, D. G. C., 1994, *Steelmaking Conference Proceedings*, pp. 665-680.

[9] Sohn, H. Y., Robertson, D. G. C., Agrawal, A. K. and Iyer, K. M., 1992, *Proceedings of the Savard/Lee International Symposium on Bath Smelting*, Edited by Brimacombe, J. K. et al., pp. 377-413.

[10] Iyer, K. M. and Sohn, H. Y., 1994, *Metallurgical and Materials Transactions*, vol. 25B, pp. 207-219.

[11] Iyer, K. M. and Sohn, H. Y., 1994, *Metallurgical and Materials Transactions*, vol. 25B, pp. 619-623.

[12] Grevet, J. H., Szekely, J. and El-Kaddah, N., 1982, *International Journal of Heat and Mass Transfer*, vol. 25, pp. 487-497.

[13] Debroy, T., Majumdar, A. K. and Spalding, D. B., 1978, *Appl. Math. Modelling*, vol. 2., pp. 146.

[14] Mazumdar, D. and Guthrie, R. I. L., 1985, *Metallurgical Transactions*, vol. 16B, pp. 83-91.

[15] Woo, J. S., Szekely, J., Castillejos, A. H. and Brimacombe, J. K., 1990, *Metallurgical Transactions*, vol. 21B, pp. 269-277.

[16] Sheng, Y. Y. and Irons, G. A., 1993, *Metallurgical Transactions*, vol. 24B, pp. 695-705.

[17] Mazumdar, D. and Guthrie, R. I. L., 1994, *ISIJ International*, vol. 34, pp. 384-392.

[18] Salcudean, M. and Lai, K. Y. M., 1988, *Numerical Heat Transfer*, vol. 14, pp. 97-111.

[19] Johansen, S. T. and Boysan, F., 1988, *Metallurgical Transactions*, vol. 19B, pp. 755-764.

[20] Neti, S. and Mohamed, O. E. E., 1990, *Int. J. Heat and Fluid Flow*, vol. 11, pp. 204-213.

[21] Neifer, M., Rödl, S. and Sucker, D., 1993, *Steel Research*, vol. 64, pp. 54-62.

[22] Koh, P. T. L., Markatos, N. C. and Cross, M., 1987, *PCH PhysicoChemical Hydrodynamics*, vol. 9, pp. 197-207.

[23] Schwarz, M. P., 1996, *Appl. Math. Modelling*, vol. 20, pp. 41-51.

[24] Schwarz, M. P., 1991, *ISIJ International*, vol. 31, pp. 947-951.

[25] Davidson, M. R., 1990, *Appl. Math. Modelling*, vol. 14, pp. 67-76.

[26] Ilegbusi, O. J. and Szekely, J., 1994, *ISIJ International*, vol, 34, pp. 943-950.

[27] Turkoglu, H. and Farouk, B., 1992, *Numerical Heat Transfer*, vol. 21, pp. 377-399.

[28] Burty, M., Fautrelle, Y. and Huin, D., 1990, *Proceedings of The Sixth International Iron and Steel Congress*, Nagoya, pp. 444.

[29] Jönsson P. and Jonsson L., 1995, *SCANINJECT VII: 7th International Conference on Refining Processes*, Luleå, Sweden, pp. 385-412.

[30] Mazumdar, D. and Guthrie, R. I. L., 1994, *Metallurgical and Materials Transactions*, vol. 25B, pp. 308-312.

[31] Thring, M. W., 1969, *Journal of Metals*, June, pp. 66-69.

[32] Kim, S. and Fruehan, R. J., 1987, *Metallurgical Transactions*, vol. 18B, pp. 381-390.

[33] Abel, C. A., Fruehan, R. J. and Vassilicos, A., 1995, *Iron and Steelmaker*, July, pp. 47-56.

[34] Abel, C. A., Fruehan, R. J. and Vassilicos, A., 1995, *Iron and Steelmaker*, August, pp. 49-64.

[35] Spalding, D. B., 1981, *Recent Advances in Numerical Methods in Fluids*, pp. 139-167, editors Taylor, C. and Morgan, K., Pineridge Press, Swansea.

[36] CHAM, 1990, *PHOENICS Instruction Course*, CHAM/TR/300.

[37] Patankar, S. V., 1980, *Numerical Heat Transfer and Fluid Flow*, Hemisphere Publishing Corporation.

[38] Launder, B. E. and Spalding, D. B., 1972, *Mathematical Models of Turbulence*, Academic Press.

[39] Malin, M. R. and Spalding, D. B., 1984, *PhysicalChemical Hydrodynamics*, vol. 5, pp. 339-362.

[40] Simonin, O. and Viollet, P. L., 1988, *EUROMECH 234*, Toulouse, France.

[41] Clift, R., Grace, J. R. and Weber, M. E., 1978, *Bubbles, Drops, and Particles*, Academic Press.

[42] Szekely, J. and Themelis, N. J., 1971, *Rate Phenomena in Process Metallurgy*, Wiley-Interscience.

[43] Danckwerts, P. V., 1953, *Chemical Engineering Science* vol. 2, pp. 1.

[44] Levenspiel, O., 1972, *Chemical Reaction Engineering*, John Wiley & Sons.

[45] CHAM, 1992, *The GENTRA User Guide*, CHAM/TR/211.

[46] Gosman, A. D. and Ioannides, 1981, *AIAA 19th Aerospace Sciences Meeting*, St. Louis, Missouri.

[47] Fruehan, R. J., 1985, *Ladle Metallurgy Principles and Practices*, A Publication of the Iron and Steel Society.

[48] Sano, M., Mori., K. and Fujita, Y., 1979, *Tetsu-to-Hagane*, vol. 65, pp. 1140-1148.

[49] Mori, K., Sano, M. and Sato, T., 1979, *ISIJ International*, vol. 19, pp. 553-558.

[50] Anagbo, P. E., Brimacombe, J. K. and Castillejos, A. H., 1989, *Canadian Metallurgical Quarterly*, vol. 28, pp. 323-330.

[51] Davidson, L. and Amick, E. H., Jr., 1956, *AIChE Journal*, vol. 2, pp. 337-342.

[52] Iguchi, M., et al. 1994, private communication.

[53] Mietz, J. and Oeters, F., 1987, *Steel Research*, vol. 58, pp. 446.

[54] Joo, S. and Guthrie, R. I. L., 1992, *Metallurgical Transactions*, vol. 23B, pp. 765-778.

[55] Krishna Murthy, G. G., Mehrotra, S. P. and Ghosh, A., 1988, *Metallurgical Transactions*, vol. 19B, pp. 839-850.

[56] Roth, C., Peter, M., Schindler, M. and Koch, K., 1995, *Steel Research*, vol. 66, pp. 325-330.

[57] Zhu, M., Inomoto, T., Sawada, I. and Hsiao, T., 1995, *ISIJ International*, vol. 35, pp. 472-479.

[58] Zhu, M., Sawada, I., Yamasaki, N. and Hsiao, T., 1996, *ISIJ International*, vol. 36, pp. 503-511.

[59] Mietz, J. and Oeters, F., 1989, *Steel Research*, vol. 60, pp. 387-394.

[60] Pan, Y., Guo, D., Ma, J., Wang, W., Tang, F. and Li, C., 1994, *ISIJ International*, vol. 34, pp. 794-801.

[61] Xie, Y. and Oeters, F., 1992, *Steel Research*, vol. 63, pp. 93-104.

[62] Xie, Y. and Oeters, F., 1994, *Steel Research*, vol. 65, pp. 315-319.

[63] Iguchi, M., Kawabata, H., Ito, Y., Nakajima, K. and Morita, Z. 1994, *ISIJ International*, vol. 34, pp. 980-985.

[64] Iguchi, M., Kawabata, H., Nakajima, K. and Morita, Z. 1995, *Metallurgical and Materials Transactions*, vol. 26B, pp. 67-74.

[65] Mazumdar, D., Nakajima, H. and Guthrie, R. I. L., 1988, *Metallurgical Transactions*, vol. 19B, pp. 507-511.

[66] Taniguchi, S., Okada, Y., Sakai, A. and Kikuchi, A., 1990, *Proceedings of The Sixth International Iron and Steel Congress*, Nagoya, pp. 394.

[67] Richter, H. J., Laaspere, J. T. and Fitzpatrick, J. M., 1994, *Metallurgical Processes for Early Twenty-First Century*, edited by Sohn, H.Y., pp. 859-878.

[68] Szekely, J., Carlsson, G. and Helle, L., 1988, *Ladle Metallurgy*, Springer-Verlag.

[69] Wilson, W. G. and McLean, A., 1980, *Desulfurization of Iron and Steel and Sulfide Shape Control*, Iron and Steel Society of AIME.

[70] Richardson, F. D., 1974, *Physical Chemistry of Melts in Metallurgical*, Academic Press.

[71] El-Kaddah, N. and Szekely, J., 1981, *Ironmaking and Steelmaking*, No. 6, pp. 269-278.

[72] Turkdogan, E. T., 1986, *Symposium on Kinetics of Metallurgical Processes*, edited by O. Jarvinen, pp. 125-150.

[73] Turkdogan, E. T., 1981, *Metallurgical Treaties*, edited by J. K. Tien and J. F. Elliott, pp. 79-94.

[74] Asai, S., Kawachi, M. and Muchi, Iwao, 1983 *SCANINJECT III*, Luleå, Sweden, pp. 12:1.

[75] Gilchrist, J. D., 1980, *Extractive Metallurgy*, 2nd edition, Pergamon Press.

[76] Turkdogan, E. T., 1983, *Physicochemical Properties of Molten Slags and Glasses*, The Metals Society, London.

[77] Kataoka, H. and Miyauchi, T., 1969, *Kaguku Kogaku*, vol. 33, pp. 181.

[78] Nelson, L. R., Robertson, D. G. C. and Swamy, K. N., 1995, *Proceedings of 1995 TMS Annual Meeting*, Las Vegas.

[79] Swamy, K. N., Robertson, D. G. C. and Peaslee, K. D., 1996, *Proceedings of 1996 TMS Annual Meeting*, Anaheim, CA.

[80] Patel, P., Frohberg, M. G. and Biswas, K., 1975, *Kinetics of Metallurgical Processes in Steelmaking*, "The Effect of Rising Gas Bubbles on the Mass Transfer between Liquid Iron and FeO-Bearing Slags," pp. 180-191.

[81] Oeters, F., 1975, *Kinetics of Metallurgical Processes in Steelmaking*, "Convective Diffusion with Chemical Reaction," pp.116-135.

[82] Gerlach, F. and Frohberg, M. G., 1993, *Steel Research*, vol. 64, pp. 7-14.

[83] Frohberg, M. G., Gerlach, F. and Handschuh, G. 1990, *Steel Research*, vol. 61, pp. 151-156.

[84] Hirasawa, M., Mori, K., Sano, M., Hatanaka, A., Shimatani, Y. and Okazaki, Y., 1987, *Transactions ISIJ*, vol. 27, pp. 277-282.

[85] Hirasawa, M., Mori, K., Sano, M., Hatanaka, A., Shimatani, Y. and Okazaki, Y., 1987, *Transactions ISIJ*, vol. 27, pp. 283-290.

[86] Nelson, L. R., Robertson, D. C. and Swamy, K. N., 1994, *EPD Congress 1994*, edited by G. Warren, pp. 713-737.

[87] Gupta, S. K., Agrawal, R. D., Gupta, S. S. and Kapoor, M. L., 1988, *Ironmaking and Steelmaking* vol. 15, pp. 82-89.

[88] Deng, J. and Oeters, F., 1990, *Steel Research*, vol. 61, pp. 438-448.

[89] Xie, H. and Oeters, F., 1995, *Steel Research*, vol. 66, pp. 501-508.

[90] Geiger, G. H. and Poirier, D. R., 1973, *Transport Phenomena in Metallurgy*, Addison-Wesley Publishing Company.

[91] Brimacombe, J. K., *Class Notes of Metallurgy 460: Mass Transfer in Metallurgical Processes*, University of British Columbia, Vancouver, B.C. V6T 1W5.

[92] Sano, M. and Mori., K., 1992, *Proceedings of the Savard/Lee International Symposium on Bath Smelting*, Edited by J. K. Brimacombe et al., pp. 465-492.

[93] Robertson, D. G. C. and Staples, B. B., 1974, *Process Engineering of Pyrometallurgy*, edited by M. J. Jones, pp. 51-59.

[94] Richardson, F. D., Robertson, D. G. C. and Staples, B. B., 1976, *Physical Chemistry in Metallurgy: Proceedings of Darken Conference*, Edited by R. M. Fisher et al., pp. 25-48.

[95] Paul, S. and Ghosh, D. N., 1986, *Metallurgical Transaction*, vol 17B, pp. 461-469.

[96] Lewis, W. K. and Whitman, W., 1924, *Industrial and Engineering Chemistry*, vol. 16, pp. 1215.

[97] Higbie, R., 1935, *Transactions of the American Institute of Chemical Engineers*, vol. 31, pp. 365-388.

[98] Danckwert, P. V., 1951, *Industrial and Engineering Chemistry*, vol. 43, pp. 1460-1467.

[99] Fortescue, G. E. and Pearson, J. R. A., 1967, *Chemical Engineering Science*, vol. 22, pp. 1163-1176.

[100] Lamont, J. and Scott, D. S., 1970, *AIChE Journal*, vol. 16, pp. 513-519.

[101] Henstock, W. H. and Hanratty, T. J., 1979, *AIChE Journal*, vol. 25, pp. 122-131.

[102] Sonin, A. A., Shimko, M. A. and Chun, J., 1986, *Int. J. Heat Mass Transfer*, vol. 29, pp. 1319-1332.

[103] Theofanous, T. G., 1984, *Gas Transfer at Water Surfaces*, edited by W. Brutsaert and G. H. Jirka, published by D. Reidel Publishing Company.

[104] Singh, R. P. and Ghosh, D. N., 1990, *Ironmaking and Steelmaking*, vol. 17, pp. 333-342.

[105] Nakanishi, K., Fujii, T. and Szekely, J., 1975, *Ironmaking and Steelmaking*, vol. 3, pp. 193-197.

[106] Sinha, U. P. and McNallan, M. J., 1985, *Metallurgical Transactions*, vol. 16B, pp. 850-853.

[107] Prasher, B. D. and Wills, G. B., 1973, *Ind. Eng. Chem. Process Des. Develop.*, vol. 12, pp. 351-354.

[108] Mazumdar, D. and Guthrie, R. I. L., 1986, *Metallurgical Transactions*, vol. 17B, pp. 725.

[109] Krishnamurthy, G. G., Mehrota, S. P. and Ghosh, A., 1988, *Metallurgical Transactions*, vol. 19B, pp. 839.

Appendix A

Residence Time Distribution Analysis

The variation of actual residence times from the calculated average is called the distribution of residence times. A continuous flow reactor in which all fluid elements have the same residence time is called a plug flow reactor. On the other hand, the reactor is called perfectly mixed when material fed at one point is rapidly mixed throughout the volume of the reactor.

Experimental measurements of residence time distribution (RTD) provide a means of estimating the performance of reactors when the system can be assumed sufficiently isothermal and with first-order reactions.

The residence time distribution of a fluid flowing through a continuous reactor can be determined by means of tracer tests. There are two major ways of carrying out tracer tests: injecting tracer by step input or by pulse input. The later one is the more popular one because of its sensitivity and convenience.

Step Input   In this method a quantity of tracer m_{tr} is thoroughly mixed into the inlet stream while the addition of tracer is continued indefinitely and at a constant ratio. The measured concentration at the outlet can be used to characterize the flow behavior in the reactor. No further details will be given here since the other method, the pulse input method, was used in this study.

Pulse Input In this method a quantity of tracer m_{tr} is again thoroughly mixed into the inlet stream during a period of time which must be very short compared to the mean residence time of the fluid in the reactor. The concentration of tracer c in the outlet stream is measured from the moment of addition until it is no longer detectable.

The results can be plotted in dimensionless, thus more general, form by using the variable C for the dimensionless concentration and τ for the dimensionless time, i.e.,

$$C = \frac{c}{m_{tr}/V} = \frac{c}{c_o} \tag{A.1}$$

and

$$\tau = \frac{t}{t_{mean}} \tag{A.2}$$

where c is the concentration of tracer in the exit stream at time t; m_{tr} is the mass of injected tracer; V is the volume of the liquid in the reactor; t_{mean} is the nominal mean residence time of the liquid in the reactor. The denominator of (A.1) represents the equilibrium concentration that the tracer would reach if it were mixed "instantaneously" with the contents of the reactor.

This type of plot, based on the pulse signal, is given the name "C-diagram" by Danckwerts [43]. If there were a close approximation to plug flow the plot would rise to a sharp peak at the mean residence time. The greater the deviation from plug flow the greater is the "spread" of the measured concentrations and the less sharp is the peak. Figure A-1 shows a sketch of three different behavior types: (a) perfectly mixed flow, when some of the tracer will appear at the exit immediately after it has been added; (b) plug flow, when t=t_{mean}; and (c) the most realistic case, a combination of plug flow, perfect mixing and "dead zone".

The shape of the C-diagram varies considerably between different reactors and can provide useful information as to the flow characteristics in a reactor. The area under each C-curve is equal to unity, since all the tracer introduced at the inlet must eventually leave the system, i.e.,
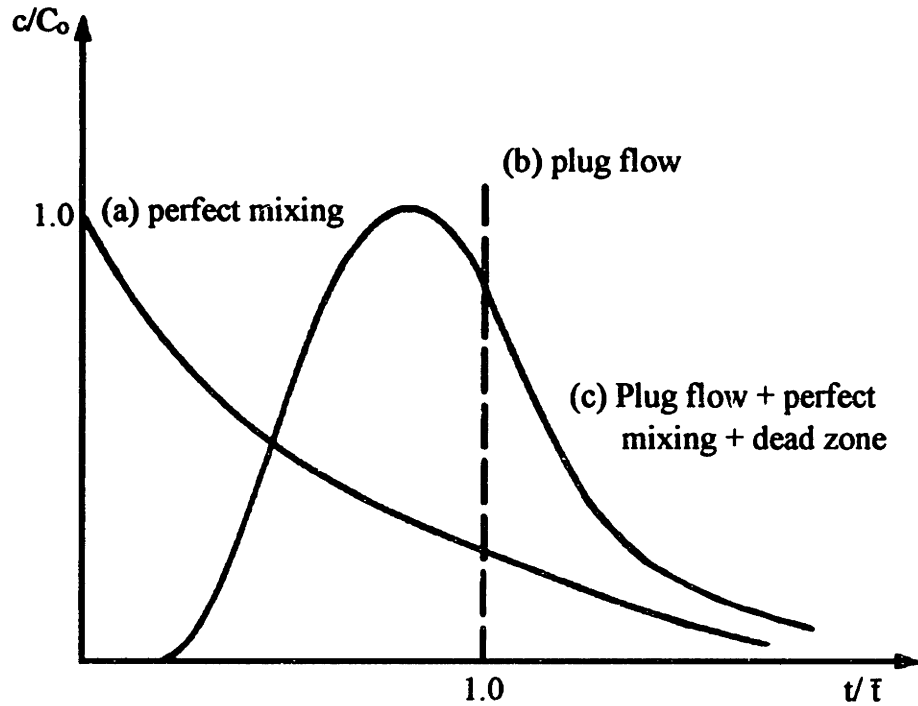
Figure A-1: Typical C-diagrams from a pulse addition of tracer.

$$\int_0^\infty Cd\tau = 1 \qquad (A.3)$$

The Mean and the Variance One of the most important measure of distribution is the mean value of it which is defined as the actual mean residence time. The actual mean residence time of the fluid in the reactor can be obtained by integrating the C-curves by using the following equation [42]:

$$\bar{t}_{mean} = \frac{\int_0^\infty ctdt}{\int_0^\infty cdt} \qquad (A.4)$$

Another important descriptive quantity is the spread of the distribution, which is commonly measured by the variance. The statistical variance σ^2, or square of the standard deviation, which has units of (time)^2 and is defined by:

$$\sigma^2 = \frac{\int_0^\infty c(t - \bar{t}_{mean})^2 dt}{\int_0^\infty cdt} \qquad (A.5)$$

164

By analyzing the actual mean residence time and the variance, important characteristic of the fluid flow in a reactor can be obtained. This includes, for example, the determination of the Peclet number (Pe) from which a overall longitudinal diffusivity of a flow system can be obtained using the following expression:

$$\sigma^2 = 2D_e/uL - 2(D_e/uL)^2(1 - e^{-\frac{uL}{D_e}}) = 2Pe^{-1} - 2Pe^{-2}(1 - e^{-Pe}) \qquad \text{(A.6)}$$

This approach is widely used by chemical engineers to establish a measure of the overall mixing characteristics in a reactor and the distribution of residence times. Subsequently, the performance of a reactor can be estimated. For more detailed description of this topic, please refer to some of the good textbooks [42, 44].

Appendix B

Derivation of the Velocity Profiles

A highly idealized system where two layers of liquids are flowing counter-currently is solved analytically. The bottom gas injections are not taken into account here, and the flow is considered as two dimensional as well as laminar.

Figure B-1 is a schematic of the system where two layers of fluids are flowing counter-currently and each layer has its own viscosity, density and height. The coordinate system is shown as in the figure.

The general differential equation describing the motion of fluid in each of the layers can be obtained from simplification of laminar Navier-Stokes equations:

$$0 = -\frac{\partial p}{\partial x} + \mu(\frac{\partial^2 u}{\partial y^2}) \tag{B.1}$$

For fluid #1 (lower layer), assuming $(\frac{\partial p}{\partial x})_1 = C_1$, then the solution of the velocity profile for fluid 1 would be:

$$u_1 = \frac{C_1}{2\mu_1}y^2 + C_2 y + C_3 \tag{B.2}$$

where C_1, C_2 and C_3 are constants to be decided.

Similarly for fluid #2 (upper layer), assuming $(\frac{\partial p}{\partial x})_2 = D_1$, then the solution of the velocity profile for fluid 2 would be:
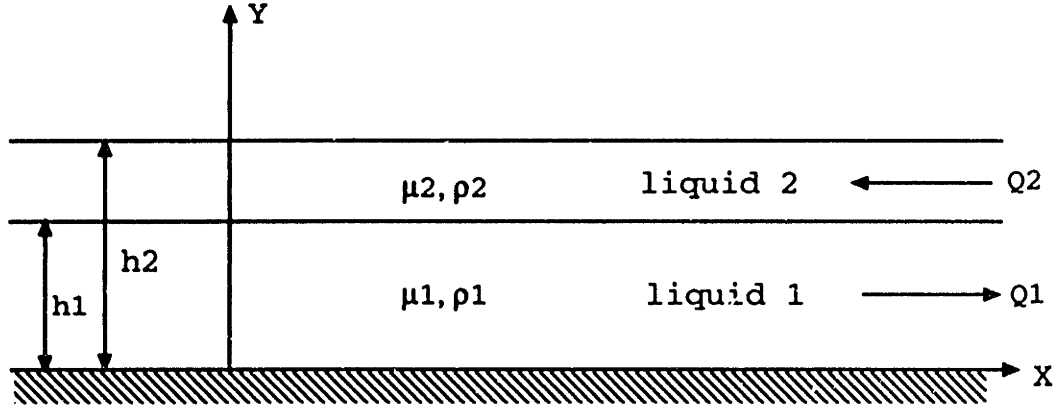
Figure B-1: A schematic representation of an idealized two-layer counter-current flow system.

$$u_2 = \frac{D_1}{2\mu_2}y^2 + D_2 y + D_3 \tag{B.3}$$

where D_1, D_2 and D_3 are constants to be decided.

The boundary conditions are:

$u_1 = 0$ at $y = 0$ (bottom)

$\mu_2 \frac{\partial u_2}{\partial y} = 0$ at $y = h_2$ (top)

$\mu_1 \frac{\partial u_1}{\partial y} = \tau_{12} = \mu_2 \frac{\partial u_2}{\partial y}$ at $y = h_1$ (interface)

$\int_0^{h_1} u_1 dy = Q_1 = U_1 h_1$

$\int_{h_1}^{h_2} u_1 dy = Q_2 = U_2(h_2 - h_1)$

where U_1 and U_2 are the average velocity of the lower and upper layer, respectively; τ_{12} is the shear force at the two-layer interface.

Now we have five equations to solve for six unknowns. Obviously, another condition is needed to obtain a unique solution of six unknowns. Let's assume the slip velocity $(u_1(h_1) - u_2(h_1))$ at the two-layer interface is ΔU, then we can solve for C_1, C_2, C_3, D_1, D_2 and D_3.

The results are obtained as follows:

167

Table B.1: Parameters used to calculate the velocity profiles.

h_1 (m)	h_2 (m)	μ_1 (kg/ms)	μ_2 (kg/ms)	U_1 (m/s)	U_2 (m/s)
0.2	0.3	0.0008	0.0009	0.0035	-0.0065

$$C_1 = -\frac{3\mu_1}{h_1}\left(\frac{U_1}{h_1} + \frac{9U_1 - 6U_2 - 6\Delta U}{4h_2 - h_1}\right) \tag{B.4}$$

$$C_2 = \frac{3U_1}{h_1} - \frac{9U_1 - 6U_2 - 6\Delta U}{4h_2 - h_1} \tag{B.5}$$

$$D_1 = \frac{2\mu_2(9U_1 - 6U_2 - 6\Delta U)}{(h_2 - h_1)(4h_2 - h_1)} \tag{B.6}$$

$$D_2 = -\frac{2h_2(9U_1 - 6U_2 - 6\Delta U)}{(h_2 - h_1)(4h_2 - h_1)} \tag{B.7}$$

$$D_3 = U_2 - \frac{(h_1^2 - 2h_1h_2 - 2h_2^2)(3U_1 - 2U_2 - 2\Delta U)}{(h_2 - h_1)(4h_2 - h_1)} \tag{B.8}$$

with $C_3 = 0$.

Since we don't know what kind of values ΔU would be, trying to find its lower or upper bound will be helpful. It is to be noted that there are both an upper and a lower limit for ΔU which should be $\Delta U_{min} = 0$ and $\Delta U_{max} = |U_1| + |U_2| = U_1 - U_2$.

Figure B-2 shows how the velocity profile would change as the slip velocity between the two liquid layers changes. The parameters used for the calculation of velocity profiles, which were taken from the physical model at UMR, are shown in Table B.1.

For flow in turbulence regime, the velocity profile would be much flatter than what is shown in Figure B-2.
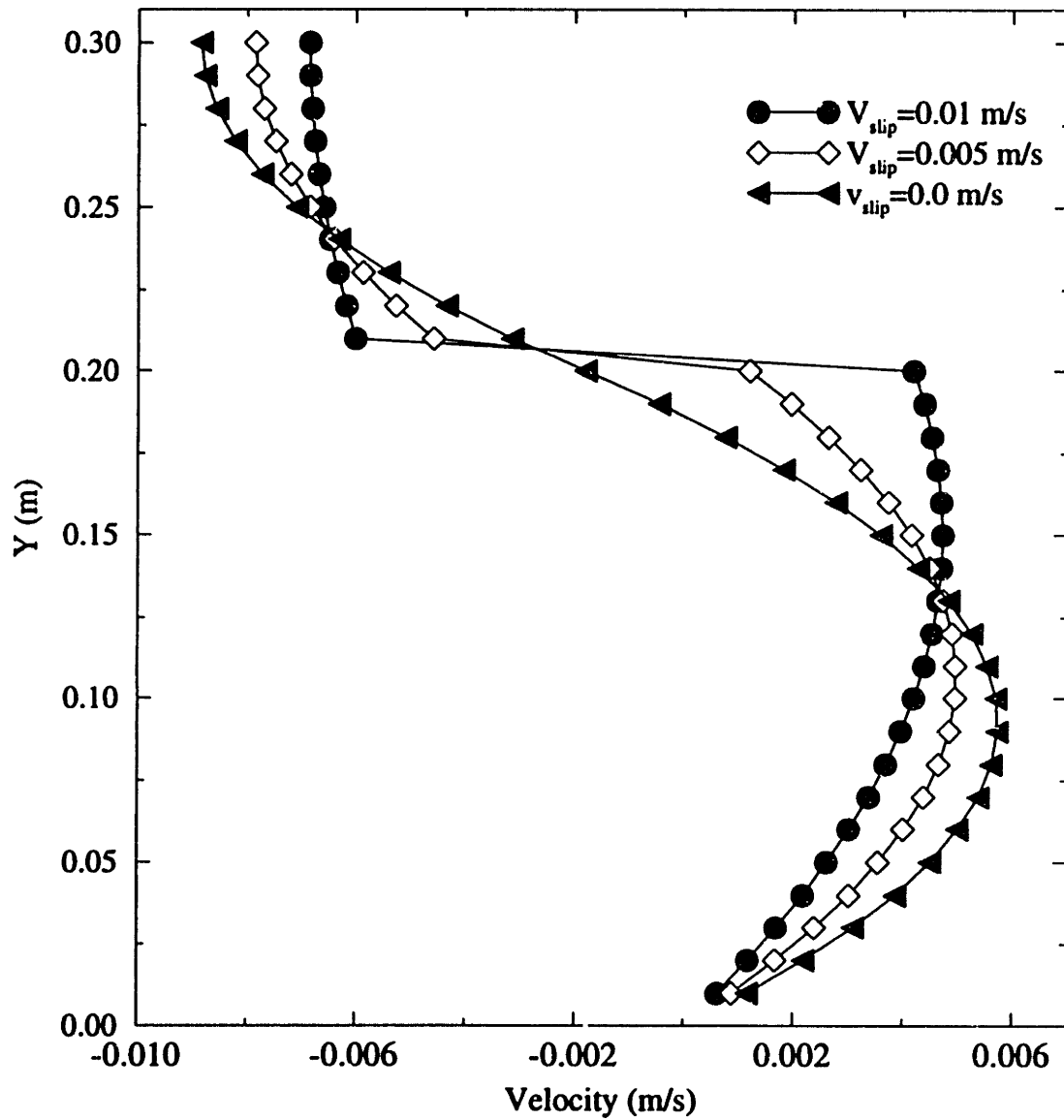
Figure B-2: Velocity profiles under different slip velocities between the two liquid layers.

Appendix C

A Summary of Desulfurization Process in Steelmaking

Desulfurization of steel is usually done in a ladle to produce clean or ultraclean steels. There are three main methods by which sulfur may be removed from molten steel:

1. By reaction with metallic additions such as magnesium or rare earth elements, which in combination with sulfur form very stable sulfides.

2. By reaction with compound additives such as calcium-carbide (CaC_2) or soda-ash (Na_2CO_3).

3. By reaction with fluid slags.

A synthetic slag used to treat the steel has to be basic and nonoxidizing with the following general requirements.

1. low oxygen potential (by the addition of strong deoxidizers, such as powdered aluminum);

2. low melting point (around 1600°C);

3. moderate fluidity;

4. large solubility for alumina and sulfur.

The slags having these characteristics are generally found in the CaO-FeO-SiO$_2$ or CaO-Al$_2$O$_3$-SiO$_2$ systems. The ternary phase diagram of these systems are shown in Figure C-1 (from [75]) in which the shaded area shows the range of composition which melt at around 1300°C and 1500°C, respectively. Typically, the slags for desulfurization will contain: 50-60% CaO, 3-8% MgO, 3-8% MnO, 6-26% FeO, 15-25% SiO$_2$, 1-5% P$_2$O$_5$, <1% Al$_2$O$_3$ and <0.2% S [73]. The removal of sulfur from the metal phase is realized by reaction with lime in the slag phase, to form calcium sulfide in the slag and oxygen in the metal, which can be represented by the following overall equations:

$$(CaO) + \underline{S} = (CaS) + \underline{O} \tag{C.1}$$

or

$$3(CaO) + 2\underline{Al} + 3\underline{S} = 3(CaS) + (Al_2O_3) \tag{C.2}$$
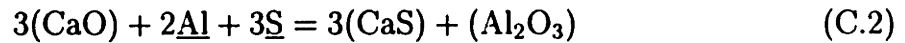
The equilibrium constant for the first reaction may be expressed as:

$$K = \frac{a_{CaS}a_O}{a_{CaO}a_S} \tag{C.3}$$

and for the second reaction:

$$K = \frac{a_{CaS}^3 a_{Al_2O_3}}{a_{CaO}^3 a_S^3 a_{Al}^2} \tag{C.4}$$

where a is the activity of the respective species. Equation (C.3) readily shows that the lower the oxygen activity, the lower will be the equilibrium sulfur content of the steel. This clearly underlines the need to deoxidize the steel first, before desulfurization.

The sulfide capacity concept can be used to express desulfurization equilibria. The sulfide capacity of the slag may be defined as

$$C_S = (wt.\%S)_{slag}(\frac{P_{O_2}}{P_{S_2}})^{1/2} \tag{C.5}$$

where P_{O_2} and P_{S_2} stand for the partial pressure of oxygen and sulfur based on reaction (C.1). The sulfide capacity is mainly a function of temperature and basicity of the slag. Therefore, the higher the sulfide capacity, the greater the ability of the
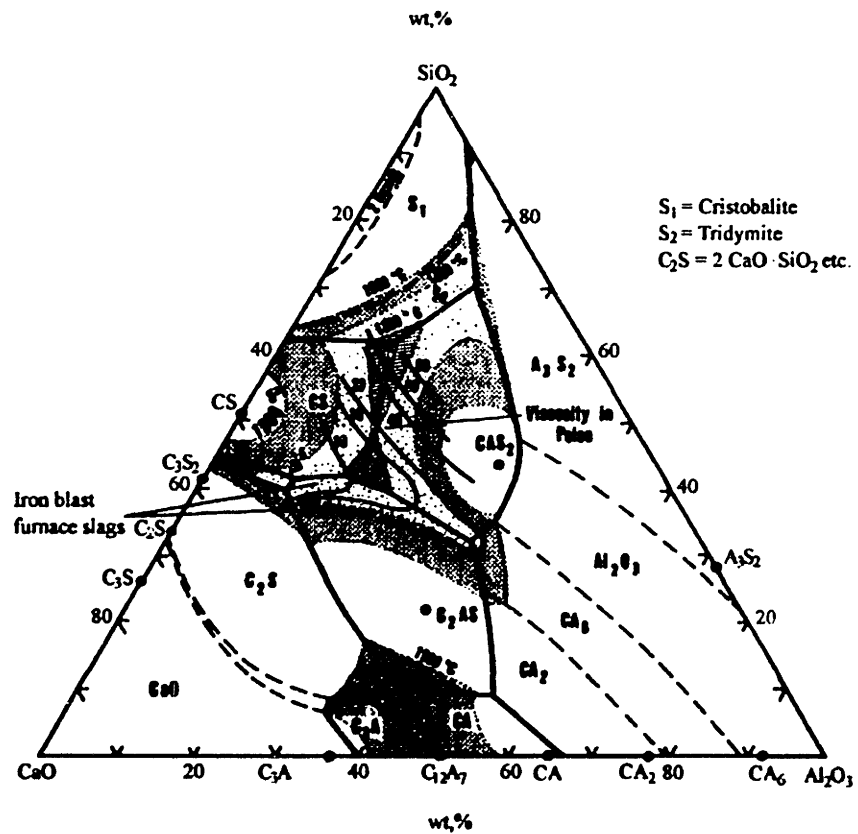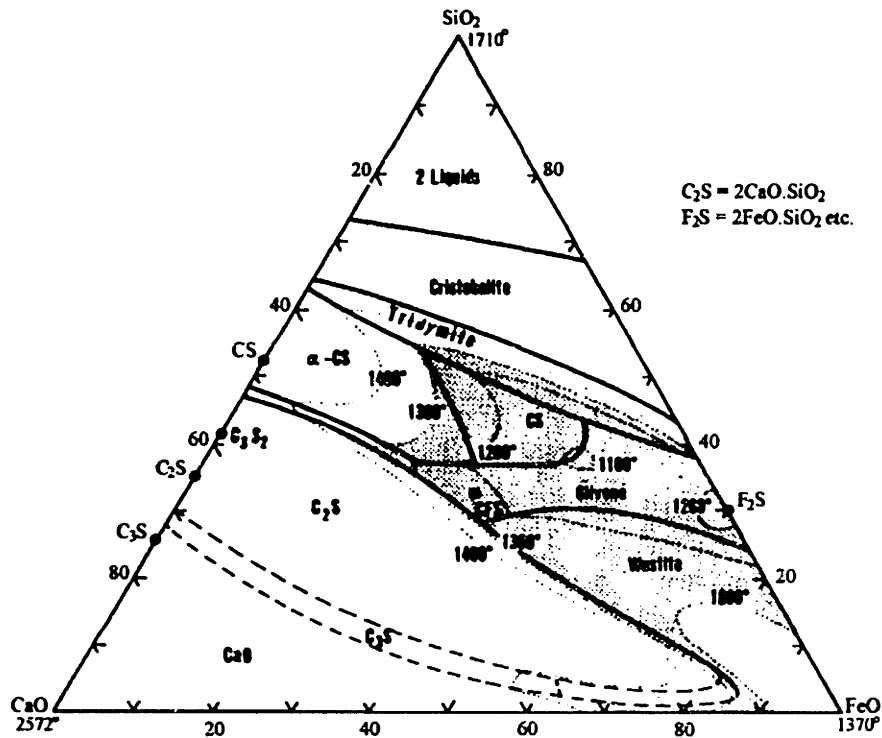
Figure C-1: Phase diagrams of CaO-FeO-SiO₂ and CaO-Al₂O₃-SiO₂ systems.

172

slag to absorb sulfur. The desulfurizing slags can absorb sulfur up to a limit at which CaS starts precipitating.

Typically 20 to 25 pounds (8 to 10 kgs) of synthetic slags are used per ton of steel in typical ladle refining operations. The slag-to-metal ratio (mass) is usually larger in continuous process. For example, the slag-to-metal ratio suggested for optimum metallurgical performance of a CCRL (counter-current reaction launder) is in the range of 3.5 to 1, according to estimations by Nelson et al. [86].

The equilibrium partition ratio of sulfur between slag and metal is defined as the sulfur content in the slag phase divided by the sulfur content in the metal phase:

$$P_s = \frac{(\%S)}{[\%S]} = \frac{c'_s}{c'_m} \tag{C.6}$$

where c'_s and c'_m are the equilibrium concentration of sulfur in the slag phase and metal phase, respectively. For a given temperature and oxygen activity, the sulfur distribution ratio between slag and metal increases with increasing the basicity of the slag.

Figure C-2 shows a plot of the sulfur partition ratio for a Fe-Al alloy at 1550°C and 1650°C for a CaO saturated slag, as a function of the aluminum content of the slag. The round brackets denote the slag phase and the square brackets the metal phase. It is seen that the partition ratio increases with increasing aluminum content. It is also noted that lower temperature will tend to favor desulfurization equilibria. However, kinetic aspects are favored at higher temperature and some balance will be the determining factor in establishing the rate at which the reaction would occur.

From activation energy point of view, it is generally believed that the chemical reaction is not the controlling step in the process of desulfurization of steel [70], in part, due to the high operating temperature involved. Therefore, it is reasonable to assume that the rates of solute transfer are controlled by transport processes in the phases involved. That is, the reactions are mass-transfer limited. In fact, there is a great deal of experimental work that supports this suggestion [80, 89, 87].
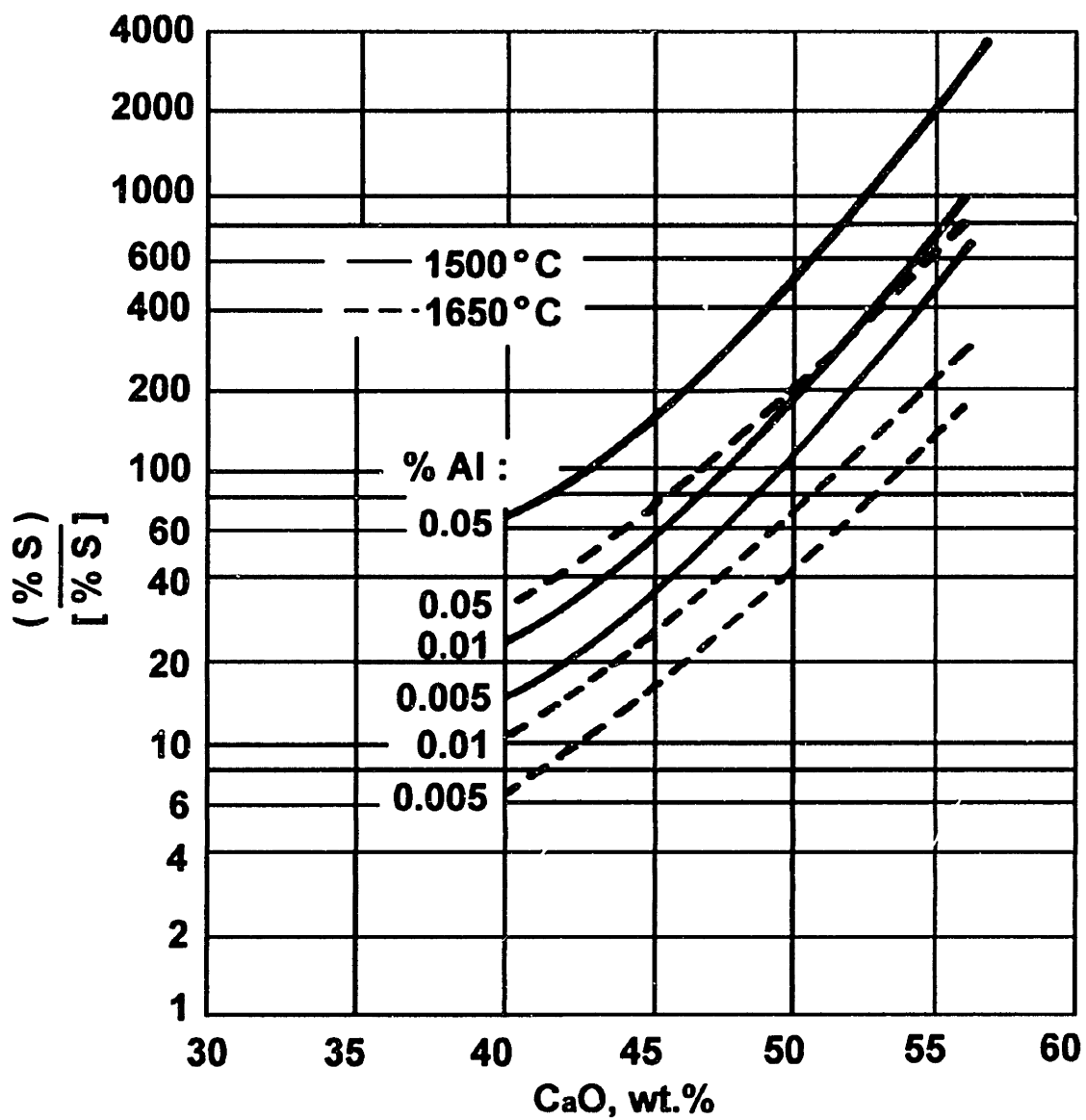
Figure C-2: Sulfur partition ratio between slag and metal for Fe-Al alloys in equilibrium with CaO-Al$_2$O$_3$ slags.

174

Assuming that mass transfer is the rate limiting step in operations such as desulfurization, there are two liquid boundary layers offering resistance to overall mass transfer process. Mass fluxes at the two phase boundaries under steady state condition would be:

$$J = k_m(c_m - c'_m) = k_s(c'_s - c_s) \tag{C.7}$$

where k_m is the mass transfer coefficient in the metal phase and k_s is the mass transfer coefficient in the slag phase; c_m and c_s are the sulfur concentration in the metal and slag phases, respectively. Substitute c'_s with the equilibrium partition ratio of sulfur P_s, one can get:

$$c'_m = \frac{k_m c_m + k_s c_s}{k_m + P_s k_s} \tag{C.8}$$

and the flux can be represented by:

$$J = k_o(c_m - \frac{c_s}{P_s}) \tag{C.9}$$

where k_o is the overall mass transfer coefficient which is a combination of k_s and k_m:

$$k_o = \frac{1}{\frac{1}{k_m} + \frac{1}{P_s k_s}} \tag{C.10}$$

Some important conclusion can be obtained from analysis of above equation. When

$$\frac{1}{P_s k_s} \gg \frac{1}{k_m} \tag{C.11}$$

the main resistance to mass transfer corresponds to the slag phase. When

$$\frac{1}{P_s k_s} \ll \frac{1}{k_m} \tag{C.12}$$

the main resistance to mass transfer corresponds to the metal phase.

Since the difference between k_m and k_s is rarely larger than an order of magnitude, and the equilibrium partition ratio of sulfur between slag and metal is usually in the

175

range 200~500, one can reasonably assume that the mass transfer on the metal side is the controlling mechanism for desulfurization. In fact, the assumption that mass transfer on the metal side is the rate-determining mechanism has been experimentally supported in a number of studies [81, 80].

In a practical sense, desulfurization process is much more complicated than what has been summarized here. For more information regarding the desulfurization of steel, please refer to [69, 47].

Appendix D

A Derivation of the Conversion Ratio in a Continuous Reactor

Assuming an ideal plug flow reactor having a mass transfer at one of its boundaries as shown in Figure D-1. Fluid is flowing from left to right with a uniform velocity of U, while the third dimension is not shown in the figure.

The rate of mass transfer at the top boundary is $kacdx$, where a is the surface area per unit volume (A/V) and k is the mass transfer coefficient at the top boundary. The equilibrium concentration outside of the reactor is assumed to be zero.

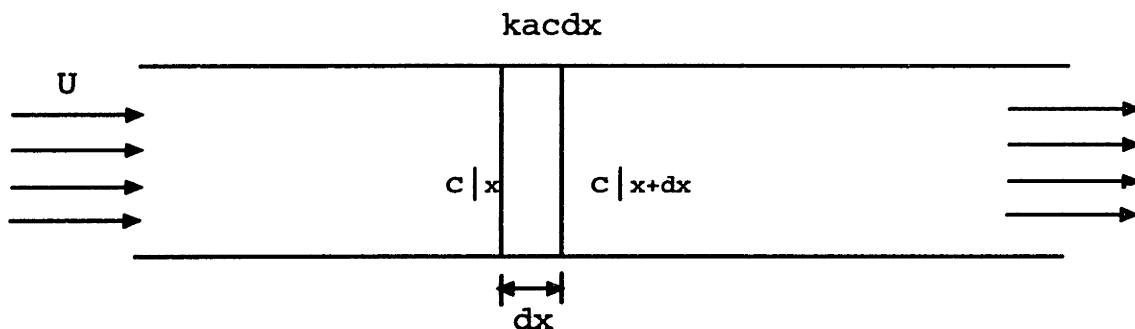Let's examine a sectional volume element of thickness dx, and perform a mass balance for concentration c:

Figure D-1: A schematic of an ideal plug flow reactor (The third dimension is not shown here).

$$Uc|_x - Uc|_{x+dx} = kacdx \tag{D.1}$$

divided by dx:

$$U\frac{dc}{dx} = -kac \tag{D.2}$$

since dx=Üdt, the equation above can be rewritten as:

$$\frac{dc}{dt} = -kac \tag{D.3}$$

integrate above equation:

$$\int_{c_i}^{c_o} \frac{dc}{c} = \int_0^{t_R} -kadt \tag{D.4}$$

we get:

$$\ln c_o - \ln c_i = -kat_R \tag{D.5}$$

where c_i and c_o are the concentrations at the inlet and outlet of the reactor, respectively; t_R is the characteristic residence time of the reactor.

rewrite above equation:

$$\frac{c_o}{c_i} = e^{-kat_R} \tag{D.6}$$

then the conversion ratio of the reactor can be obtained from:

$$1 - \frac{c_o}{c_i} = 1 - e^{-kat_R} \tag{D.7}$$